Unitized Stiffened Composite Textile Panels: Manufacturing, Characterization, Experiments, and Analysis

by

Cyrus Joseph Robert Kosztowny

A dissertation submitted in partial fulfillment
of the requirements for the degree of
Doctor of Philosophy
(Aerospace Engineering)
In The University of Michigan
2017

Doctoral Committee:

Professor Anthony M. Waas, Co-Chair, University of Washington
Associate Professor Veera Sundararaghavan, Co-Chair
Assistant Professor Sean Ahlquist
Professor Joaquim R. R. A. Martins
Dr. Marc R. Schultz, NASA Langley Research Center

Cyrus Joseph Robert Kosztowny
ckosztow@umich.edu
ORCID iD: 0000-0003-4603-6861

To my family

ACKNOWLEDGMENTS

I thank everyone who supported me throughout my graduate career. I am grateful I had the opportunity to meet, work, laugh, and learn with all of you. This work would not have been possible without your camaraderie.

I would like to first thank my advisor, Professor Anthony Waas, for his motivation, guidance, and mentorship during my years at the University of Michigan. He never fails to inspire me when I need it. His knowledge and passion for learning have influenced me a great deal over the years and have instilled a lifelong goal to never cease learning. I would also like to thank Dr. Marc Schultz for his collaboration through the NASA Space Technology Fellowship program. Much of the imperfection data and experimental results would not have been possible without his assistance. I would also like to thank NASA and the NSTRF program for their support, both financially and professionally, over the course of my graduate career.

I thank my committee members Professor Veera Sundararaghavan, Professor Martins, and Professor Ahlquist for the opportunities they have given me as a student and researcher. A special thanks to Professor Sundararaghavan for becoming my University of Michigan Co-Chair after Professor Waas moved to the University of Washington.

Too many others to mention have been so helpful throughout this journey. Thank you to the technicians and staff at the University of Michigan, the University of Washington, and at NASA Langley Research Center. A special thank you to Terry Larrow and Tom Griffin at UM for teaching me that life goes on and that today's problems will seem small in comparison to tomorrow's successes. Thanks to my fellow WaasGroup colleagues and to all students I learned from: Evan Pineda, Mark Pankow, Wooseok Ji, Amit Salvi, Pavana Prabhakar, Paul Davidson, Zachary Kier, Marianna Maiaru, Dianyun Zhang, Royan D'Mello, Brian Justusson, Christian Heinrich, Jiawen

Xie, Solver Thorsson, Armanj Hasanyan, Ashith Joseph, Deepak Patel, Jaspar Marek, Nhung Nguyen, David Singer, and everyone else too numerous to list.

None of this would have been possible without the tremendous love from my family. They have supported me through both good and bad times, and they never doubted I would one day attain this achievement. Mom, Dad, Zac, and Heather, I love you all, and thank you for everything.

TABLE OF CONTENTS

LIST OF TABLES

LIST OF FIGURES

ABSTRACT

Use of carbon fiber textiles in complex manufacturing methods creates new implementations of structural components by increasing performance, lowering manufacturing costs, and making composites overall more attractive across industry. Advantages of textile composites include high area output, ease of handling during the manufacturing process, lower production costs per material used resulting from automation, and provide post-manufacturing assembly mainstreaming because significantly more complex geometries such as stiffened shell structures can be manufactured with fewer pieces. One significant challenge with using stiffened composite structures is stiffener separation under compression. Axial compression loading conditions have frequently observed catastrophic structural failure due to stiffeners separating from the shell skin. Characterizing stiffener separation behavior is often costly computationally and experimentally.

The objectives of this research are to demonstrate unitized stiffened textile composite panels can be manufactured to produce quality test specimens, that existing characterization techniques applied to state-of-the-art high-performance composites provide valuable information in modeling such structures, that the unitized structure concept successfully removes stiffener separation as a primary structural failure mode, and that modeling textile material failure modes are sufficient to accurately capture postbuckling and final failure responses of the stiffened structures. The stiffened panels in this study have taken the integrally stiffened concept to an extent such that the stiffeners and skin are manufactured at the same time, as one single piece, and from the same composite textile layers. Stiffener separation is shown to be removed as a primary structural failure mode for unitized stiffened composite textile panels loaded under axial compression well into the postbuckling regime. Instead of stiffener separation, a material

damaging and failure model effectively captures local post-peak material response via incorporating a mesoscale model using a multiscaling framework with a smeared crack element-based failure model in the macroscale stiffened panel. Material damage behavior is characterized by simple experimental tests and incorporated into the post-peak stiffness degradation law in the smeared crack implementation. Computational modeling results are in overall excellent agreement compared to the experimental responses.

CHAPTER 1

Introduction

1.1 Motivation

Use of carbon fiber textiles in complex manufacturing methods creates new implementations of structural components by increasing performance, lowering manufacturing costs, and making composites overall more attractive across industry. Straight, or unidirectional, carbon fiber material is not the only industry standard option despite pervasive use in structural applications across air- and space-based components. Similar to how common fibers such as cotton or silk are spun into yarns before being used to generate textiles, many individual carbon fibers are agglomerated to form carbon fiber yarns or fiber tows. These tows can then be used to form carbon fiber textiles, and it is these textiles that form the base material for textile composite structures. While carbon fiber textiles have been used in certain applications for almost as long as carbon fiber has been used in structural applications, many advantages of carbon fiber textiles over other forms have not been taken advantage of for various reasons. Some of the disadvantages with textile composites are typically reduced stiffness in the principal material direction. As there are fibers woven or braided along multiple directions, the stiffness per amount of fiber is not as high as plain unidirectional material. Post-peak material behavior, both damage initiation and progression, are also active areas of research as the understanding of textile damage mechanics is not as developed as that for unidirectional or random-

oriented composites. A few advantages of textile composite materials include high area output of material, ease of handling during the manufacturing process, and lower production costs per material used due to automated manufacturing processes. How effectively the textile can drape over complex geometries also lends to increased manufacturing capabilities that would be difficult with unidirectional materials. Since textiles maintain their integrity while bending around high curvature molds and can even fold around corners, significantly more complex geometries such as stiffened shell structures can be manufactured with fewer pieces and require less post-manufacturing assembly. Reduced manufacturing waste is a benefit of most composite materials resulting from the "build up" process in a structure, and textile composites observe similar benefits compared to metallic structures.

One significant challenge with using stiffened composite structures is stiffener separation under compression. Axial compression and similar (post-) buckled loading conditions have frequently observed catastrophic structural failure due to the reinforcing stiffeners separating from the shell structure. Once a stiffener separates, the underlying structure cannot support the previously sustained loads and often fails suddenly. Modeling and validating stiffener separation behavior is often costly both computationally and experimentally. New manufacturing concepts that remove the stiffener separation failure mode can prove effective in reducing modeling complexity by removing the need to include separation behavior. The strength and ultimate postbuckling behavior of the structural panel can then be captured using material failure methods only rather than structural level stiffener separation methods.

1.2 2D Triaxially Braided Composite Textile

Many types of composite textiles are manufactured, and the benefits of one textile over another vary depending on the intended service, performance requirements, cost, and production quantity among other considerations. The material used for this research is a 2D triaxially braided carbon (TBC) fiber textile. The braiding process is similar to weaving. In woven textiles, the angle between tows is usually 90° with a vertical fiber tow and perpendicular horizontal tow. In braided textiles, the tows are typically biased at an angle from the vertical direction and are symmetric. This biaxial braid is often

described as having a ±θ° bias about the braiding direction. For triaxially braided textiles, axial fiber tows are incorporated into the braid and the bias tows are braided around the axial tows. The braid is planar, or 2D, because the textile does not incorporate any out-of-plane fiber orientations beyond minimal tow undulations as tows cross above and below each other. The maypole in certain European summer festivals can be considered a type of triaxially braided structure because the bias strands are braided around strands that remain still. Figure 1.1 provides a diagram of a generic 2D triaxially braided textile. Orange tows are biased at an angle ±θ° about the axial tow reference direction highlighted by the blue tows. The principle direction is taken to be in the axial tow direction for such 2D triaxially braided textiles.

Figure 1.1: Diagram of 2D triaxially braided textile

2D triaxially braided textiles were chosen in this study for the ease of handling in the manufacturing process, excellent conformity to folded geometries, good material property variation depending on the bias angle, and material availability. Two braiding bias angle materials were used in this study, where θ = 30° and θ = 60°, and the braiding angle was held constant for each type of material, respectively. The 30° textile (TBC 30) is orthotropic when cured with a polymer matrix while the 60° textile (TBC 60) is almost quasi-isotropic when cured. Figure 1.2 shows images of cured TBC 30 and TBC 60 material and highlights the bias tow angle differences between both materials. Figure 1.3 shows what dry textile prior to manufacturing with a polymer resin looks like and is an example of a 45° TBC textile material.

Figure 1.2: Cured TBC 30 material (left) and TBC 60 material (right)

Figure 1.3: Dry TBC 45 material

1.3 Unitized Structure Concept

Reducing part counts and post-manufacturing assembly steps have been shown to reduce overall time and cost to create a structural component. There has consequently been increased interest in the use of "integral" structures where there are minimal sub-components to a much larger structure, and the manufacturing and design processes are used to specifically decrease part counts and structural assembly time while satisfying performance and weight requirements. Current large-scale stiffened shell structures used as part of rocket fuselages are often integrally stiffened where the stiffeners and skin are machined from a much thicker single piece of metallic material. The process machines away the majority of the original material volume generating waste and is time and energy intense. Composites, with their typical "build-up" manufacturing process instead of the "machine-down" metallic processes, can be better suited to taking advantage of the benefits of creating large, complex structures. The stiffened panels in this study have taken the integrally stiffened concept to an extent such that the stiffeners and skin are manufactured at the same time, as one single piece, and from the same composite textile

layers. Such one-piece structures are herein called unitized stiffened panels because there is only one piece of the final structure, and the unitized panel cannot be broken down into any components because there are none. Bonded stiffeners, commonly used in current composite structures, typically have an adhesive layer that may cause a gradient to develop in the stress field while under load. Whether the adhesive layer or a layer in the composite near the adhesive fails, the unitized stiffened panel herein is designed not to fail as a result of the effects of stress gradients in the presence of bonded features. Composite textiles offer certain advantages over other forms of composite materials such as unidirectional pre-impregnated fiber because the dry textile can withstand being manipulated to create complex geometries like stiffened shell structures prior to the curing process without loss of integrity. As there are fibers running in directions other than axially, textiles typically exhibit lower stiffness in the principal material direction than pure unidirectional material. The textile manufacturing process also introduces fiber waviness from the undulation over and under other bundles of fibers. The bundles of fibers, or fiber tows, also may create local resin rich regions during manufacturing if the tows do not nest adequately. Nesting in this work refers to the ability of fiber tows to conform to neighboring tows within the textile and across textile layers.

As the textiles used to create the unitized stiffened panels are 2D, multiple layers may be used with standard lamination techniques. The unitized panel concept, however, could be used with just a single layer of composite textile material. In this work, certain layers in the unitized stiffened panel form just the flat skin section, while others are wrapped and folded over themselves to create a J-shaped stiffener geometry. Other stiffener geometries are possible and are limited only on the ability of the textile to fold or drape around surfaces. J-shaped stiffener geometry was chosen for this work to demonstrate that geometries more complex than standard blade stiffened structures could be manufactured while not significantly increasing the mold complexity. The layers that are folded over to create the stiffener geometry also contribute to the skin thickness as well, so the same layer of material is part of the stiffener and part of the skin without a physical break in material. This would not be achievable without using textiles as the fundamental material component. With this stiffener design, two layers of TBC material were used for the skin-only, and two layers were used to create the stiffener geometry for

a combined total of four textile layers. Figure 1.4 demonstrates the differences between commonly adhered stiffeners and the unitized textile stiffener concept.

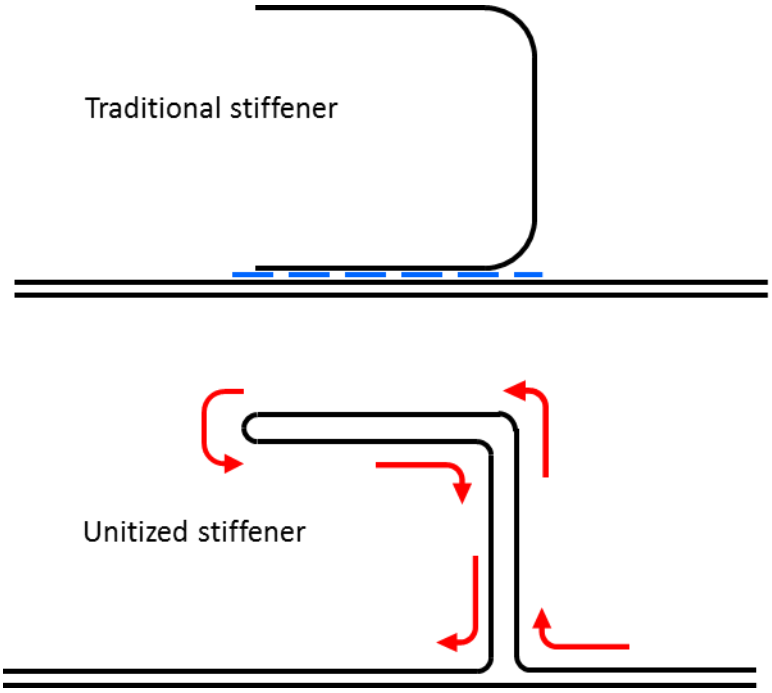

Figure 1.4: Diagram contrasting an adhesively bonded stiffener (top) and a unitized textile stiffener (bottom)

It should be noted that each section of the panel has four layers of TBC material regardless of whether it is a skin or stiffener section. The stiffener sections have four total layers because two of the textile layers were folded over, effectively doubling the thickness and number of material layers. The skin sections are where there are four separate textile layers as the skin sections are not generated by this folding process.

No post-manufacturing methods are used on the unitized stiffened panels other than trimming the panel edges. The resulting panel is a single-piece stiffened structure where the stiffeners essentially cannot be separated from the skin sections post-cure because they are made from the same textile layers. While it theoretically is possible to separate each layer from the next, such significant delamination between the layers is an energetically unfavorable failure mode and therefore stiffener separation is effectively removed as a primary failure mode.

1.4 Research Objectives

The objectives of this research effort are to demonstrate that unitized stiffened textile composite panels can be manufactured in such a way so as to produce quality test specimens, that existing characterization techniques commonly applied to many types of composites provide valuable information to model such structures, that the unitized structure concept as previously discussed successfully removes stiffener separation as a primary structural failure mode, and that modeling TBC material failure modes are sufficient to accurately capture the postbuckling response and failure of the stiffened structures. A vacuum-assisted resin transfer molding (VARTM) manufacturing method is used because it produces consistent, high quality test specimens with little special equipment and is an out-of-autoclave (OOA) process easily adaptable to making unitized stiffened composite textile panels. Various characterization techniques such as acid digestion and optical inspection for fiber volume fraction determination, an in-plane shear modulus test independent of material principal directions, and as-manufactured geometric imperfections using a coordinate measurement laser scanning machine are used to demonstrate the effectiveness of the VARTM method. A computational multiscaling approach is implemented to accurately model TBC material failure using a nonlinear in-situ matrix characterization technique to capture local tow buckling coupled with crack-band material degradation method on the macro scale model. Comiez demonstrated that structures loaded in compression can experience significant loss in load carrying capability when delaminations are present and allowed to propagate [1]. The aim of this research is to provide conclusive evidence that unitized stiffened composite textile panels are effective at removing stiffener separation under axial compressive loads and can be accurately predicted without using structural failure mechanisms.

1.5 Dissertation Organization

The research to meet the objectives is discussed in the following five chapters. Chapter 2 details the VARTM composite manufacturing process used to obtain the test specimens that provided experimental results to achieve the research objectives. An overview of typical composite manufacturing methods is given, and the VARTM method

that was chosen is explained in further detail. The VARTM method was chosen over other methods due to the low initial equipment requirement to manufacture composite specimens, high-quality aerospace-grade specimens were consistently produced, and that VARTM as implemented in this work is an out-of-autoclave process with an exothermic polymer resin matrix. In Chapter 3, various techniques that were used throughout this work to characterize the TBC material having been manufactured with the VARTM process are discussed. Other work was previously performed [2] on TBC material that was manufactured using a high pressure resin transfer technique instead of VARTM. The high pressure resin infusion resulted in thickness-controlled panels, but there were some quality issues commonly observed with that technique. Voids and lack of fiber wetting, or the lack of complete resin infusion, throughout the preform, were clearly visible. Using a thickness-controlled infusion method also reduced the potential for the fiber tows to nest. The characterization techniques used herein include fiber volume fraction determination, basic material property verification, and as-manufactured geometric imperfection characterization for each of the experimentally tested unitized stiffened composite textile panels.

Chapter 4 provides the experimental tests used to assist in the characterization of the TBC material and the setup used in the primary axial compression tests to load the unitized stiffened panels well into the postbuckling regime. Experimental results are provided for each manufactured and tested unitized stiffened panel. Chapter 5 expands the work discussed in Chapter 4 by providing the analysis and modeling contribution to the research objectives. A macroscale stiffened panel model is introduced, as well as a multiscale computational framework used in the complete nonlinear analysis for modeling each individual stiffened panel. In conjunction with the macroscale stiffened panel model, the multiscale framework uses a mesoscale triaxially braided composite representative volume element (RVE) model at a localized level to capture braid angle specific damage behavior observed in the stiffened panel experiments. Work by Heinrich [3], for example, demonstrates that textiles may be strongly influenced by the underlying architecture at a local level, but the global response of a structure can be homogenized effectively at larger length scales. The smeared crack material damaging constitutive model by Bazant [4] called crack band is used at the macroscale model to implement

material damage and stiffness reduction following post-peak behavior. A comparison of the computational analysis results to the experimental results is given. Chapter 6 concludes with a summary of the results obtained by this research and provides suggestions for future areas of investigation into utilizing the advantages of textile composites in unitized stiffened structures.

CHAPTER 2

Triaxially Braided Composite Manufacturing

2.1 Overview of Composite Manufacturing Methods

As composite materials increase in complexity and specialization, composite manufacturing methods also must be capable of meeting the requirements and capabilities of high-performance materials and structures. Just as analysis methods for metallic or ceramic materials are not necessarily applicable to analyzing fiber-reinforced materials, the manufacturing methods used for metallic structures are typically not applicable to composites. Fiber-reinforced composites are broadly classified as having a build-up manufacturing process [5] where individual segments of material, either dry fibers or fibers and resin mixed together, are added to each other to create the desired structure. Conversely, metallic structures are often built in a machine-down process where unwanted material is machined away until the desired structure is left. The build-up method of composites has clear advantages in that minimal waste is possible for a given structure geometry, and that controlling the placement of material can be developed at a high level resulting in weight savings. Other significant advantages of build-up techniques are less capital requirements in post-manufacturing machining as the structure is near net shape from the manufacturer. The composite structure can be designed and manufactured in such a way so as to reduce the number of post-manufacturing modifications prior to being implemented in the larger structural system. The ability of

composites to be built up from the design phase achieves performance increases in material sizing requirements, reduced material waste, reduced capital requirements for post-manufacturing processing, and similar areas of structural processing beyond the in-service use.

There are many composite manufacturing technologies available today. Two broad manufacturing categories depend on whether the constituent materials are pre-mixed or if the resin is to be added to the dry fibers in a second manufacturing process. Preimpregnated fiber composites have fiber reinforcement embedded in a partially cured resin material. These materials are often thermally activated to begin the curing process. Resin transfer molding, or RTM, is in the other category where dry fibers are formed into the desired structure shape and resin is then infused and cured. Both broad categories have their advantages and disadvantages, and each should be evaluated for the desired traits and feasibility for the composite structure. An RTM technique was chosen for manufacturing the unitized stiffened composite textile panels because of the ability to scale the technique down to research lab sized capability as well as some RTM methods do not require an autoclave to fully cure the composite. The resin transfer is assisted by a vacuum pressure differential across the mold of the stiffened panel preform. The vacuum pressure effectively draws the bulk uncured liquid resin into the mold. It also assists in distributing the resin throughout the entire mold as the liquid attempts to fill the void created by the vacuum. This method is called vacuum-assisted resin transfer molding and has many advantages over other types of manufacturing techniques for the research in this study.

VARTM methods typically require minimal equipment in order to be able to successfully manufacture structures. The ability to customize the dry fiber preforms into non-standard shapes to handle the unitized stiffened panel concept was vital for this work. VARTM is typically used in an out-of-autoclave process where applied external pressure and temperature are not required to manufacture aerospace quality components. An exothermic, thermoset resin system of Epon 862 with EpiKure 9553 hardener is used as the matrix material in this study. This resin system is chosen for low viscosity in the infusion process, good chemical and physical resistances after curing, good physical perofrmance, and availability. The resin system is considered to be an aerospace grade

resin. The VARTM process also returns high-quality and consistent composite specimens. With the relative simplicity of the setup, ease of handling, and high quality results, the VARTM method is chosen as the best manufacturing path for the present work.

2.2 Vacuum-Assisted Resin Transfer Molding Setup

Equipment required for a VARTM setup consists of assorted hand tools, consumable roll material like vacuum bags, tapes, infusion assistance media, etc., a composite mold, and a vacuum pump. Over the course of this study, multiple types of composite panels were studied to determine the range for which VARTM methods could be used. The overall VARTM process remains similar across all types of panels, but the mold specific geometry and infusion media differ depending on the application. The next section overviews and discusses the main types of panels that were made in the VARTM study.

The VARTM process with the TBC textiles begins with the creation of the dry textile preform. This preform consists of the TBC textile layers used to create the type of desired panel and various resin infusion assistance media. A peel-ply material is used for easing the de-molding process, a polyester batting material is used as a breather to soak up excess resin, and a resin flow media increases the resin infusion speed by creating tiny channels for the resin to flow. Figure 2.1 shows an example of a flat plate of TBC material dry preform. The outer layer is the resin flow media and resembles a chain link fence in texture.

Aluminum 0.25-inch plates are used to create the supporting mold geometry with the dry preform sandwiched in between them. Polyvinyl alcohol Partall #10 mold realease is applied to the aluminum surfaces to assist in the de-molding process. For the stiffened panel geometry mold, aluminum block inserts are also used and form the desired J-shaped stiffener geometry. Other consumable materials used for the manufacturing process include various tubing and T-connectors to direct the flow of resin under vacuum pressure.

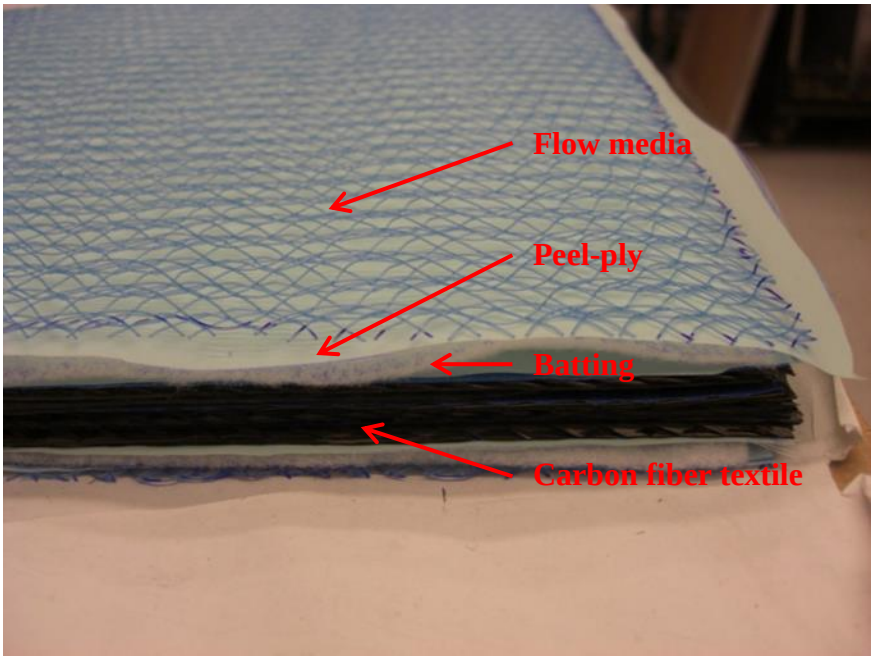

Figure 2.1: TBC material dry textile preform with resin infusion assistance media

Figure 2.2 shows the assembled dry preform sandwiched between aluminum plates and with all infusion materials attached. This is the step immediately prior to sealing in

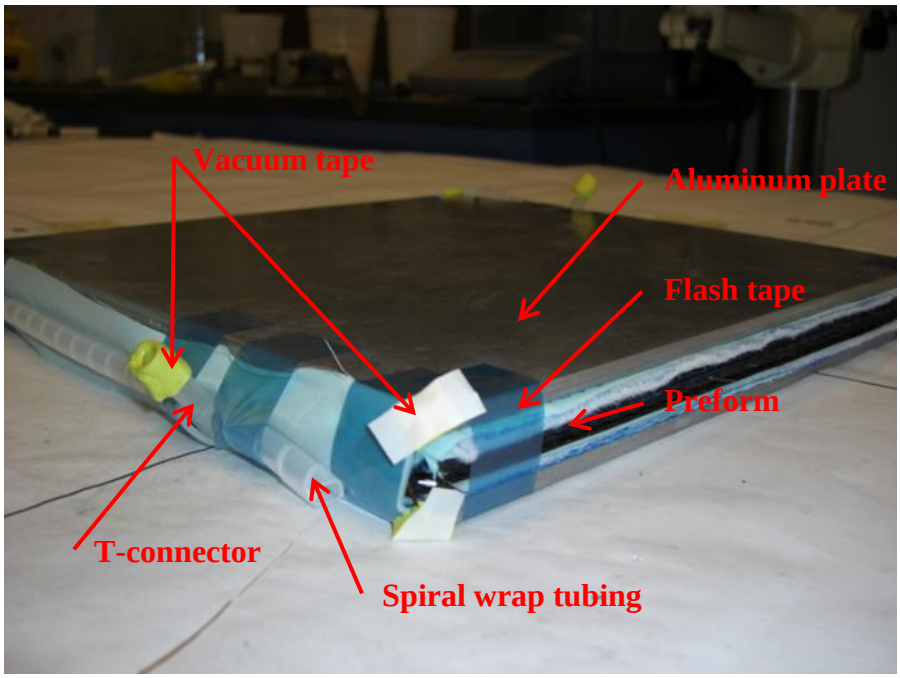

Figure 2.2: Completed 8-ply VARTM panel mold

the vacuum bag and attaching the resin inlet and outlet ports. Vacuum bag material is wrapped over the completed mold and sealed with vacuum tape. Resin inlet and outlet tubes are attached to the ports and the setup is tested for vacuum pressure integrity. A vacuum pump pulls vacuum, and the inlet/outlet tubes are clamped for 30 minutes to check if the vacuum integrity changes. If even a very tiny hole is present, the vacuum bag will lose integrity and the infusion process will not be successful. Figure 2.3 shows the sealed vacuum bag and mold prior to testing vacuum integrity.

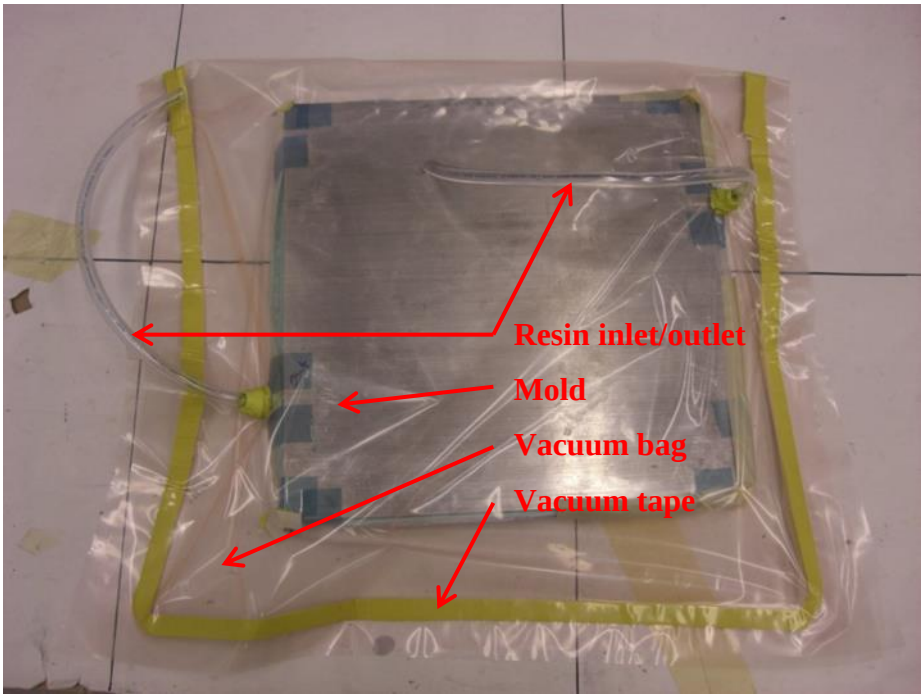

Figure 2.3: VARTM bagged and sealed infusion mold

Figure 2.4 demonstrates the intended flow paths of resin in a flat plate specimen. Actual resin flow will vary slightly based on a number of factors. Excessive compression of the dry preform effectively prevents resin flow across the length of the panel. When this occurs, the edges of the panels usually become infused with resin but areas in the center may suffer from poor infusion quality. It has been observed that sufficient but not excessive compression aids the resin flow because there is less volume for the resin to fill at a given location. The use of resin flow media helps prevent excessive fiber compression by acting as a buffer between the preform and the aluminum plates.

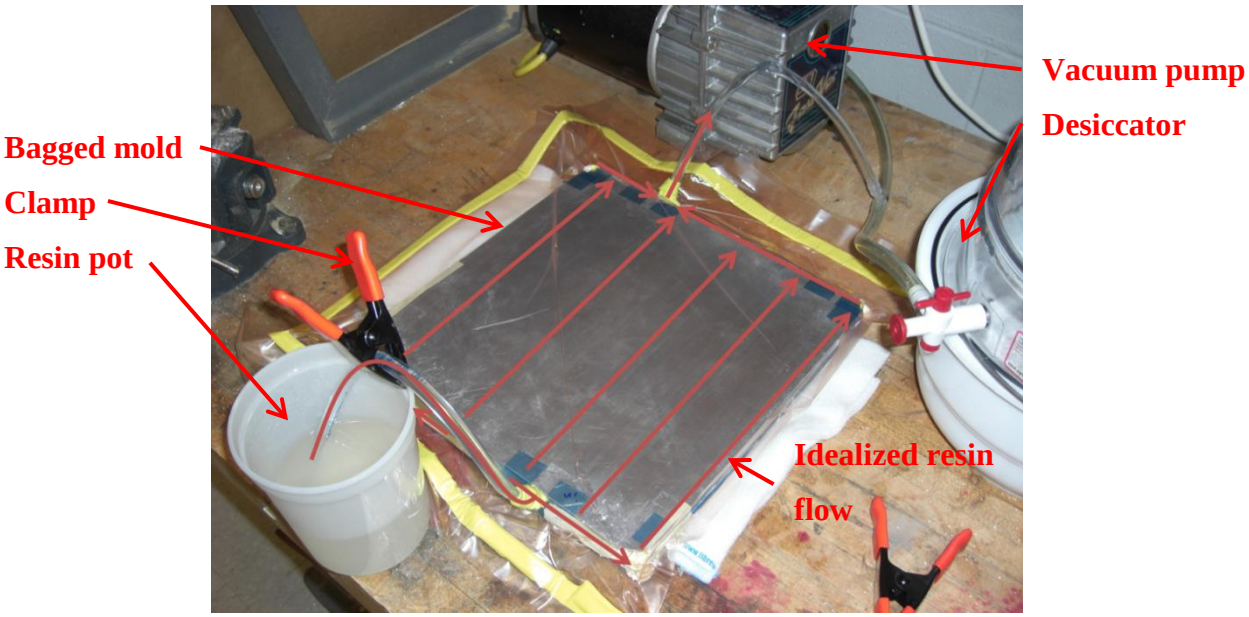

Figure 2.4: Idealized resin flow during infusion across a flat plate TBC specimen

Figure 2.5 shows a cross sectional view of the vacuum bag and dry preform concept. Note the specific layers of textile, infusion assistance media, and aluminum plates. Extra material is also used for the infusion process such as spiral wrap tubing to distribute resin equally along the width of the specimen from the inlet port.

If specimens different than flat plates are needed, the infusion process changes little. The significant changes occur in the mold shape itself as well as the infusion media. The infusion media is not required for the VARTM process, however, it does provide better consistency and higher-quality specimens. One disadvantage of using the infusion media is the surface texture of the specimens is difficult to control. The nylon peel-ply release media imparts a coarse texture to the surface of the specimens. If no infusion assistance media were to be used, the surface finish would be that of the mold. Infusing a specimen without using infusion media is possible and achieves a very smooth and high quality surface, but demolding becomes significantly more difficult and the resin flow is more difficult to control consistently. Various prototype specimens were investigated and are discussed in the next section.

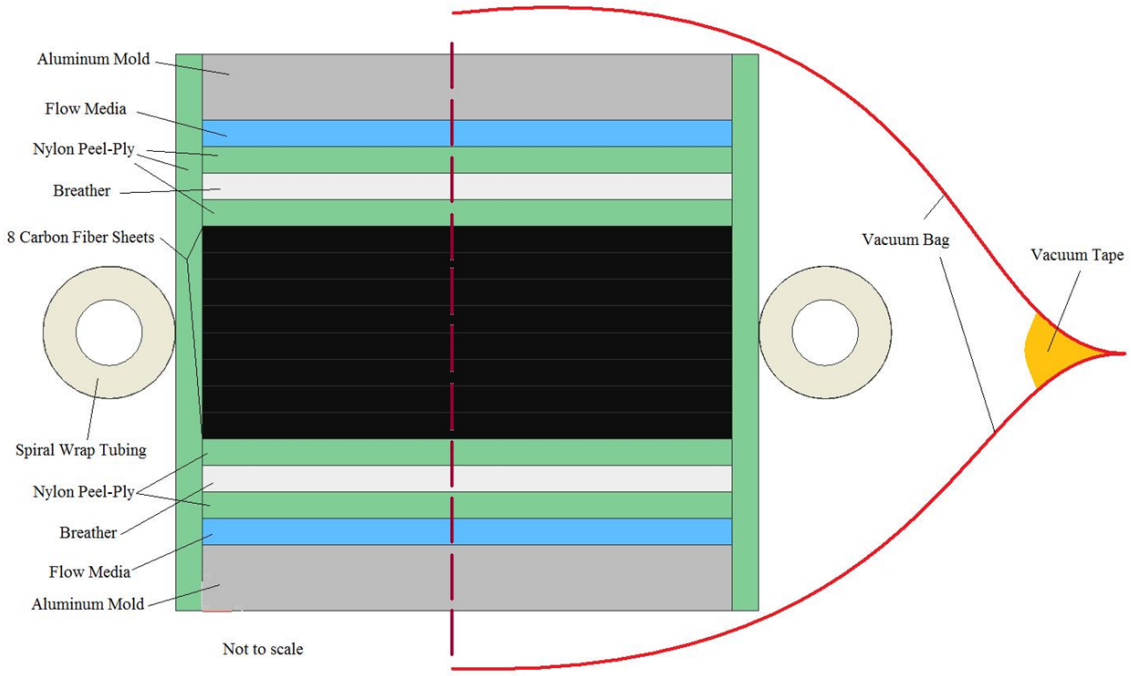

Figure 2.5: 8-ply cross sectional view highlighting vacuum bag concept

2.3 VARTM Panel Prototypes

In using the VARTM manufacturing method, a study was done to see what types of specimens could be produced and what quality could be obtained. A simple flat plate is first discussed with the previously detailed dry preform in Figure 2.5. A pure resin plate is then overviewed and demonstrates that the VARTM process can be used to achieve thickness-controlled specimens despite that not usually being of greatest importance. The concept of a mid-ply plate and the two steps taken to manufacture it is mentioned. Lastly, the unitized stiffened panel mold and preform used in this work is overviewed. This is the setup used to create the stiffened panels characterized, tested, and modeled for the remaining body of work.

2.3.1 8-Ply Flat Plate

To demonstrate the initial effectiveness of the VARTM process, simple geometries were used. Flat, one-square-foot panels were manufactured. The cross-sectional view of the mold, preform, and vacuum bag were previously shown in Figure 2.5. Eight layers of TBC textile material were used in the manufacturing of these

specimens, and some of these samples were used in the characterization methods detailed in 3.2. It should be noted that the method used for the 8-ply plates was not thickness controlled, but consistent resin infusion volume control effectively resulted in consistent thicknesses across all manufactured specimens.

2.3.2 Pure Resin Plate

As the VARTM method previously outlined is not a thickness controlled manufacturing method, a technique was developed to create specimens that are thickness controlled. The primary way this was achieved was to use a spacer inserted around the perimeter of the aluminum flat plates. No infusion media was used in the thickness controlled specimens because the media could not be controlled in any way in the interior of the mold. Also desired was the ability to manufacture pure resin material without reinforcing fibers. It is sometimes difficult to obtain pure resin material that cures under similar conditions as those used in the manufacturing of fiber reinforced composites. The pure resin plate allows the VARTM process to be tested in thickness control as well as demonstrate that matrix material is cured under similar manufacturing conditions for possible testing purposes. Figure 2.6 provides a diagram of the spacer system used in manufacturing thickness controlled pure resin plate specimens.

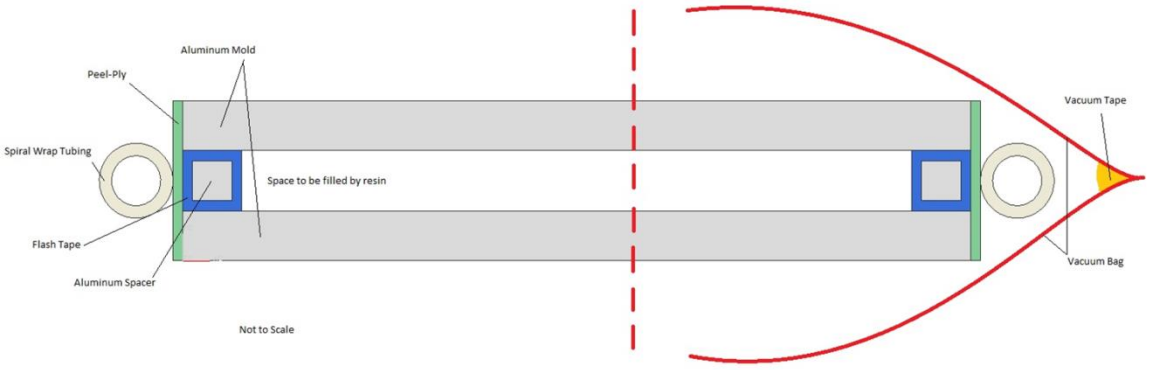

Figure 2.6: Pure resin mold cross sectional view highlighting use of spacers

2.3.3 Mid-Ply Plate

The mid-ply plate concept derives from the need to determine if a composite layer embedded in other material behaves differently than if the layer were on the outer surface. It has been well documented that edge and surface effects can play a significant

role in how material behaves [6]. The mid-ply plate concept is to manufacture a single textile layer plate using the method outlined in the 8-ply section. After the single ply had cured, it would be placed in a setup similar to the pure resin plate previously described and infused a second time under thickness control. This effectively created a single layer textile composite that is embedded in the center of pure matrix material. Spacers were used to keep the single ply centered between the aluminum molds during the infusion process as well as to control the overall desired thickness of the final plate. Figure 2.7 shows a diagram of the single textile layer spaced between the aluminum plates to allow pure resin material to flow on either side and be embedded in the center of the final specimen.

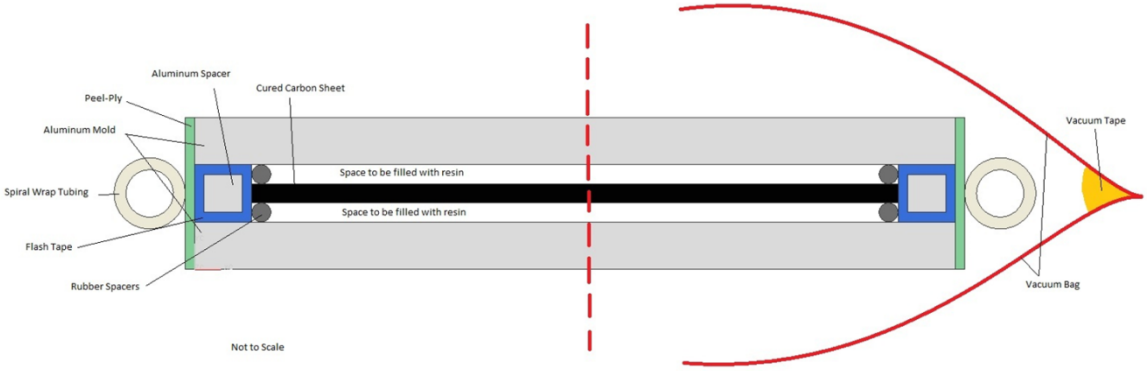

Figure 2.7: Mid-ply layup cross sectional view showing the spacers for both the pure resin areas and the secondary spacers for the pre-cured laminate

2.3.4 Unitized Stiffened Panel

The unitized stiffened panel concept takes ideas from all three previously described VARTM mold setups as the geometry is significantly more complicated with the inclusion of J-shaped stiffeners. The 8-ply plate forms the basis of the mold concept because all sections of the textile plate are surrounded by infusion assistance media. Using infusion assistance media significantly increased the quality and repeatability of manufacturing the stiffened panels as the vacuum pressure was sufficient to compress the textile layers enough to prevent thorough fiber wetting in all sections of the panel if the media was not used. Aluminum blocks were inserted between the aluminum plates so that the textile TBC material could be folded over itself to form the unitized structure while

maintaining the stiffener geometry. Figure 2.8 shows a cross sectional view of the J-shaped stiffener section of the idealized mold used to manufacture the unitized stiffened textile composite panels and is not to scale. Note that the aluminum insert used between each stiffener was composed of two separate blocks. The justification for this was purely based on manufacturability during the demolding procedure. The block cured under the flange was removed only after the first block was taken out to minimize stiffener twisting.

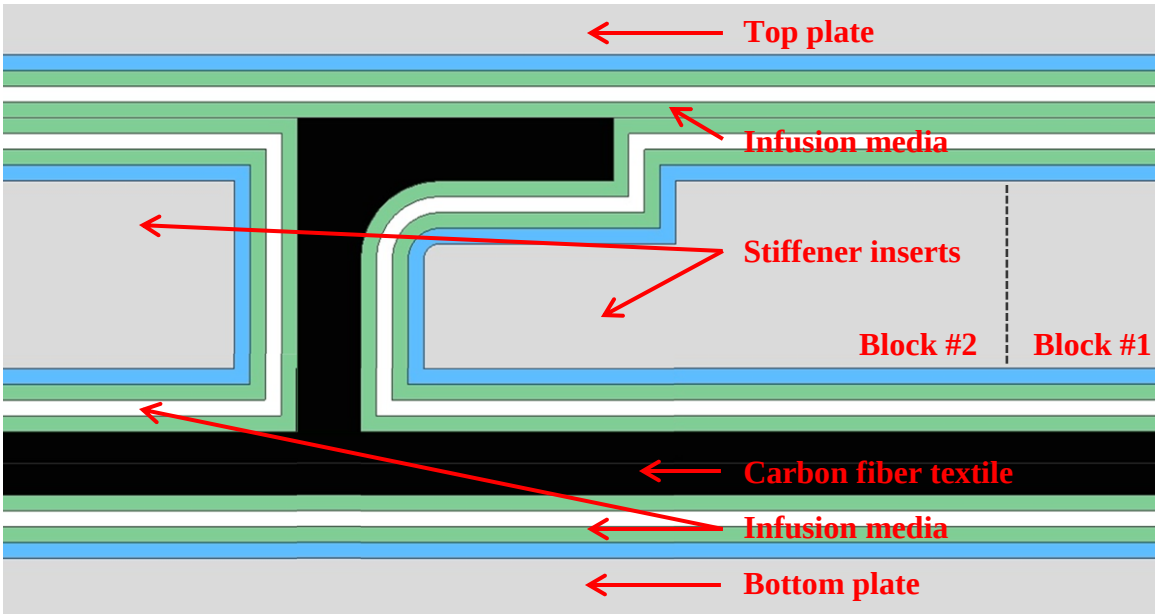

Figure 2.8: Sectional view of stiffened panel mold for J-shaped stiffeners

The nominal dimensions of the unitized stiffened panels are provided in Figure 2.9. As the aluminum blocks used to define the stiffener geometry were not actual spacers as implemented in the pure resin and mid-ply plates, the resulting stiffened panels are not manufactured under thickness controlled infusion conditions. Consistent resin volume control is used in a similar manner as the 8-ply plates to achieve repeatable results. The lack of thickness control, however, does result in meaningful deviations from the nominal geometry shown in Figure 2.9. These deviations are further discussed in the next chapter.

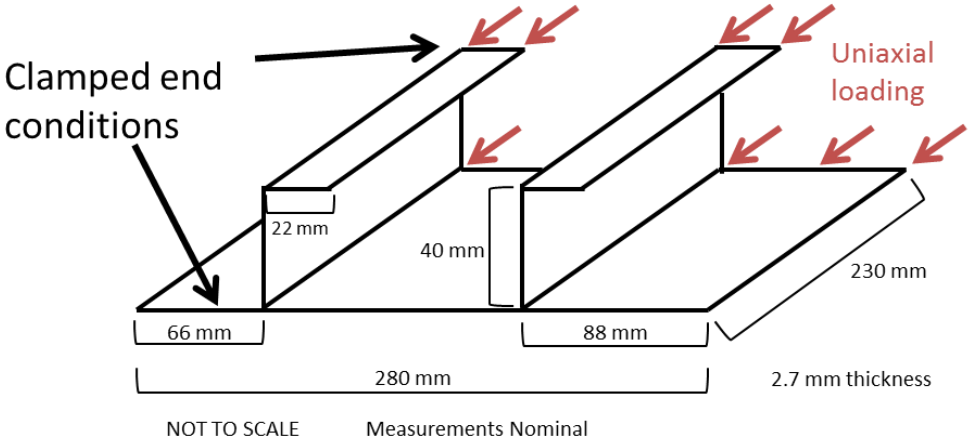

Figure 2.9: Nominal panel dimensions for unitized concept

Figure 2.10 provides the oven curing cycle used while manufacturing all VARTM TBC textile specimens. An initial ramp to 130°F over 15 minutes brings the vacuum bagged mold to a temperature that accelerates the exothermic reaction to begin curing. This temperature is held for 1 hour to allow enough time for the resin to begin the gelation process and start to solidify. A second ramp over 15 minutes to 200°F is then applied. This elevated temperature occurs at a time in the cure cycle to encourage significant cross-link development between molecules of the polymer resin. Cross-linked

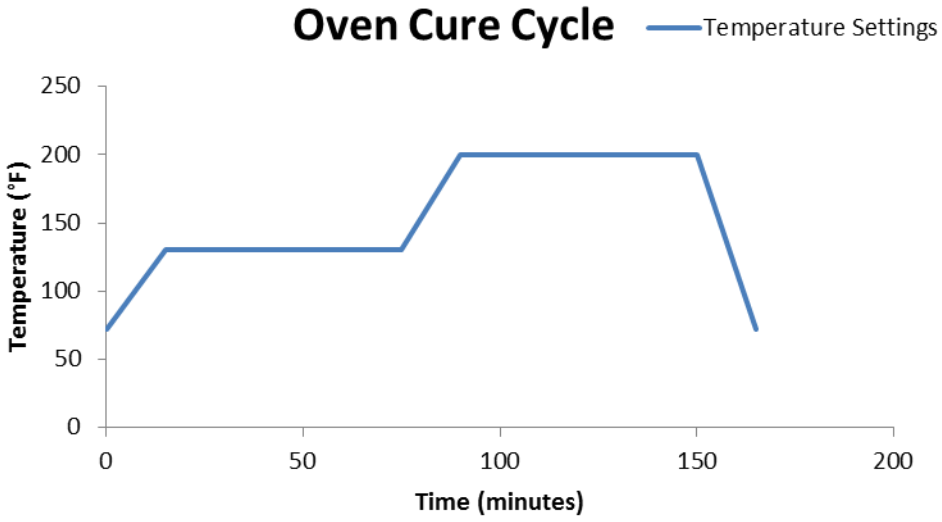

Figure 2.10: Oven cure cycle used for all TBC textile VARTM manufactured specimens

polymers are advantageous over some other types of cured polymers because of demonstrated increased stiffness, strength, and even fracture properties [7]. By making the matrix less susceptible to micro cracking and damage accumulation as a result of the enhanced cross-linking, the post peak performance of the material is enhanced [8], [9]. Song in [8] showed that the effects of matrix micro cracking has a strong effect on the post-peak response in TBC material. Rask in [9] found that matrix rich regions between fiber tows are susceptible to matrix shear damage. This leads to the conclusion that matrix material toughening may lead to less damage accumulation prior to other modes of failure, or at least delay damage initiation or progression.

The 8-ply flat plates used in the characterization studies and the anticlastic bending specimens in Chapter 3, the TBC 45 axial tension test coupons in Chapter 4, and the unitized stiffened composite textile panels in Chapters 4 and 5 were all manufactured with an oven cure cycle. While the exothermic Epon 862 resin system does not require an oven cure cycle, it provides the specimens with increased properties as previously mentioned via enhanced cross-linked polymers. The added equipment item does not detract in a meaningful way to the otherwise minimal required equipment VARTM process.

2.4 Summary

Vacuum-assisted resin transfer molding methods are developed in this work to manufacture unitized stiffened composite textile panels. Using inserts to define the stiffened panel geometry and stiffener shape, coupled with the addition of a top aluminum mold plate create a mold setup not previously observed in VARTM use. VARTM proved to be an excellent manufacturing technique to demonstrate the manufacturing of unitized stiffened panels because of a few key advantages. These advantages are that the method consistently produces high-quality, aerospace-grade specimens as determined in Chapter 3, the VARTM process requires little equipment besides the mold, hand tools, consumable infusion media, and a vacuum pump, and minimal post-manufacture processing is required before the stiffened panels were experimentally tested. Trimming the panel's four edges are all that were done to the panel

prior to test instrumentation. No secondary machining or stiffener bonding process was used to manipulate the stiffeners.

CHAPTER 3

Triaxial Braid Composite Characterization

3.1 Introduction

Many of the challenges researchers encounter with composite structures stems from a lack of understanding the fundamental constituents and the interaction beyond simple superposition between them [10]–[12]. As TBC textiles are not as widely used as other materials like unidirectional prepregs, especially when combined with the VARTM manufacturing method, fundamental characterizations prove useful in understanding the manufacturing as well as for further analysis and computational efforts. This chapter overviews two main studies performed on the TBC material. The first is a characterization of the VARTM manufacturing method for the TBC textile material itself. Flat plate specimens, as outlined in the manufacturing chapter, are investigated for fiber- and void-volume fraction. The specimen global fiber volume fraction is used to help determine the potential ranges of tow volume fraction, V_t, when used in conjunction with the individual tow fiber volume fraction, V_f. It should be noted that the tow volume fraction is defined to be the volume occupied by fiber tows within a representative unit cell or volume element. The idealized geometry of the braided architecture in numerical modeling outlined in Chapter 5 can make matching the as-manufactured tow volume fractions difficult without exhaustive developmental effort [2], [13]–[16]. Yushanov in [14] developed a stochastic modeling approach to quantify the effects of misaligned or

wavy fibers compared to the idealized straight or perfect paths. Huang in [15] implemented a method of separating fiber tow paths into linearized segments and summing the stress contributions in a piecewise manner to obtain the effective stiffness for highly curvilinear fiber paths. The void volume fraction, V_v, is a useful parameter by which different manufacturing methods and composite constituents can be compared. Void volume fraction is defined as the ratio of void volume to the volume of the entire RVE being inspected. Voids arise for various reasons including off-gassing during the curing stages [17], insufficient fiber wetting, or gas getting trapped between lamina during layup. The lower the void volume for most composites, the higher the quality as voids are often undesirable. Voids may be viewed as imperfections within the material and may lead to early damage initiation or propagation locations. Certain materials such as foams used in foam core sandwich structures are based on voids being desirable; however, this work treats them as undesirable.

The tow-level fiber volume fraction is inspected optically by sectioning a fiber tow perpendicularly to view the cross section. The cross-section is then polished and imaged under an optical microscope. A custom analysis script using the software program Matlab [18] is used to analyze the image based on the greyscale value for each pixel. An open source image analysis program called ImageJ [19] available from the National Institute of Health also was used to perform similar tasks but with added functionality through image enhancement toolboxes.

Lastly, a study measuring the geometric imperfections of the as-manufactured unitized stiffened panels is discussed. A coordinate measurement machine (CMM) laser scanner onsite at NASA Langley Research Center is used to scan the accessible surfaces of all eight unitized stiffened textile composite panels. The as-manufactured information collected is then aligned to a nominal model and processed to be used in the modeling efforts outlined in 5.6 and 5.7. This data proved useful by increasing the agreement of the postbuckling stiffness for both TBC 30 and 60 stiffened panels. The nominal model section thicknesses resulted in under predicting the TBC 30 postbuckling stiffness while over predicting the TBC 60 postbuckling stiffness. The corresponding as-manufactured section thicknesses support this trend as the TBC 30 sections were typically at or slightly

thicker than the nominal thickness while the TBC 60 sections were typically at or slightly thinner than the nominal model thickness.

3.2 Fiber Volume Fraction

Two methods of obtaining the fiber volume fraction are used in this work, though each method returns a different fiber volume fraction as the architecture dependency of the underlying material makes a broad term like fiber volume fraction less descriptive. An acid digestion test is used to determine the total ratio of fiber volume to RVE volume. This global parameter provides a value inclusive of all fiber tows and does not provide architecture specific values for individual axial or bias tows. The acid digestion fiber volume fraction is a good indicator of tow nesting when used in combination with the optical inspection tow fiber volume fraction. With the tow-level fiber volume fractions already known, the fiber volume fraction returned by the acid digestion can be used to determine the effective pure resin rich volume fraction. Tow volume fraction, or the ratio of tow volume to total specimen volume, is often difficult to obtain for manufactured specimens and can often be determined using idealized geometric models from CAD programs [2], [20]. A representative model is created that aims to capture the tow paths and cross-sections of the real specimen. From this model, CAD programs can easily return the volume of the tow and the total model volume to obtain the tow volume fraction. The difficulty with this method is in generating a model that is truly representative of the physical specimen. Fiber volume fraction of the axial and bias tows are optically determined Cross-sections of each type of tow are cut, polished, and imaged. The ratio of fiber to surrounding matrix may then be determined as approximated by the ratio of light and dark pixels in each image.

3.2.1 Acid Digestion

An acid digestion test was conducted according to ASTM D3171 [21]. Acid digestion was preferred over a fiber burnout procedure due to the concern over fiber oxidation potentially skewing the results. Fiber burnout measurements are more common in glass fiber reinforced composites because glass fiber is not affected by high-temperature oxidation as much as carbon fiber. Two sets of samples were digested to

obtain the results. Set I was composed of 0.25” x 0.25” small blocks of VARTM manufactured TBC 30 and 60 materials. Set II was composed of larger individual samples of both TBC materials measuring 0.25” x 1.0”. The sets were split up further between TBC 30 material samples labeled A-# and TBC 60 material samples labeled B-#. The inputs required to make the calculations were the initial specimen mass, the specimen mass in water, the temperature of the water, and the mass of the specimen after the matrix has been digested. The calculated outputs were the specimen matrix volume ratio, fiber volume fraction, and void volume fraction.

As provided in Table 3.1, the matrix volume fraction, Vm, global fiber volume fraction, Vf, and void volume fraction, Vv, are fairly consistent between the three digested samples. The TBC 30 material fiber volume fraction averaged near 54%. The void volume fraction is good at around 0.6%. This means that less than 1% of total volume is comprised of voids, and 1% is a common limit in the aerospace industry. Table 3.2 shows that the fiber volume fraction for the TBC 60 material in Set I averaged approximately 49%, with the void volume fractions varying from 0.1026% to 1.050%. Set II data are provided in Table 3.3 for TBC 30 material and Table 3.4 for TBC 60 material. The larger digestion sample sizes averaged near 56% compared to the 54% of the small samples from Set I. The void volume fraction is still excellent at much less than 0.5% for TBC 30 specimens. The TBC 60 large samples were more consistent in the returned fiber volume fractions with an average near 52% compared to 49% with the smaller samples. The void volume fractions are still less than 1% for five out of six tests. Carbon fiber composites are often classified as “void-free” if the void volume fraction is less than 1% [21]. Therefore, from the acid digestion results, using the VARTM manufacturing method consistently resulted in samples with small void volume fractions. Vacuum pressure during the manufacturing process is important in achieving large fiber wetting and therefore removing many of the voids in the final composite material.

Table 3.1: TBC 30 0.25” x 0.25” acid digestion results

		A-1	A-2	A-3
Set I	Vm (%)	45.37	44.83	45.25
	Vf (%)	54.05	54.63	54.01
	Vv (%)	0.5743	0.5392	0.7387

Table 3.2: TBC 60 0.25” x 0.25” acid digestion results

		B-1	B-2	B-3
Set I	Vm (%)	48.84	48.94	51.51
	Vf (%)	51.06	50.19	47.44
	Vv (%)	0.1026	0.8669	1.050

Table 3.3: TBC 30 0.25” x 1.0” acid digestion results

		A-1	A-2	A-3
Set II	Vm (%)	43.88	43.26	45.30
	Vf (%)	56.04	56.61	54.33
	Vv (%)	0.0763	0.1334	0.3699

Table 3.4: TBC 60 0.25” x 1.0” acid digestion results

		B-1	B-2	B-3
Set II	Vm (%)	47.27	46.94	47.46
	Vf (%)	52.09	52.49	51.52
	Vv (%)	0.6382	0.5765	1.026

3.2.2 Optical Inspection

Cross sections of axial and bias tows were sectioned, polished, and imaged to be used with imaging analysis software to optically determine tow fiber volume fractions. Figure 3.1 shows a collage of many local photos used to determine axial tow fiber volume fractions within a TBC 30 material sample. Note that the bias tow fiber volume fractions must be obtained using a different sectioned specimen as the bias tows are not cut perpendicularly to the fibers and therefore return erroneous fiber ratio values.Tow-level fiber volume fractions for TBC 30 and 60 materials in the axial and bias tows are provided in Table 3.5.

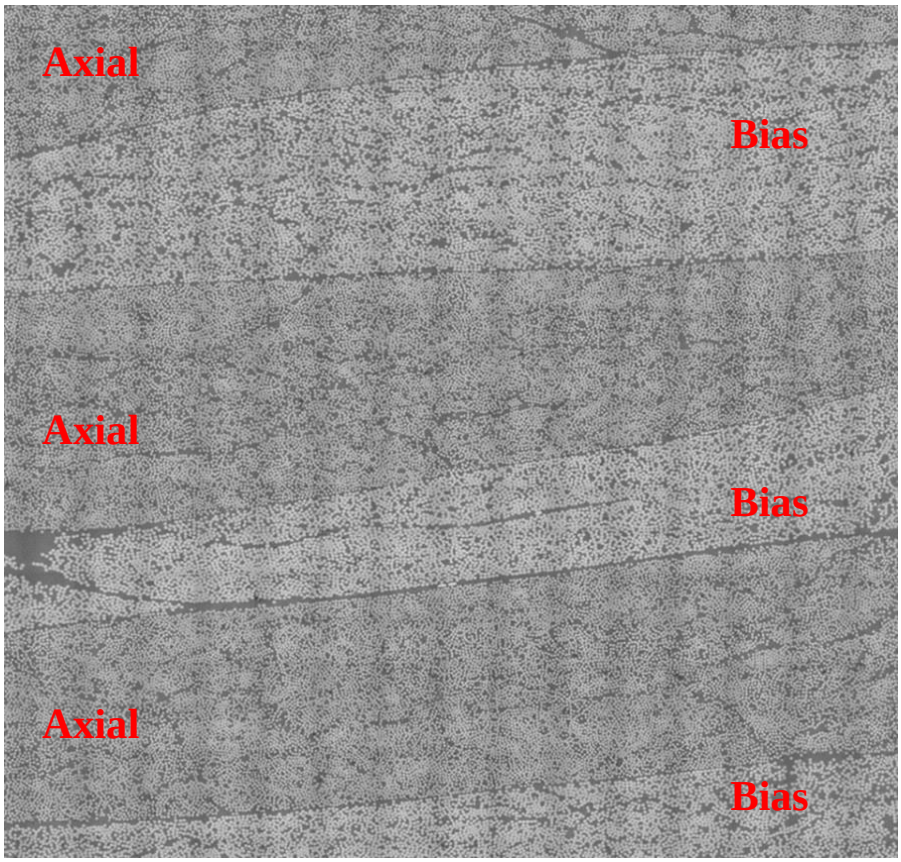

Figure 3.1: Sectioned, polished, and imaged TBC 30 material showing a collage of many individual photos used for axial tow fiber volume fraction calculation

Table 3.5: Optically determined tow fiber volume fractions for TBC 30 and 60

	TBC 30	TBC 60
Axial Vf (%)	72.2	64.0
Bias Vf (%)	68.1	57.6

When compared to the values reported in [20] of TBC 30 axial and bias tow volume fractions of 77% and 71%, respectively, and TBC 60 axial and bias tow volume fractions of 62% and 54%, respectively, the TBC 30 fiber tow volume fractions are slightly lower while the TBC 60 tow fiber volume fractions are slightly higher. Possible explanations for the differences arise in the different manufacturing methods used between both investigations. The current VARTM panels increase tow nesting and result in less volume occupied by resin rich areas, but the tows themselves may not necessarily

compress much, or at all, during the vacuum infusion process. Significant handling may also degrade the fiber sizing used to keep fibers within each tow bundled together, and repeated tow bending can break the hold of the sizing.

3.3 As-Manufactured Geometric Imperfections

Thin shell structures are often sensitive to geometric imperfections. Typically, flat plates are considered the least sensitive, while shallow shells, deep shells, and cylindrical shells increase in sensitivity in a spectrum [11], [22]–[24]. Using a Brown & Sharpe 12 15 10 laser coordinate measuring machine (CMM) at NASA Langley Research Center, the TBC 30 and 60 unitized stiffened panel surfaces were scanned to obtain geometric coordinate data. This data is processed into information that can then be used to characterize the as-manufactured imperfections into quantifiable terms. Each panel's seven sections were analyzed to determine the average section thickness. Significant differences between the nominal geometry and the as-manufactured specimens were observed. The section thicknesses varied from the nominal design, and the stiffener spacing was also typically different than that outlined in the nominal model. The section specific thicknesses play an important role in matching the load vs. displacement responses of the TBC 30 and 60 panels in the postbuckling computational loading. The geometric imperfection and section thickness work is discussed in the rest of section 3.3.

3.3.1 Coordinate Measurement Machine

The CMM laser scanner uses non-contacting reflected electromagnetic waves to record surface information. Figure 3.2 provides an example of what the scanning head of the CMM looks like as well as the laser scanning device in use. Note that the potted aluminum block is being scanned in the image as the alignment markers used to construct the fully 3D data set are attached to the block and not the specimen itself. The alignment markers used in this work are steel ball bearings. Discussion of the alignment process is in section 3.3.2.

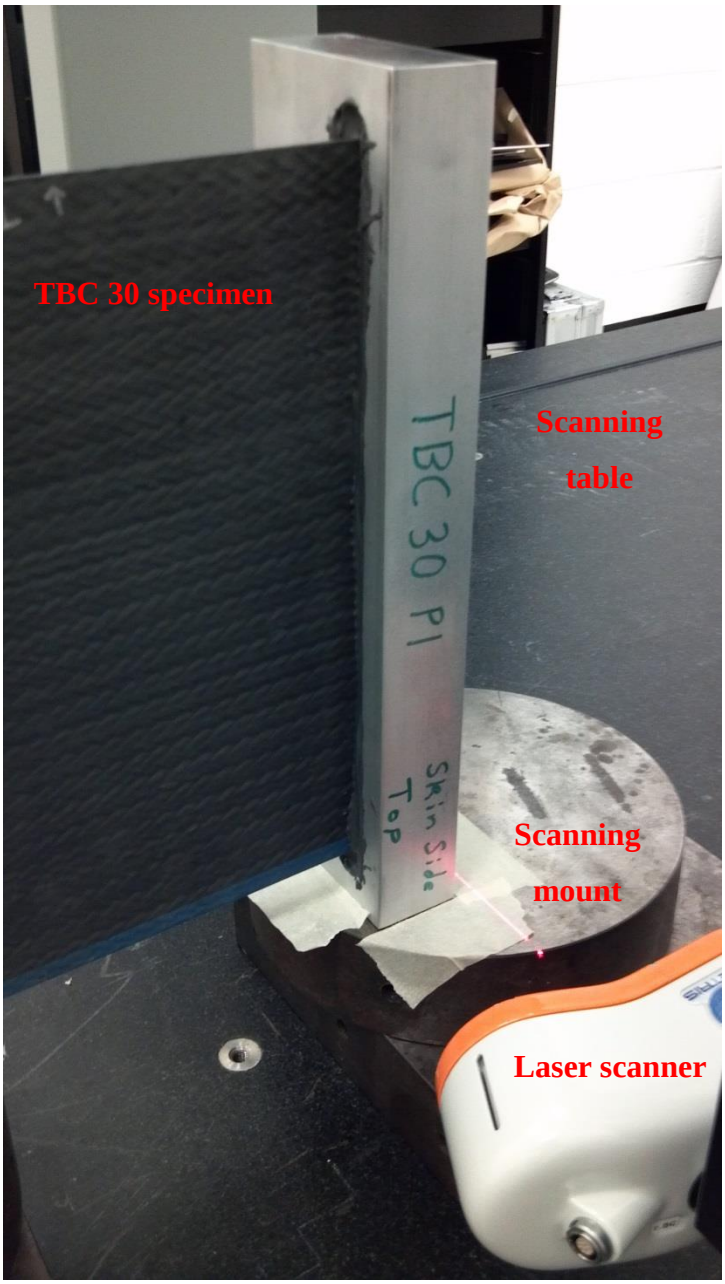

Figure 3.2: CMM scanning in progress capturing the potted block end boundary condition

The initial data captured after a scan is a simple point cloud in a 3D reference space. Markers or specimen features are used to assist alignment of multiple separate scans. In the case of the TBC panels, multiple scans were required as the dexterity of the scanning head was not sufficient to scan the complete panel at one time. The inside surfaces of the stiffeners and flanges proved particularly difficult to scan due to the

receiver potentially impacting the potted ends. No such impact was observed during data collection. As such, one complete interior flange surface could not be captured and half of the other flange interior surface could not be captured. Further discussion of the data processing is in section 3.3.2.

3.3.2 Data Alignment and Post-Processing

After scanning as much of the stiffened panel surface as possible, alignment of the individual scans created a single dataset of the entire panel in one 3D point cloud. Small ball bearings were glued to the aluminum potting blocks to aid the alignment process. The data processing software Focus Inspection [25] was able to recognize simple geometrical shapes such as spheres and use them as reference points by which to align and orient overlapping portions of partial scans. A minimum of three bearings on the skin side and three on the stiffener side were used. Reference spheres were fit using Focus Inspection to the sphere scan points, and a least-squares method was used to determine the best alignment.

Once the alignment of each individual scan was complete, each full 3D data cloud contained approximately 3.5 million data points representing the stiffened panel. As this large data cloud contained too many points to be feasible for processing in a timely manner, a filter was applied. This filter removed all excess data points from the full point cloud except at the specific interval. The filter interval was set so that a grid of data points would be kept, and the grid spacing set such that 50 points per inch were retained. This resulted in grid spacing of one point every 0.02 linear inch. 50 points per inch also was sufficient to resolve the as-manufactured surface texture resulting from fiber tow undulation and nylon peel-ply from the infusion media preform.

A nominal stiffened panel model was imported into the 3D data cloud and aligned to match the orientation of the scanned panels. Once the as-manufactured scanned data is aligned with the idealized geometric model, software tools within Focus Inspection are used to analyze certain data such as deviations from the nominal model. This comparison allows the user to learn how the as-manufactured specimen differs from the nominal model. Four TBC 30 panels labeled P1 through P4 and four TBC 60 panels labeled P1 through P4 were manufactured, scanned, and tested in this work. Figure 3.3 provides

color contours superimposed on the as-manufactured scan data for panel TBC 60 P1. The coloring denotes deviation away from the surface of the nominal model. Warmer colors indicate that a surface is farther away, while cooler colors indicate that a surface is closer to the corresponding nominal model surface. As seen in Figure 3.3, the three skin sections are generally close to the nominal model surface and are dominated by blue coloring. The stiffener sections, however, are much warmer colored and denote that the stiffener location is significantly different compared to the nominal model dimensions. The top flange sections are mixed.

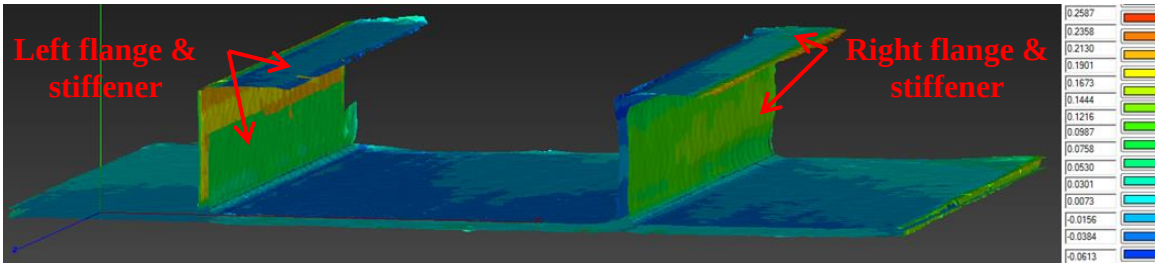

Figure 3.3: As-manufactured surface scan comparison contours to the nominal TBC 60 P1 stiffened panel design

The left flange in Figure 3.3 agrees well with the nominal model while the right flange deviates near the unsupported edge. For this specific panel, this flange edge deviation indicated that the flange is actually slightly wider than the flange in the nominal model and the scanned data is being referenced against the edge of the nominal model. Figure 3.4 shows the stiffener spacing difference by viewing along the stiffeners in a cross sectional view for panel TBC 60 P1. Note the location of the left stiffener is shifted by almost an entire thickness of the section.

Figure 3.4: Cross sectional view of the as-manufactured TBC 60 P1 panel data (red) and the nominal panel reference (blue) looking along the stiffeners

3.3.3 Section Fitting

In order to convert the as-manufactured vs. nominal data comparisons into data that can be implemented in analysis, each panel is divided into seven separate sections. The naming convention is based on whether the section is a skin, stiffener, or flange section. The location of the section is determined based on the widths of the closest skin section as all three skin sections vary in nominal width. The *narrow skin section* is on the left in Figure 3.4, while the *center skin section* and *wide skin section* are in the center and on the right, respectively. The *narrow stiffener section* would be the one on the left, as would the *narrow flange section*, too. The remaining sections are called the *wide stiffener section* and *wide flange section*, respectively.

The global aligned 3D data cloud is then divided by these sections so each section may be individually analyzed with a Matlab script. As each section cloud is now effectively a flat plate, the scanned points are analyzed to return the average section thickness. Since each section has two surfaces of data cloud points, the thickness calculation is based on comparing the differences in the through-the-thickness direction. A *for loop* over one surface of points is made. For each point on that surface, a search algorithm finds the point in the opposite point cloud that has the closest in-plane coordinates within a defined search area. The thickness parameter is then computed by averaging the out-of-plane coordinate values of the two points. This process repeats across all points on one surface, and at the end the thickness values are averaged to obtain the average section thickness value.

Figure 3.5 shows a representative example of how a point in one surface cloud (red point) searches for the closest match in the direction perpendicular to the plane of points of the section in the opposite surface data cloud (black points). All green dots are within the search area and are analyzed to determine the best fit. The dark green dot is determined to be the best match opposite the red dot, and the thickness is calculated between these two points. In this search algorithm, a new data point (blue) is also defined to be at the mid-point between the red and green data points. This new midplane surface is used to condense the 3D scanned data into a representative shell structure.

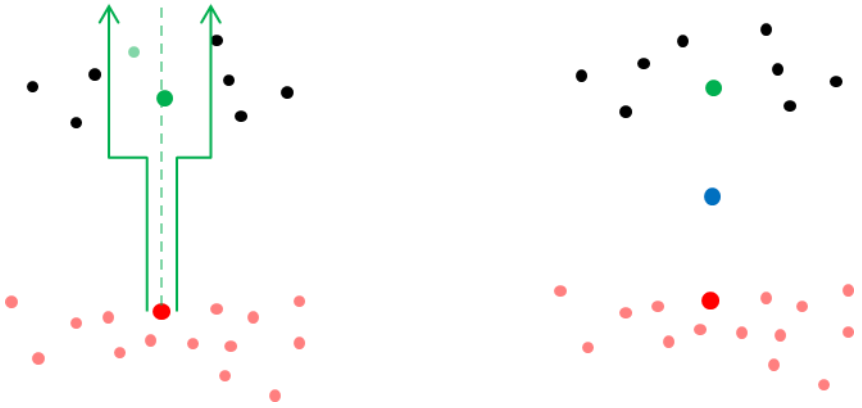

Figure 3.5: Section thickness search algorithm example

3.3.4 Section Thickness

After processing the seven sections for all eight stiffened panels, a trend in the as-manufactured geometry becomes clear. Specifically, in addition to the previously noted stiffener-spacing discrepancy, certain sections in the TBC 30 material panels were consistently thicker than the nominal model. Conversely, most sections in the TBC 60 panels were consistently thinner than the nominal model. These trends are consistent with all four panels of each material type. Also of note are manufacturing specific features resulting from the mold used to make the stiffened panel geometry.

Figure 3.6 shows a clear "ridgeline" in the middle of the center skin section. This manufacturing defect is a direct result of the split aluminum block mold insert used to create the stiffened panel geometry. Split-block inserts are used to be able to successfully remove each insert post-manufacturing without damaging the stiffened panel. The unsupported edge on the *narrow skin section* also has locations of higher thickness. This defect is more difficult to trace to the manufacturing, but it is thought that the free edges were not compressed as significantly under vacuum pressure as the centers of each section.

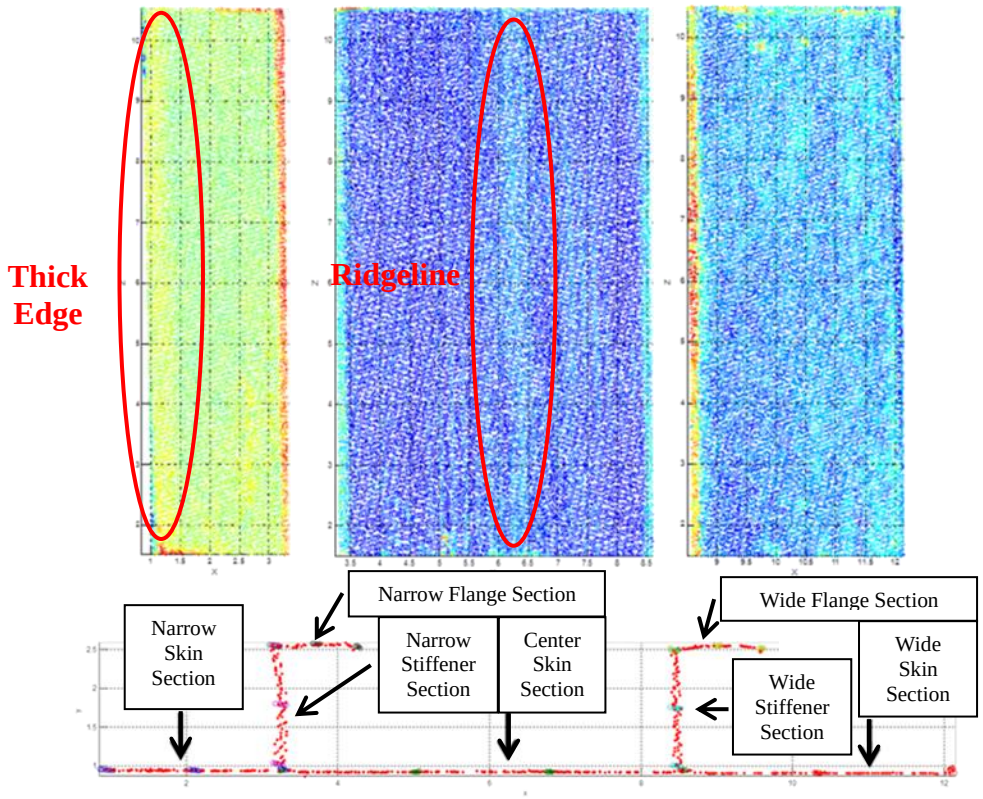

Figure 3.6: Skin section thickness noting manufacturing specific features resulting from the panel mold, not to scale

Figure 3.7 provides an example of the TBC 30 P1 section average thickness result of processing the as-manufactured TBC panels. Note that the skin sections are approximately equivalent to the nominal thickness, but both stiffener sections exhibit significantly larger thickness ranging from 2.980-mm to 3.178-mm. This trend was observed for all TBC 30 panels in that the stiffener and flanges were typically thicker than nominal while the skins were in line with the nominal model.

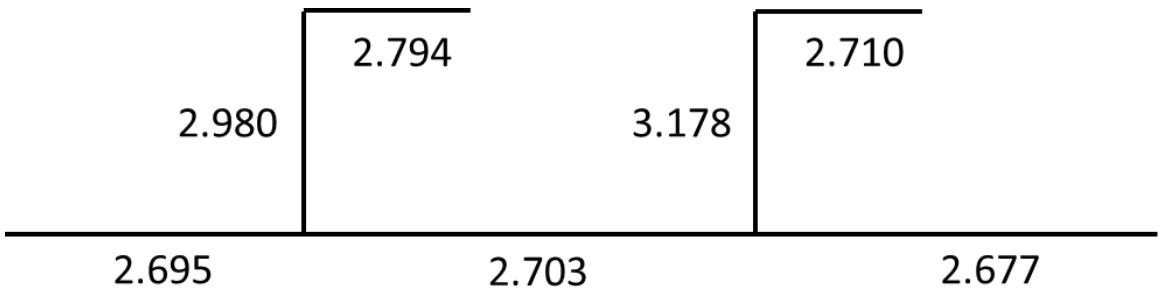

Figure 3.7: TBC 30 P1 section highlighting thicker stiffener and flange section thickness compared to the nominal model

Figure 3.8 provides an example of a TBC 60 section average thickness result after processing the as-manufactured panel TBC 60 P1. The section thicknesses for the TBC 60 panels as a whole are thinner than those for the TBC 30 panels. The *wide stiffener section* is typically the thickest section in each respective panel regardless of whether it is a TBC 30 or 60 panel, but the TBC 30s are thicker than the TBC 60 sections. The *wide stiffener section* thickness is most likely a direct effect of the manufacturing mold used to create the stiffener geometry. Each panel section average thickness is incorporated into a computational model and these results are discussed in section 5.8.

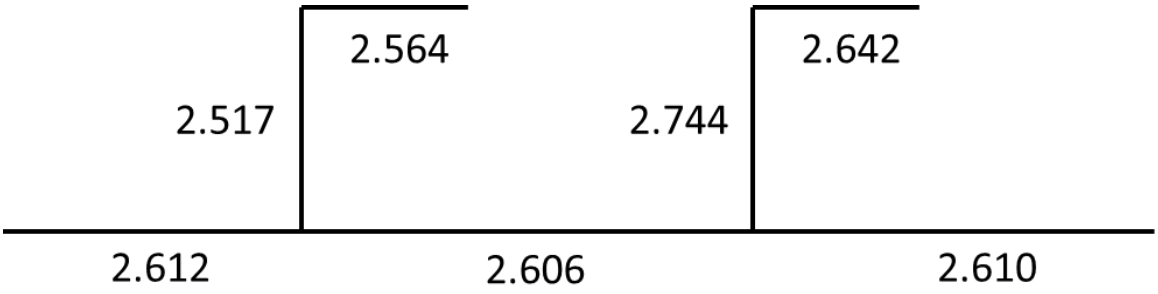

Figure 3.8: TBC 60 P1 section highlighting thinner sections compared to the nominal model

Table 3.6 provides all section average thickness values for each TBC 30 and 60 stiffened panel. Note the change in average thickness of the TBC 60 panels compared to the TBC 30 panels. Tow nesting, the tendency and degree of fiber tows to rest adjacent to each other, is much more dominant in the TBC 60 material. Higher levels of tow nesting was also observed for other TBC 60 based specimens such as the flat plates used for the characterization specimens in previous sections. Note that the *wide stiffener section* is the thickest in all TBC 30 and two of four TBC 60 panels. That section is over 3-mm for TBC 30 P1, P2, and TBC 60 P4. TBC 60 P4, however, has significantly thinner skin thickness averages for the remain skin and flange sections ranging from 2.272-mm to 2.520-mm. Despite the quality of the infusion process as previously mentioned, the table data highlight the lack of thickness control in the outlined VARTM method. To improve thickness consistency, spacers or other thickness control devices should be incorporated. Thickness tolerances are important in flight structures not only from a performance perspective, but also in the assembly and use of the final structure.

Table 3.6: TBC 30 and 60 individual average section thickness values

	TBC 30 (mm)				TBC 60 (mm)			
Section	P1	P2	P3	P4	P1	P2	P3	P4
Narrow Skin	2.695	2.691	2.690	2.647	2.612	2.564	2.578	2.322
Center Skin	2.703	2.729	2.702	2.774	2.606	2.645	2.580	2.362
Wide Skin	2.677	2.668	2.680	2.555	2.610	2.664	2.547	2.272
Narrow Flange	2.794	2.803	2.791	2.812	2.564	2.518	2.492	2.459
Wide Flange	2.710	2.705	2.711	2.692	2.642	2.508	2.476	2.520
Narrow Stiffener	2.980	2.911	2.813	2.902	2.517	2.676	2.513	2.708
Wide Stiffener	3.178	3.442	2.987	2.993	2.744	2.651	2.507	3.028

3.4 Summary

Various characterization methods were used to obtain important information on the manufacturing quality, constituent parameters, and as-manufactured geometric imperfections of the unitized TBC 30 and TBC 60 stiffened panels. Acid digestion tests demonstrated that the VARTM manufacturing process resulted in excellent quality panels on a void volume fraction basis as most void fractions were well below 1%. Optical inspection via sectioning, polishing, imaging, and analyzing with image software showed that the VARTM TBC 30 and 60 materials were up to 5% lower in local tow fiber volume fractions compared to other TBC material manufactured using a high pressure infusion method. The VARTM method did, however, increase fiber tow nesting and reduce overall resin rich areas in the TBC materials. A laser scanning CMM device was used to collect, process, and characterize the VARTM manufacturing method and difference between as-manufactured and nominal panels. The TBC 30 panels were found to have thicker stiffener and flange sections as compared to nominal. The TBC 60 panels had thinner sections overall compared to nominal. The average section thickness collected on the as-manufactured panels is implemented in the computational modeling efforts discussed in later sections.

CHAPTER 4

Triaxial Braid Composite Experimental Investigations

4.1 Introduction

Carbon fiber textile composite structures can offer distinct advantages over other composites across many industrial applications including aerospace, automotive, and recreational markets. One common challenge of using textile composite materials is the designers', manufacturers', and engineers' relative unfamiliarity with the material compared to unidirectional composites, for example. Textile composite material, whether woven, braided, knitted, or other, can be thought of as a structural material itself where the components are many bundles of individual fibers. The widely used concentric cylinder model produces good agreement for straight fiber composites, but the undulating nature of textile composites requires further analysis to capture accurate material properties. Analytical decomposition [2] of textiles like woven or braided materials considers tow-level component analysis contributing to the overall textile material global properties. Therefore, an analyst must remain aware of exactly what is required to characterize material properties for such materials lest the tests return misleading values.

The following sections outline experimental tests conducted to characterize unknown or questioned properties of the VARTM manufactured TBC material used to make the unitized stiffened composite textile panels. The first is a non-aerospace-industry-standard test to determine the in-plane shear modulus, G_{12}. This test is better

suited than other industry standard tests like rail-shear tests because it attempts to remove material orientation effects from coarse aggregate-sized materials like textiles and composite wood structures, among others.

The second outlined test is used to characterize the material nonlinearity of the in-situ matrix in TBC specimens. It is well known that in-situ matrix properties may vary from pure, virgin matrix material properties commonly provided by material manufacturers [26]. Differences in properties arise due to the matrix curing in the presence, or absence, of reinforcing fibers. Residual thermal stresses from the manufacturing process often invalidate the assumption that an unloaded material is considered to be in a stress-free state [27]. While it may be valid in a global sense of the specimen, it is not the case on a local, constituent level. The results of the nonlinear in-situ matrix characterization tests are used to enhance the mesoscale model discussed in section 5.4 to include material nonlinearity and successfully capture the observed experimental tow failure behavior.

The third test conducted in this work provides the experimental validation of the unitized stiffened textile composite panel concept as outlined in section 1.3. The stiffened panels were loaded in axial compression well into postbuckling until failure, and a complete loss of load carrying capability was observed. An overview of the test setup, instrumentation, naming conventions, experimental results for TBC 30 and TBC 60 panels, and results of the failure investigation are given.

4.2 Anticlastic Plate Bending Tests

Previous work in characterizing TBC textiles manufactured using a high-pressure infusion method included in-plane shear modulus, G_{12}, characterization using double-rail [20] test fixtures. While this test is an industry standard, the results varied as the orientation of the material proved significant in the returned shear modulus value i.e. $G_{12} \neq G_{21}$. When the axial tows were aligned parallel to the direction of loading in the double-rail fixture, most of the shear was carried by the bias tows only. However, by rotating the material 90 degrees and having the axial tows perpendicular to the loading direction, a significantly different modulus was obtained. This discrepancy was determined to be caused by the carrying of load by the axial tows when aligned

perpendicularly to the test loading and not carrying significant load when aligned parallel to the test loading. The effective number of loaded fibers changed between orientations. As the shear modulus was still vague in value, another test [28], [29] aimed to determine G_{12} independently of material orientation was conducted on the VARTM manufactured TBC material.

Figure 4.1 shows the analytical loading condition using distributed, opposing moments and the equivalent loading condition when the four corners are under point-forces. Such anticlastic curvature results in the very center of the square plate experiencing a state of pure shear. From the experimental data collected, which consists of just the load and corner displacement, the shear bending stiffness term D_{66} can be calculated using equation (4.1).

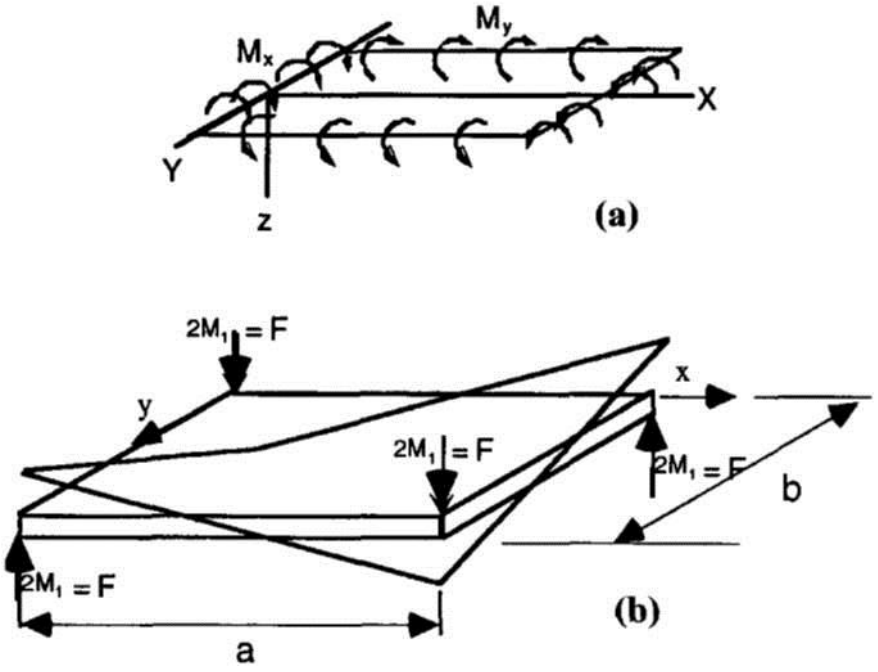

Figure 4.1: Applied opposing moment diagram (a) and equivalent opposing corner load (b)

$$D_{66} = \frac{PL^2}{4w_c} \qquad \textbf{(4.1)}$$

Where P is the load on each corner of the square specimen, L is the specimen side length, and w_c is the corner displacement from the unloaded configuration. With the shear bending stiffness calculated from experimental data, one can turn to the definition of the D_{ij} terms from classical lamination theory using equation (4.2).

$$D_{ij} = \frac{1}{3}\sum_{k=1}^{N}\left(\overline{Q}_{ij}\right)_k (z_k^3 - z_{k-1}^3) \quad \textbf{(4.2)}$$

Where $\overline{Q}$ is the lamina stiffness matrix rotated to the principal material frame. The shear modulus can then be calculated from this value as the principal material frame and the specimen frame are aligned. Once the $\bar{Q}_{66}$ term is calculated from the D_{66} value obtained from equation (4.1), it is equivalent to the in-plane shear modulus due to the aligned coordinate frames.

The tests were conducted on the Shore Western axial load frame in the Composite Structures Laboratory at the University of Washington. The load cell in this frame is rated for 35,000 pounds. Figure 4.2 provides a broad view of the plate bending shear test fixture as implemented in the Shore Western load frame. In the bottom pair of grips is an insert that has two slide-adjustable point supports. The top pair of grips has a similar insert, except the slide-adjustable point supports are much longer to accommodate external data acquisition equipment such as the linear variable differential transformers (LVDTs) as seen in Figure 4.2. As the expected loads are less than 200 N, bending of the longer supports is negligible. Using the corner deflection data combined with data recorded by the load cell is the generally accepted way to extract the in-plane shear modulus as it is based on fundamental structural mechanics. There is a second method of determining the shear modulus that has been documented, and the LVDTs are only used for this second method. One LVDT collects the displacement of the center of the top surface of the specimen. The other LVDT collects the displacement of one-quarter the diagonal of the specimen. Which diagonal is used does not matter as it is only the relative displacement between the two locations that are significant. An example of the center and quarter diagonal collection locations is shown in Figure 4.3 As the data needed for both methods could be collected at the same time during each test, each method could be

compared as to the consistency of the shear modulus each reduction method returned. The LVDTs were used in this test to compare published data reduction methods used for other composite materials [29] such as manufactured wood products. However, other work [28], [30] has shown that this secondary data method using the LVDTs can return inconsistent values for the shear modulus and range anywhere from 20%-50% higher than the actual shear modulus depending on the type of material being used.

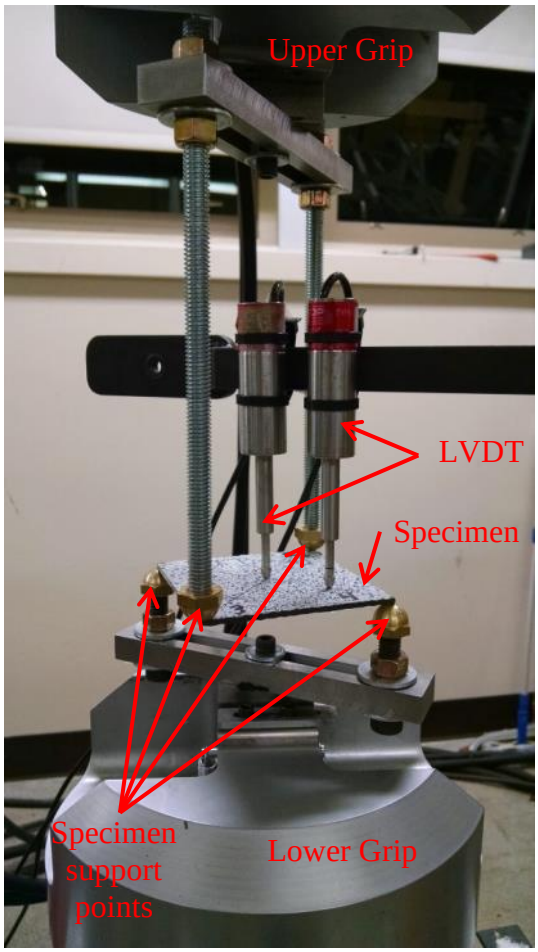

Figure 4.2: Anticlastic plate bending shear test fixture setup

For thin plates, defined here by the thickness to side length ratio of 20 or greater, the corner displacement data reduction method is typically the most accurate. The coupons tested in this study satisfied the thin plate ratio. One square specimen was cut from each of TBC 30 and TBC 60 material. Figure 4.3 shows an example of a loaded TBC 30 specimen where the opposing corners of the square plate are bending in similar directions.

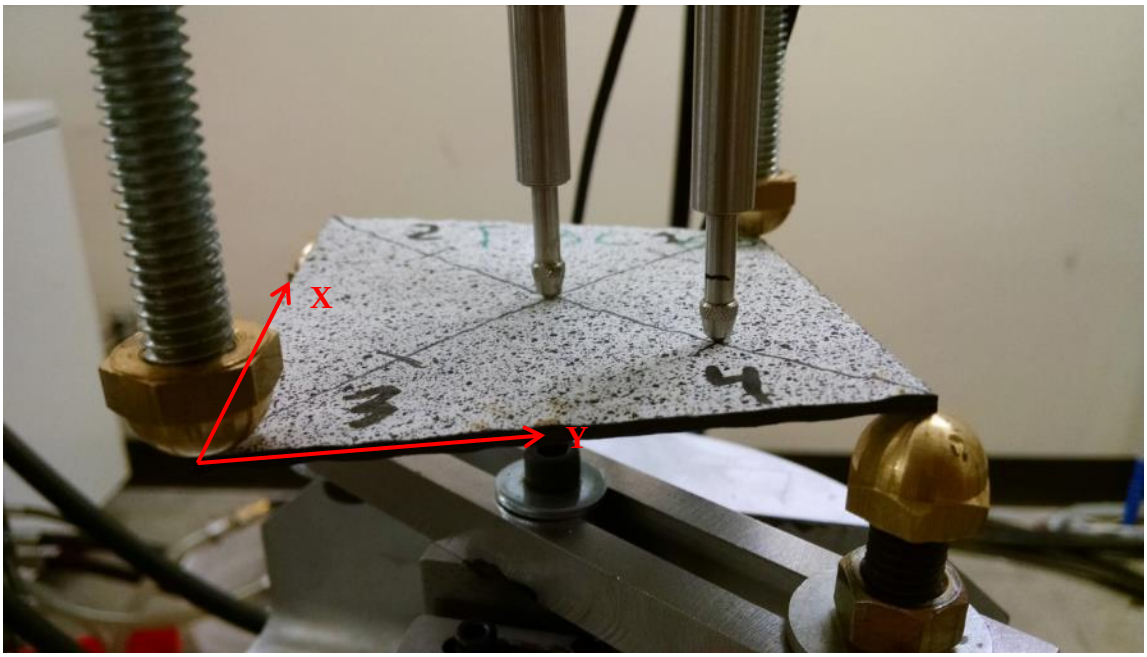

Figure 4.3: TBC 30 square coupon bending under load in orientation "1"

Each coupon was tested twice, with the second test having been rotated by 90° clockwise within the test fixture to demonstrate material orientation independence. The tests labeled as Test-2X were conducted in this rotated orientation where labels of Test-1X denote the original orientation. Figure 4.4 shows an elevated perspective with the corners rotated relative to the orientation shown in Figure 4.3. For each material coupon in each orientation, tests were conducted twice to ensure repeatability and that the material's linear-elastic range was not exceeded.

Table 4.1 provides basic geometry data for each of the TBC material coupons that were tested in the shear modulus characterization. The third column provides the averaged in-plane shear modulus G_{12} for the four tests recorded per specimen. This G_{12} value is found from the method using the corner displacement data. The last column provides the previously reported values as obtained by the rail-shear tests [20].

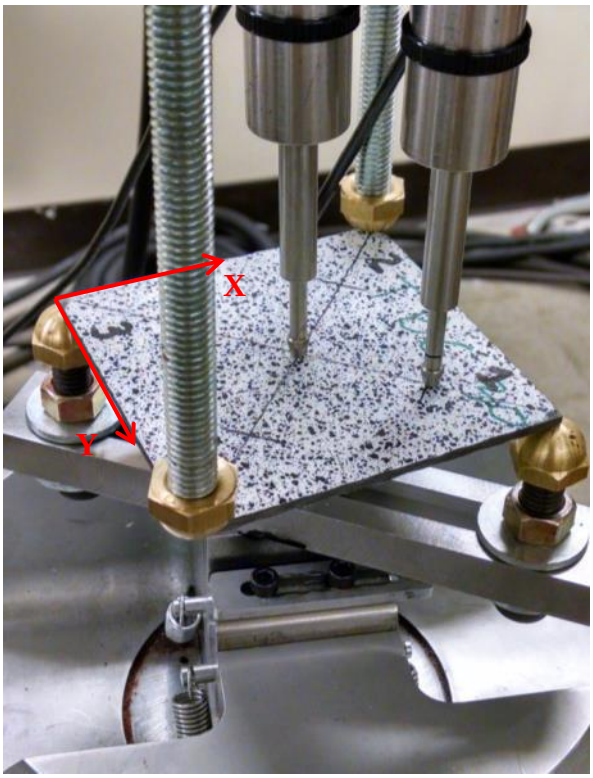

Figure 4.4: Test coupon showing the rotated orientation for the second set of tests to determine material orientation independence

Table 4.1: Data on anticlastic plate bending square coupons

	Side length (mm)	Thickness (mm)	G_{12} (GPa)	Previous G_{12} (GPa)
TBC 30 Specimen	85.10	2.7	8.86	9.3
TBC 60 Specimen	84.07	2.11	11.5	11.8

Over all there is good agreement with the anticlastic plate bending test with the rail shear tests for the TBC 60 material. The TBC 30 material returns a lower modulus by approximately 0.5 GPa compared to the rail-shear tests. As seen in Figure 4.5, all four tests with the TBC 30 coupon show nearly identical load-displacement behavior.

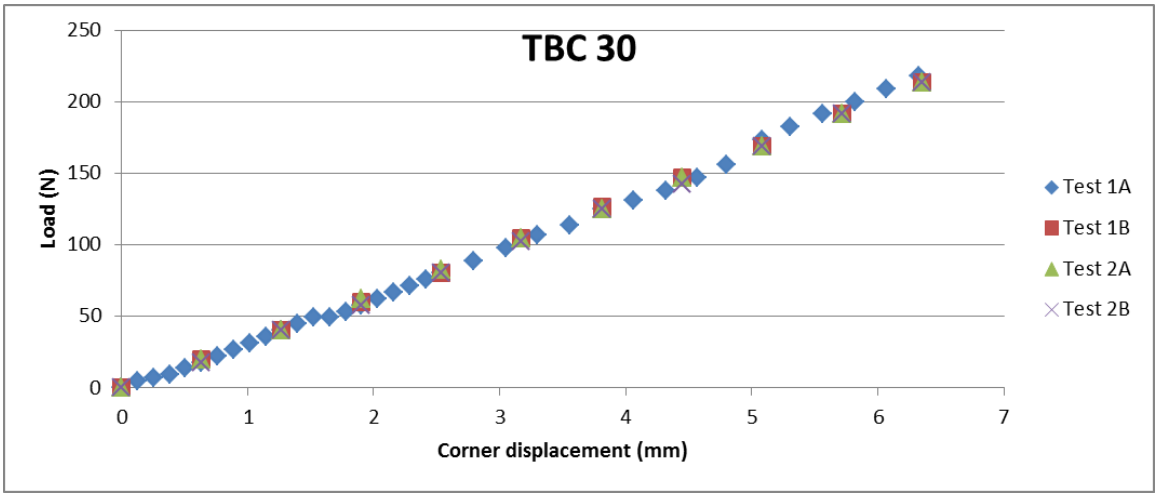

Figure 4.5: TBC 30 coupon load-displacement curves

Figure 4.6 and Figure 4.7 show the calculated shear modulus plotted against corner displacement for the two data reduction methods using the corner displacement data (Wc) and the LVDT data. For example, Test 1A produces two sets of calculated in-plane shear modulus. The set labeled Test 1A-Wc uses the corner displacement whereas set Test 1A-Wlvdt uses the LVDT data reduction method. Note Test 2X in Figure 4.7 were in the rotated configuration. Note that the LVDT data return larger shear moduli values and are in line with the 30% overestimation as previously discussed. There is excellent agreement within each method, but only the corner displacement method is used due to the overestimation potential noted previously.

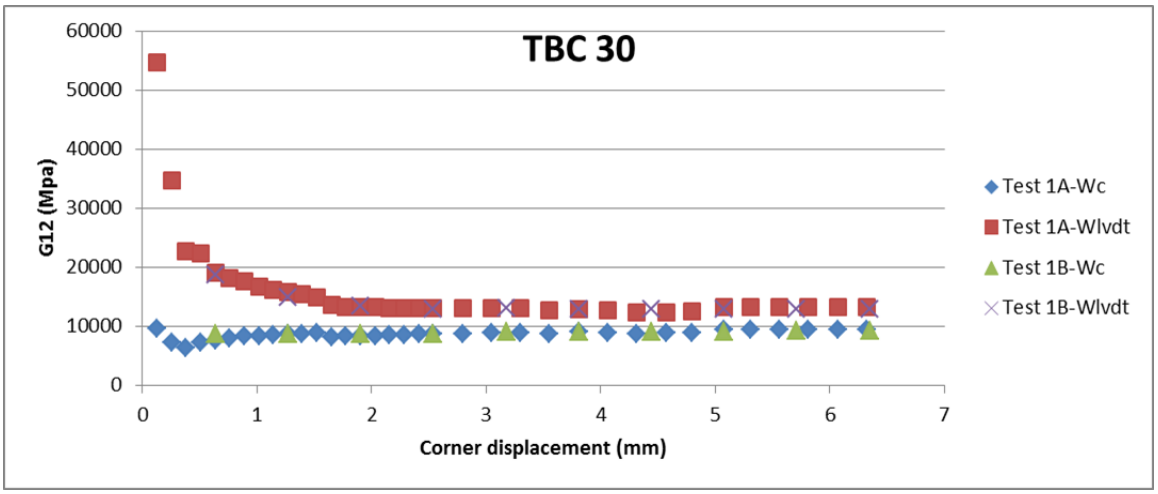

Figure 4.6: TBC 30 Test 1 calculated shear moduli

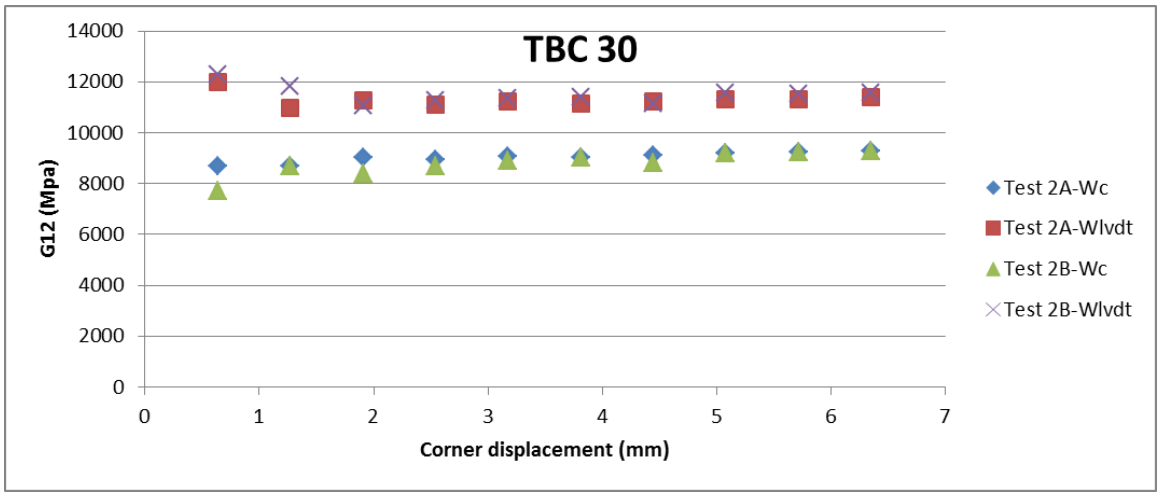

Figure 4.7: TBC 30 Test 2 calculated shear moduli

Figure 4.8 shows the load-displacement behavior for the TBC 60 coupon. There is more scatter in the data compared to the TBC 30 coupon across the four tests, however agreement is still reasonable as the calculated shear moduli show in Figure 4.9 and Figure 4.10.

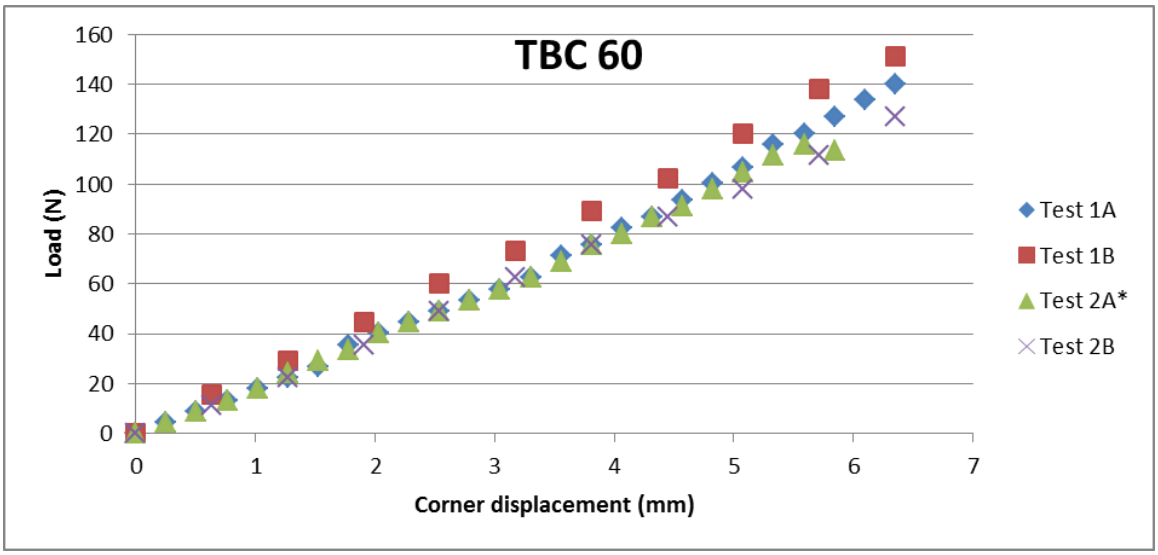

Figure 4.8: TBC 60 coupon load-displacement curves

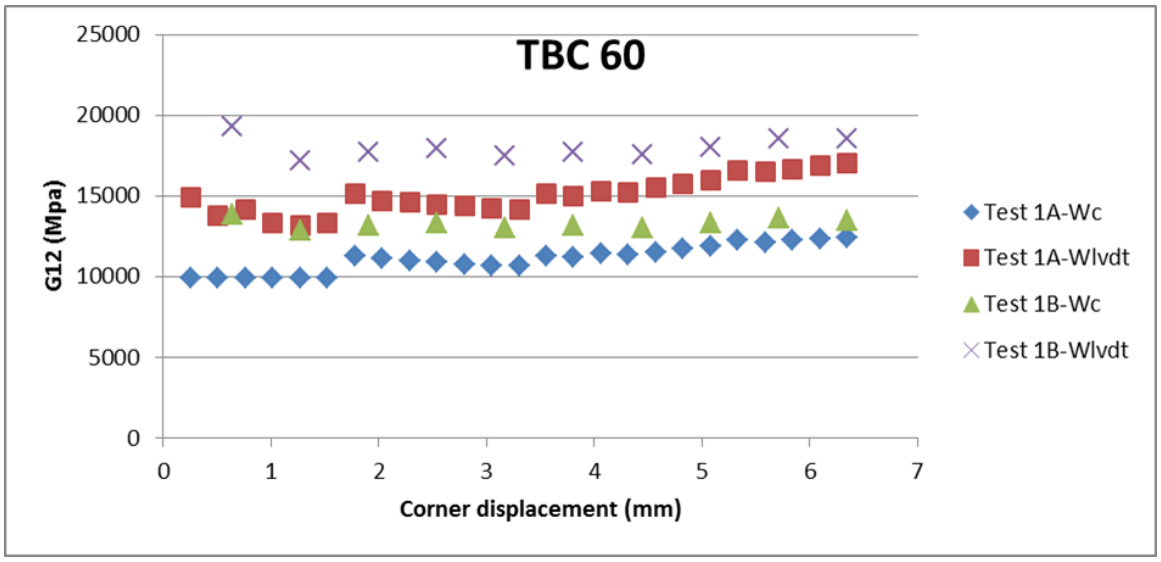

Figure 4.9: TBC 60 Test 1 calculated shear moduli

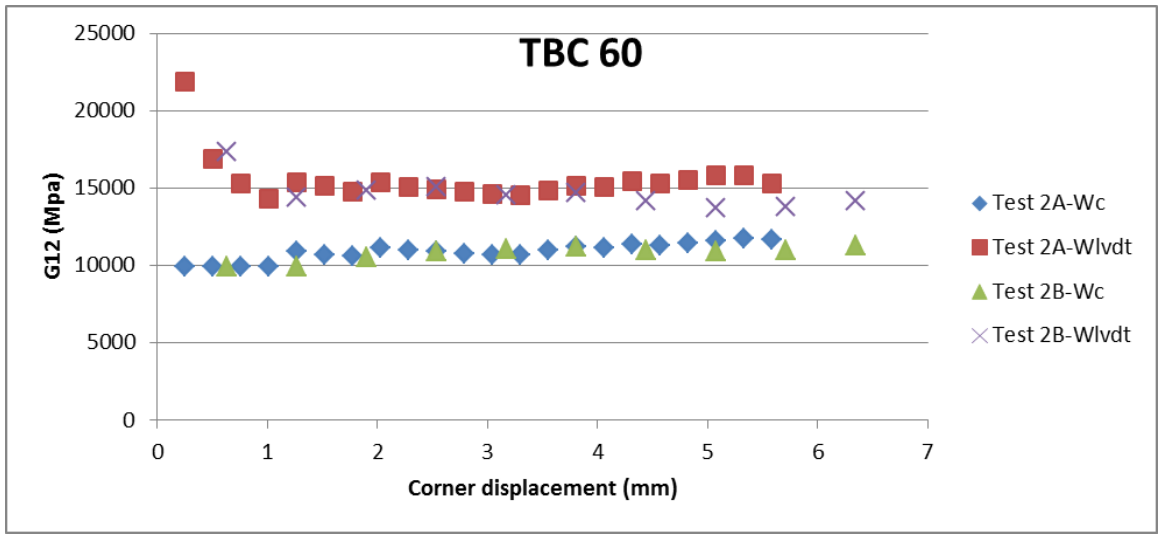

Figure 4.10: TBC 60 Test 2 calculated shear moduli

The values of the shear modulus tend to converge at higher values of corner displacement for both orientations of the TBC 30 and TBC 60 specimen. There is large scatter at small displacements for TBC 30 Test 1X and TBC TBC 60 Test 2X LVDT method's data due to the relatively small displacements in the LVDT reduction method. Since the corner displacement reduction method uses the loadframe displacement data instead, the values of relative displacement are at a magnitude where there is less

sensitivity of dividing by an extremely small number. The linear-elastic check for TBC 60 Test 1B observed a systematic offset in the value of the shear modulus compared to Test 1A. This offset is believed to come from an initial unseated position within the test fixture. Due to the undulating nature of the TBC textile composite specimens, it was possible that a corner did not fully come in contact with the fixture support upon initial loading. However, the initial offset seen in Test 1B was not a concern for two reasons. The first is that the value for the shear modulus did approach a value similar to that obtained from Test 1A at sufficiently large corner displacements where an unseated corner would have come in contact with the support and become loaded. The second reason the offset is not a concern is that the specimen was observed to still behave in a linear elastic manner as observed by TBC 60 Tests 2A and 2B conducted after Tests 1A and 1B. If any material nonlinearity was occurring, the data from Tests 2A and 2B would have deviated in the load-displacement curves in Figure 4.8 as well as resulting in a significantly different calculated shear modulus. Therefore, the data from both sets of tests are useful in determining the shear modulus just like for the TBC 30 tests. Note that the data set for TBC 60 Test 2A terminates at a lower corner displacement than the rest of the tests. This was due to the specimen slipping within the test fixture and not due to an event such as failure.

4.3 Nonlinear In-Situ Matrix Characterization

When fiber reinforced composites are under compression, it has been shown that micro buckling or kinking [31] of the fiber tows is primarily a result of the nonlinear material behavior of the matrix surrounding the fibers [32] and the nonlinear structure-like behavior of fiber tows encased in matrix. The fibers themselves may still be in the linear elastic regime, but the local buckling behavior is a matrix-dominated response. Only after the kink has initiated are the fiber compression strengths exceeded and fiber failure occurs. The in-situ matrix has also been shown to behave drastically different from pure, virgin matrix material often tested and reported by material manufacturers [26]. As the main loading condition of the unitized stiffened textile composite panels is axial compression with fiber kinking, the nonlinear material behavior of the matrix is characterized [8], [33]. This information is used in the development of the TBC 30 and

60 representative volume element (RVE) as discussed later in section 5.4. The basis for this test comes from a characterization test of the initial shear modulus G_{12} by using a tension coupon of $\lfloor \pm 45° \rfloor_S$ unidirectional fibers [34], [35]. By extending this method into the non-linear regime, the in-situ equivalent stress-equivalent plastic strain curve is obtained. Flat TBC 45 coupons, where the bias braid angle is 45°, were manufactured and then cut from a plate using a wet-saw. The TBC 45 material was deemed most appropriate to use instead of the TBC 30 or 60 materials because the 45° fiber tows would be in a state of shear stress when rotated into the bias tow principal material coordinate frame while the coupon itself is in axial tension.

4.3.1 Tests

Five TBC 45 rectangular coupons were manufactured and cut using a wet-saw. Each coupon measured a nominal 280-mm in length, 3-mm in width, and tabbed with 38-mm glass angled tabs to ensure sufficient gripping in the load frame. A 203-mm gage section resulted post-tabbing process. The 32-mm width was chosen to ensure at least 4 representative unit cells spanned the width of the coupon. Each specimen was painted with a black and while speckle pattern to use with digital image correlation (DIC) measurement techniques instead of physical strain gages. One significant advantage of DIC is the acquisition of full field strain measurements instead of local point measurements with strain gages.

Figure 4.11 provides an overview of the orientation of the TBC 45 material relative to the coupon dimensions and loading direction as indicated by the black arrows. Axial tension is taken to be in the global x-direction with the axial tows running perpendicular to loading and in the global y-direction. The shaded area indicates the majority of the gage section is used in the DIC software ARAMIS to capture the full strain field. All tests were conducted on the Shore Western load frame with 35,000 pound load cell in displacement control.

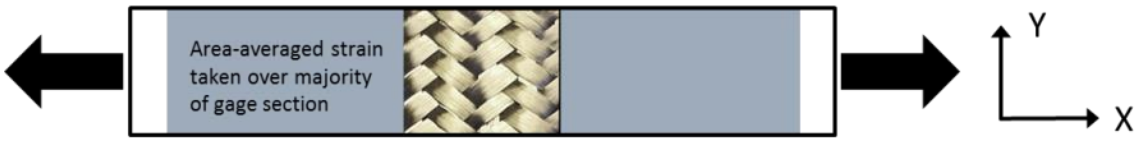

Figure 4.11: Tension coupon representative specimen outlining the direction of applied load relative to the TBC 45 material orientation

Each specimen was loaded until complete two-piece failure, and each specimen failed satisfactorily between the tabbed ends within the gage section. Figure 4.12 shows the simple tension coupon under load in the Shore Western load frame prior to failure. The white paper hanging behind the specimen aided image quality by removing background objects and focus was easier to maintain on the speckle pattern.

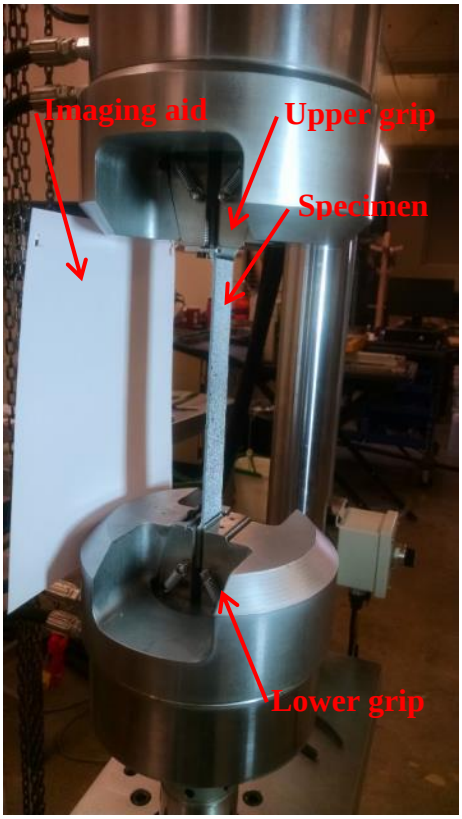

Figure 4.12: Axial tension setup

Five specimens were tested to failure, and Figure 4.13 shows the axial stress vs. axial strain curves after the DIC images were processed. Note the non-linear behavior

toward the end of loading is attributed to the formation and coalescence of matrix microcracks [35]. As the bias tows are oriented at ±45° to the loading direction, they are in a state dominated by shear stress.

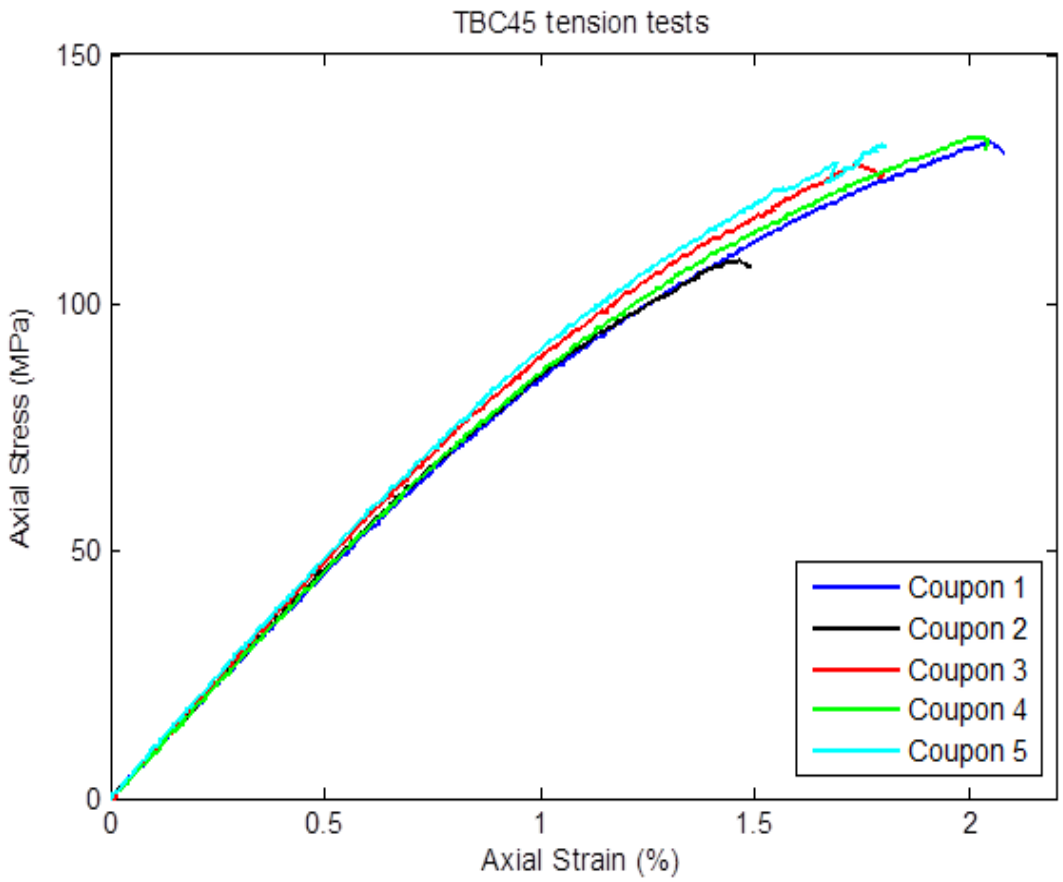

Figure 4.13: Axial stress vs. axial strain data curves for TBC 45 tests

4.3.2 Data Reduction and Post-Processing

After rotating to the principal material coordinate frame for the 45° bias tows, the shear stress, τ_{12}, and engineering shear strain, γ_{12}, are given by (4.3).

$$\tau_{12} = \frac{\sigma}{2}$$
$$\gamma_{12} = \varepsilon_x - \varepsilon_y \quad \textbf{(4.3)}$$

Note that axial stress, σ, axial strain, ε_x, and transverse strain, ε_y were all measured from the tests or calculated directly from data taken during the tests. From this data, the secant shear modulus G_{12S} can be calculated by the ratio of shear stress τ_{12} over shear strain γ_{12} and is given by (4.4).

$$G_{12S} = \frac{\tau_{12}}{\gamma_{12}} \tag{4.4}$$

From the concentric cylinder model (CCM) equations [36], the matrix secant shear modulus G_{ms} can be solved in (4.5) by extending the equation to the non-linear regime.

$$G_{12s} = G_{ms}\left(\frac{G_{12}^{f}(1+V_f)+G_{ms}(1-V_f)}{G_{12}^{f}(1-V_f)+G_{ms}(1+V_f)}\right) \tag{4.5}$$

In using this equation, the fiber shear modulus $G_{12}^{f} = 24\ GPa$ is assumed to be held constant and equal to that as provided by the manufacturer [37] and bias tow volume fraction $V_f = 0.56$ as determined from previous investigations of the TBC 45 material [20]. If an assumption is made that the fiber and matrix experience the same shear stress, τ_{12}^{f} and τ_{12}^{m} respectively, as stated in (4.6), then the matrix shear strain γ_m can be determined by (4.7).

$$\tau_{12} = \tau_{12}^{f} = \tau_{12}^{m} \tag{4.6}$$

$$\gamma_m = \frac{\tau_{12}^{m}}{G_{ms}} \tag{4.7}$$

Figure 4.14 shows the matrix secant shear modulus G_{ms} plotted against shear stress for each of the five coupons. Note that the initial wide range in values is due to subtraction of extremely small strain values and are typically ignored until such initial noise has settled out of the analysis.

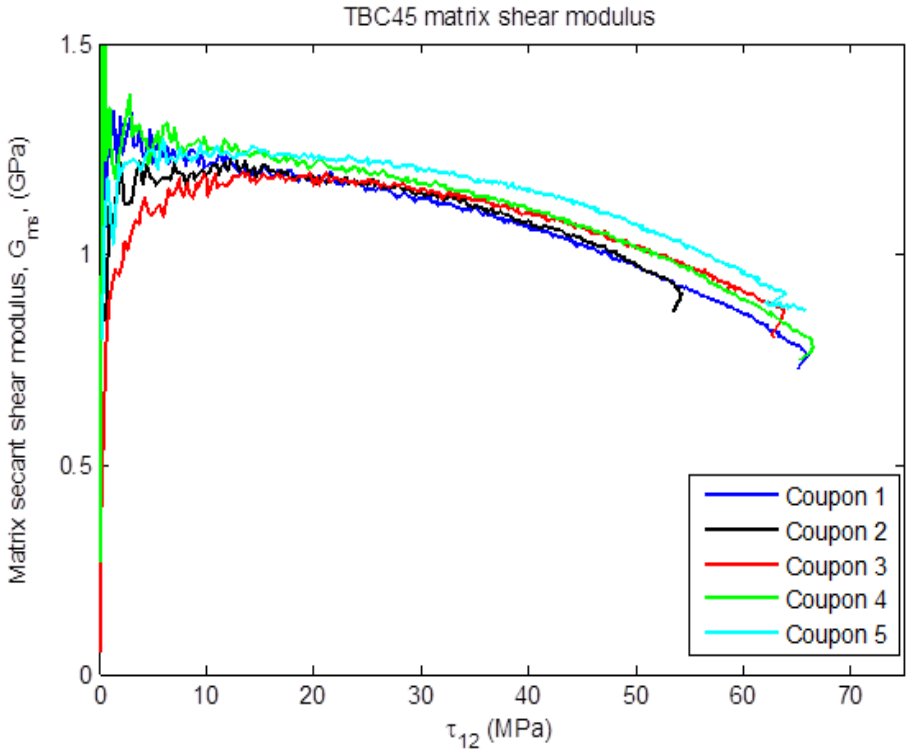

Figure 4.14: Matrix secant shear modulus as determined from solving (4.5)

With the fully non-linear matrix shear stress and shear strain data determined, Figure 4.15 shows the non-linear stress-strain curves for the five coupon tests. Note the dashed line in Figure 4.15 is used as a reference line in Figure 4.16 for comparative purposes. A Ramberg-Osgood fit was selected for the matrix shear stress-strain curves because of the simple yet accurate breakdown of the linear and non-linear contributions. Also note that in Figure 4.16, Ramberg-Osgood curves have been extended by approximately 80% of the test data to highlight the strong non-linear relationship.

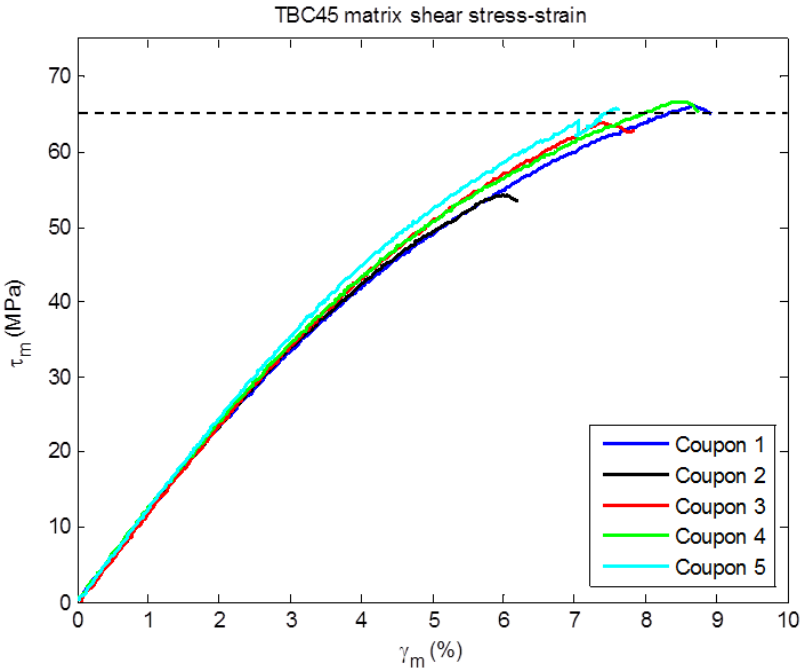

Figure 4.15: In-situ non-linear matrix shear stress-strain curves

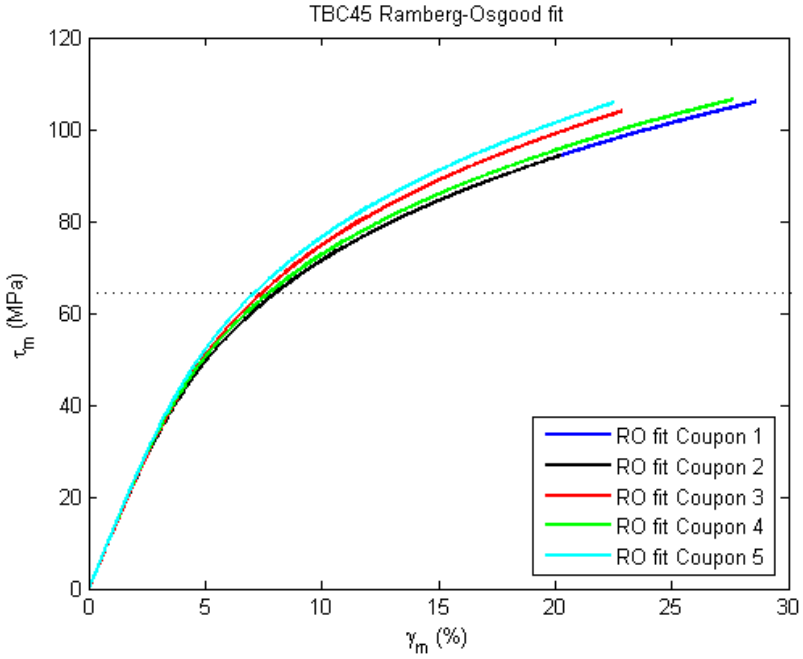

Figure 4.16: Ramberg-Osgood fit curves for in-situ matrix experimental data as determined from Figure 4.15

The form of the Ramberg-Osgood curve is given by equation (4.8) where α, τ_o, and n are parameters used to determine the best fit.

$$\gamma = \frac{\tau}{G} + \alpha \frac{\tau}{G}\left(\frac{\tau}{\tau_o}\right)^{n-1} \tag{4.8}$$

The first term in (4.8) is familiar from simple linear elastic behavior, but the second term introduces a non-linear contribution to the shear strain. Using J2 deformation theory of plasticity [38], the in-situ matrix equivalent stress and equivalent plastic strain can be calculated using equations (4.9).

$$\begin{aligned} \sigma_{eq} &= \sqrt{3}\tau_{12}^{m} \\ \varepsilon_{eq}^{p} &= \frac{\gamma_m^p}{\sqrt{3}} \end{aligned} \tag{4.9}$$

Figure 4.17 shows the in-situ equivalent stress, equivalent plastic strain relationship for each test. The in-situ equivalent plastic behavior will prove vital in the modeling efforts discussed in section 5.4 as the linear elastic material properties are not sufficient at capturing the desired axial tow buckling behavior.

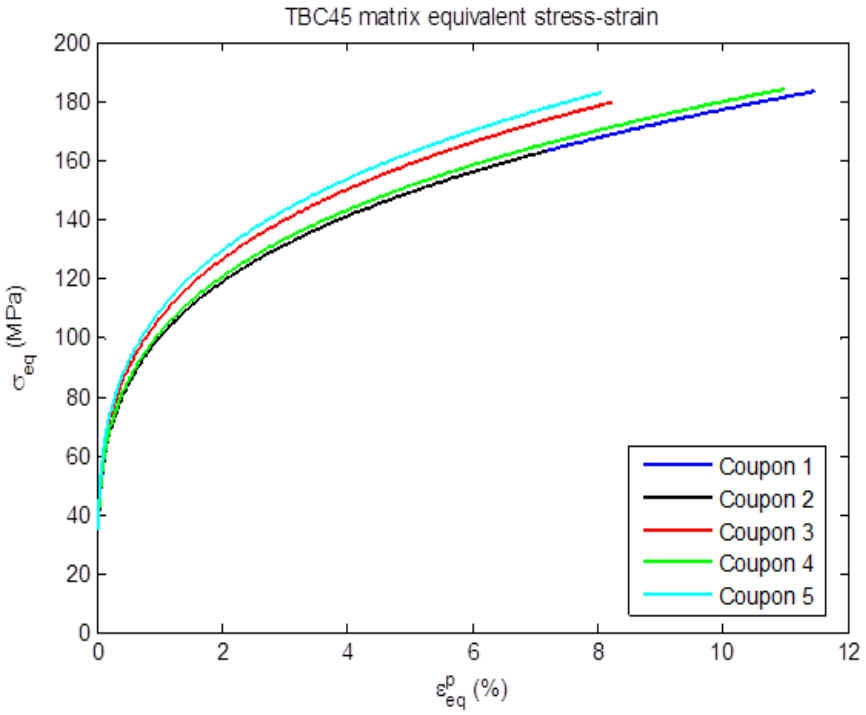

Figure 4.17: In-situ matrix equivalent stress vs. equivalent plastic strain

4.4 Postbuckling of Unitized Stiffened Textile Panels

Stiffener separation is a challenging problem faced by composite and metallic stiffened structures alike. Delamination of adhesively bonded stiffeners is a common failure mode under compression. The effect of defects is also a concern throughout stiffened structures [39] as manufacturing and service life defects are more difficult to design and analyze. Impact of a stiffened structure can cause barely visible impact damage (BVID) that is difficult to predict yet significant enough to cause a reduction in load carrying capability. Involved manufacturing techniques have even been introduced such as stitching the stiffeners to the shell preform to impair separation growth [40]. Such methods increase part and analysis complexity despite showing encouraging results from a performance perspective. The unitized stiffened composite textile panels used for this work aim to demonstrate successful removal of stiffener separation as a failure mode under axial compression and well into the postbuckling loading regime. While achieving this, the modeling complexity is aimed to remain similar to a model that incorporates global failure modes along with material failure modes.

The following sections provide an overview of the experimental unitized stiffened composite textile prototype panels. The test setup is discussed, along with the goals of a successful test. Experimental instrumentation and data collection systems are discussed. The results for all four TBC 30 panels and TBC 60 panels are presented in the form of load-displacement data, DIC images of certain behavior, and strain gage information that provides clarification on a mode-switching event observed in the TBC 60 panel tests.

4.4.1 Test Overview

Each test was conducted on a two-post compression 120-kip load frame at NASA Langley Research Center within the Structural Mechanics and Concept Branch. Recorded data include test-frame load and displacement, external instrumentation displacements, optical images for DIC, standard video with audio, high-speed video, and external strain gages bonded in back-to-back pairs. Specimens were loaded in axial compression. The load frame has one platen that is adjustable in rotation about the center point. This feature is to aid in achieving even loading due to specimen boundary condition imperfections should the specimen end not be parallel to the lower platen surface. One row of strain gages, discusses later, was used to balance the load introduction to each specimen. To achieve this, each specimen was put under a small compressive load of 2500 N and the cross-head adjusted so that similar strain readings were achieved. While this procedure does not remove all boundary condition imperfection effects, it does aid in removing erroneous loading conditions such as bending moments into the panel as those are not within the scope of the test. Successful tests were qualified as tests achieving failure, full data capture throughout loading, and informative progression through the prebuckling, buckling, and postbuckling stages. Satisfactory failure modes include all failure modes of the stiffened panel structure itself between the potted ends. Failure modes resulting from changing boundary conditions, effects of the potted ends, or failure within the potted sections were deemed unacceptable failure modes as they typically quantify the limits of the test setup rather than the test article itself.

4.4.2 Instrumentation

Various instrumentation were used to record information during the loading portion of the test. Each test had the same instrumentation so that data recorded across tests would be consistent. The following section provides an overview of the various instrumentation used to collect and process data during loading.

A total of 20 strain gages per panel were attached at various locations prior to the test. The 20 gages were divided into two rows of 10 gages per row. The first row is located 25.4-mm (1-inch) from the top surface of the bottom potting block. These gages were used during the specimen placement within the load frame to balance and level the crosshead. The second row of strain gages were placed along the center of the panel. Initial computational buckled mode shapes show that one half wave is associated with the lowest buckling mode. These results are further discussed in section 5.2. As the largest bending strains of one half wave mode shapes occur in the center of the wave, the second row of strain gages were bonded at these expected locations. Figure 4.18 provides an overview of the relative locations of each row of strain gages on each panel.

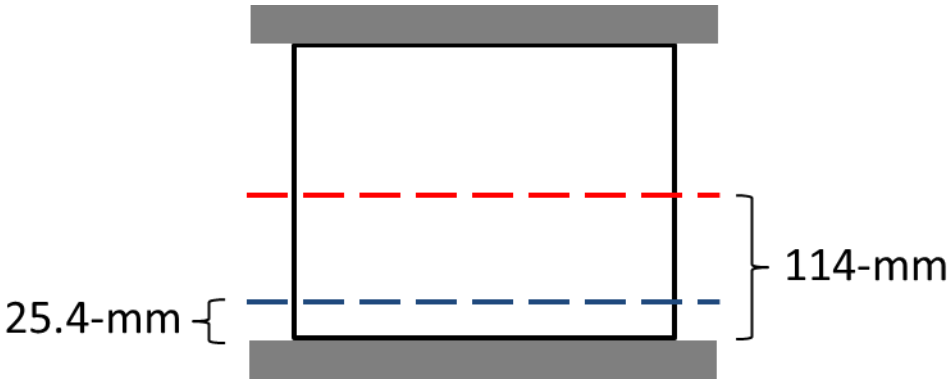

Figure 4.18: Diagram showing the two locations of rows of strain gages bonded to each panel

As the structure is a thin-shell, strain gages were attached in a back-to-back configuration where a strain gage on the stiffened side would have a corresponding strain gage in the same location on the skin side of the shell. Figure 4.19 provides a top-down view looking along the stiffener direction for each pair of strain gages. Both rows of gages are labeled by number and according to the row by color. Red numbers, or gages

11-20, correspond to the red row in Figure 4.18, and blue numbers, or gages 1-10, correspond to the gage numbers in the blue row in Figure 4.18. There are three pairs of gages in each row, one for each skin section, and two pairs of gages in each row, one for each stiffener section. The location of strain gage pairs are to be near the center of each half wave mode shape. The center of the *center skin section* is then 129-mm from the edge of the *narrow skin section*. The gage pairs on the stiffeners are placed to be in the middle of the stiffener width. The gage pairs on the *narrow* and *wide skin sections* are placed away from the edge by 25.4-mm so as to reduce possible edge effects. While bending strains are not as sensitive to edge effects, the compressive strains are more sensitive as a result of the effective-width phenomenon in postbuckled shell structures.

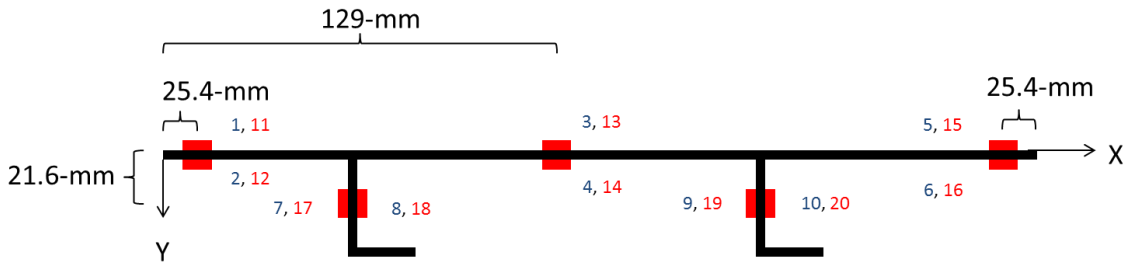

Figure 4.19: Strain gage numbering and pairing diagram

Pertinent strain gage information is provided in Table 4.2. Gages were sourced from Vishay Micro-Measurements and were bonded to the stiffened panels using Vishay's recommended adhesives and procedures. The leads from the strain gages were connected to an external data acquisition system to record the signals during testing. The information provided in Table 4.2 was used within the data acquisition system to convert the voltages into strains directly.

Table 4.2: Strain gage parameters used on each stiffened panel test

Gage Type	Grid Resistance (Ohms)	Gage Factor	Transverse Sensitivity (%)	TC of Gage Factor (%/100°C)
C2A-13-250LW-350	350.0 ±0.6%	2.120 ±0.5%	+0.5 ±0.2%	+1.3 ±0.2

Black and white speckle patterns were painted on the panels after attaching the gages. Fully 3D DIC systems were used on both sides of each panel to record in-plane and out-of-plane panel deformations. On the stiffened side of the panel, two static cameras were oriented and calibrated such that displacements towards or away from the cameras could be quantified. The unstiffened side of the panel had a second pair of DIC cameras positioned so the same method would record the back skin surface of the panel during loading. Each pair of cameras was calibrated prior to conducting each test. Figure 4.20 shows the DIC camera setup on the skin side of the test setup.

In addition to the DIC cameras, high-speed video was recorded on both sides of each panel. Regular video with audio was included as a precautionary measure in case an unforeseen event occurred that would have been missed by the photo or high speed cameras. The high-speed cameras were intended to assist identification of the location of failure initiation in the event of a sudden load drop or loss of load carrying capability. However, the size of the recorded area and corresponding maximum frame rate made any clear initiation point difficult to determine for most of the tests as the failure crack propagated too quickly across the width of the specimen. Figure 4.21 shows the 3D DIC, high speed video, and regular video cameras recorded on the stiffened side.

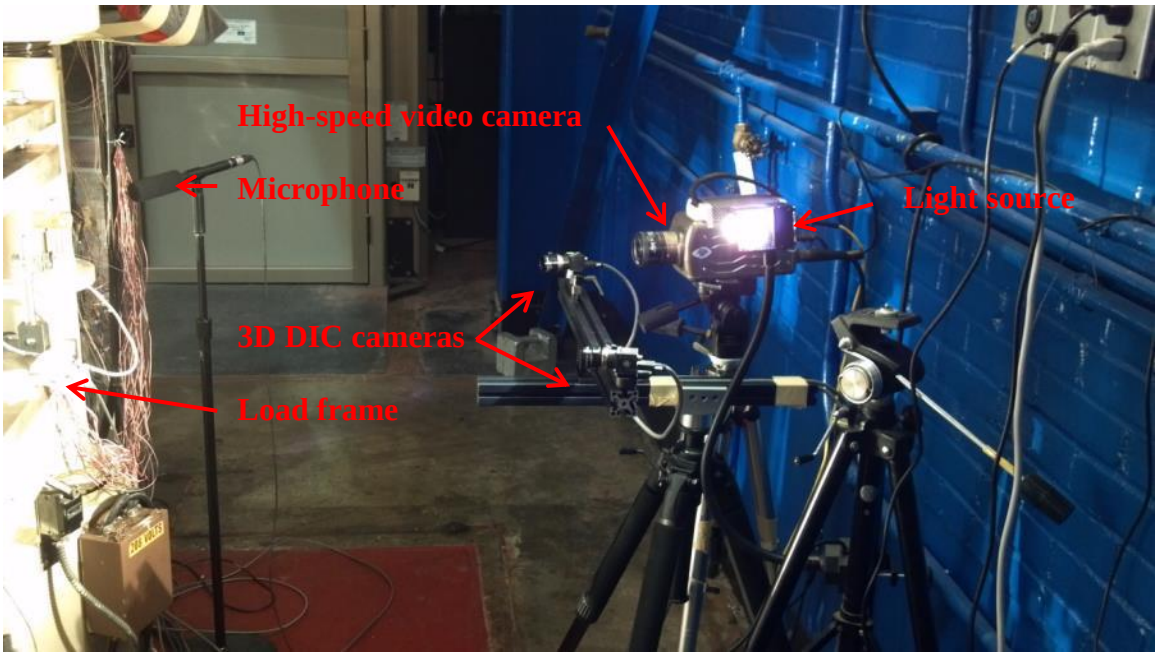

Figure 4.20: 3D DIC and high speed camera setup on the skin side

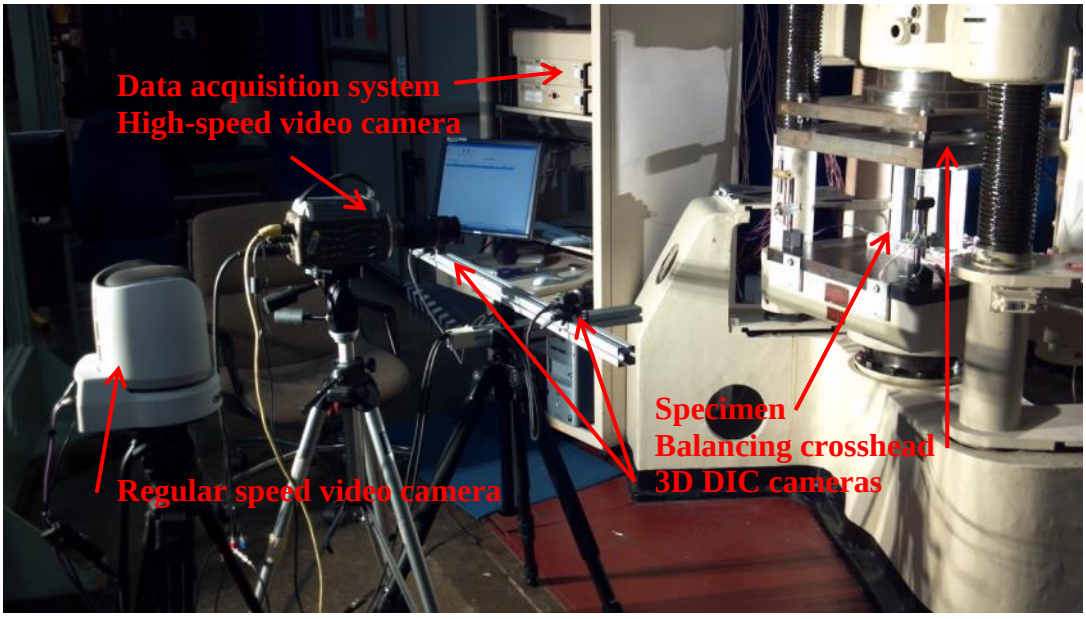

Figure 4.21: 3D DIC, high speed camera, and standard video setup on the stiffened side

Four LVDTs were used to measure the relative displacements between the upper and lower platens in the test frame. One LVDT was placed in each corner of the platens. Multiple LVDTs can be analyzed to determine relative platen rotation in addition to axial

displacement. Relative platen rotation is a common occurrence in two-post test-frames because of compliance within the load frame. It is important to minimize introducing bending moments or other loading conditions beyond simple axial loading in this test.

The locations of the LVDTs are provided in Figure 4.22 relative to the stiffened panel specimens. Note that the view is a top-down view looking along the stiffener direction. It should also be noted that for two of the TBC 30 panels tests, the locations of the LVDTs were moved closer to the specimen because erroneous relative displacements were being recorded that could not be accounted for at the time of testing. Displacement data from DIC was used to supplement and correct the shifted LVDT data for those tests that were affected. The corrected data is believed to be accurate and representative of the behavior of each affected specimen. Also seen in Figure 4.22 is the slight offset of the specimen skin section relative to the centerline of the platen. This offset was calculated to ensure minimal bending loads would be introduced during axial compression.

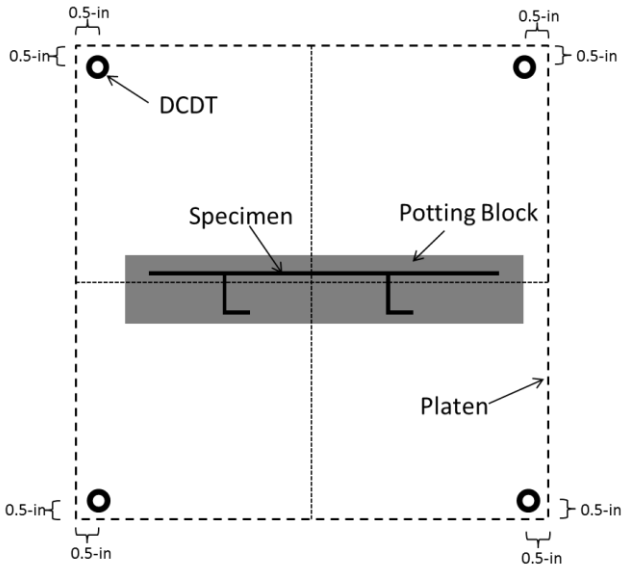

Figure 4.22: LVDT (or DCDT) recording location relative to platen and specimen

4.4.3 TBC 30 Test Results

Four TBC 30 stiffened panel specimens were loaded well into postbuckling until failure. All four stiffened panels failed acceptably and within the gage section of each specimen. A macro crack was clearly visible traversing the width of each panel, and a

significant load drop was observed. Although residual loads were still carried by all panels, the load drop was significant compared to the previously sustained load so as to classify failure as a complete loss in load carrying capability. Figure 4.23 provides the load-displacement curves for all four TBC 30 panels. There is excellent consistency in the prebuckling loading range, but postbuckling load-displacement slopes vary slightly over all four panels. The final failure load shows remarkable consistency in load and displacement values, especially for a compression test. TBC 30 P3 failed at the lowest load at 204,800 N, and TBC 30 P1 failed at the highest load at 212,400 N. This is a range of only 3.7% for load variance. TBC 30 P2 failed with the least end displacement of 1.111-mm, and TBC P4 failed with the most end displacement at 1.179-mm. This is a range of 6.1% of the overall displacements observed. The initial buckling loads, as given in Table 4.3, are more varied than the failure loads on a percentage basis. Possible reasons for the varied buckling load of the TBC 30 panels include misalignment within the potting blocks, misalignment in the test frame, or imperfections in P2 and P4 that are not present in P1 or P3.

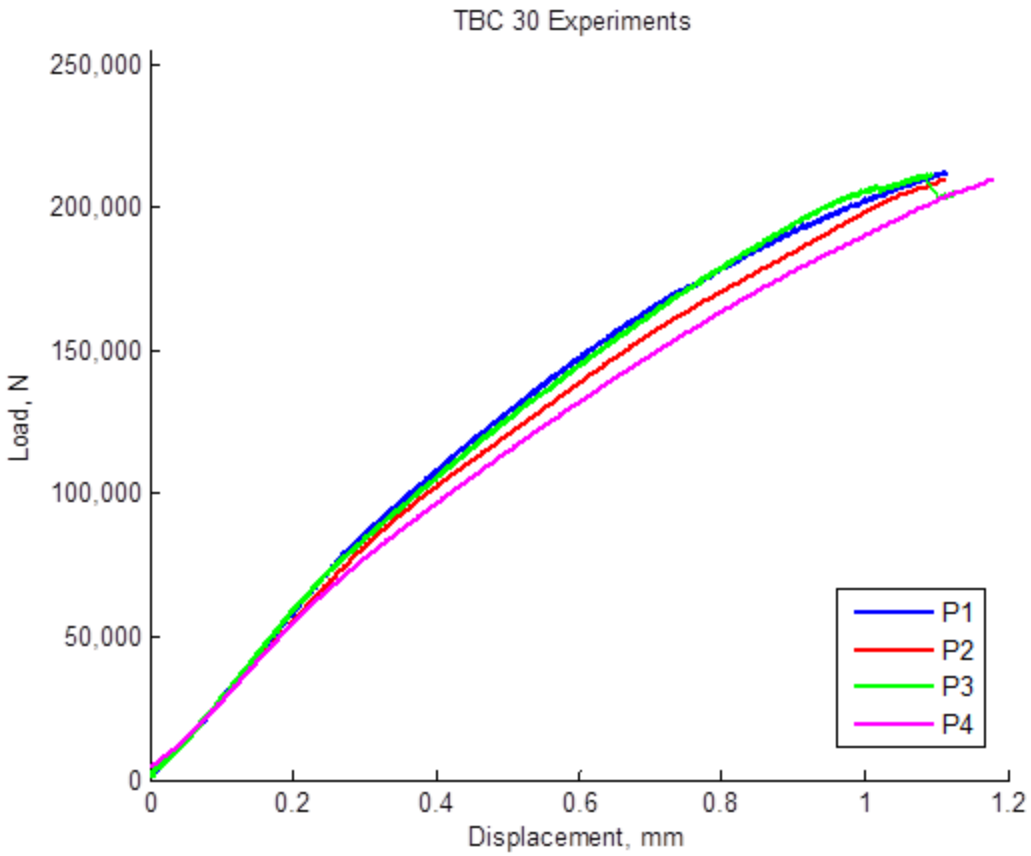

Figure 4.23: TBC 30 postbuckling load-displacement curves

Table 4.3: Experimental buckling loads for TBC 30 panels

	TBC 30 Buckling Load (N)
P1	51,780
P2	50,310
P3	51,940
P4	49,410

In addition to the load-displacement data, plots of each panel's strain gage data is given in Figure 4.24. The gage pairs plotted are from Row 2 on the skin section only i.e. gages 11-16. While the stiffeners do show slight buckling behavior, the strain divergence of the back-to-back pairs is much more apparent on the skin gages.

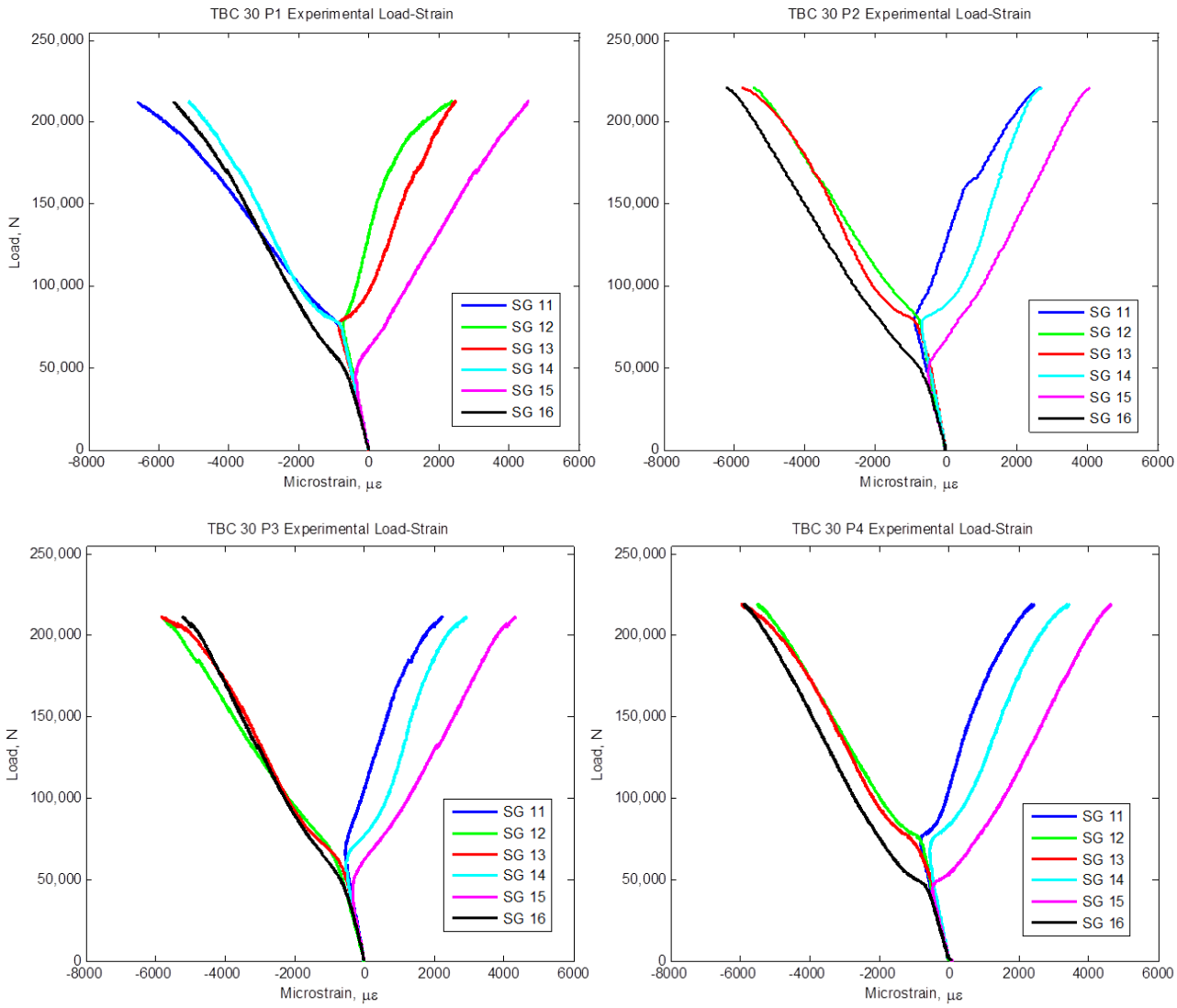

Figure 4.24: Load vs. center line skin section strain data for TBC 30 experimental panels

From the load-strain plots, the initial buckle in the *wide skin section* is visible in strain gage pair 15/16 near 50 kN. The *narrow skin section* and *center skin section* continue loading in a linear fashion until approximately 70-80 kN at which load both the sections diverge due to buckling. The strains at which failure occurs is moderately consistent in all four panels. The negative strains reach near -6000 microstrain at failure, while the positive strains vary between 2000 and 4000 microstrain depending on the skin section. The *wide skin section* fails near positive 4000 microstrain, and the *narrow* and *center skin sections* fail near positive 2000 microstrain As the buckled shape is under

bending conditions, there is a tensile and compressive side associated with each buckled half wave as the loading increases.

The skin section recorded by strain gages 15 and 16 clearly diverge before the other two skin sections. This is due to the *wide skin section* being wider than the *narrow skin section* as well as having an unsupported free edge as compared to the *center skin section*. Figure 4.25 shows a load-displacement plot with all four load-experimental curves overlaid by callouts of TBC 30 P4. Each callout shows 3D DIC out-of-plane displacement contours where red is toward the camera and purple is away from the camera. Similar buckling mode shapes were observed for all four TBC 30 panels with one half-wave across the length and width of the skin sections. The *narrow* and *wide skin sections* buckle away from the camera while the *center skin section* buckles toward the camera. The maximum out-of-plane displacement (towards the camera) averaged around 8-mm near the center of the *center skin section* while the minimum (away from the camera) averaged around 11-mm in the center of the unsupported free edge in the *wide*

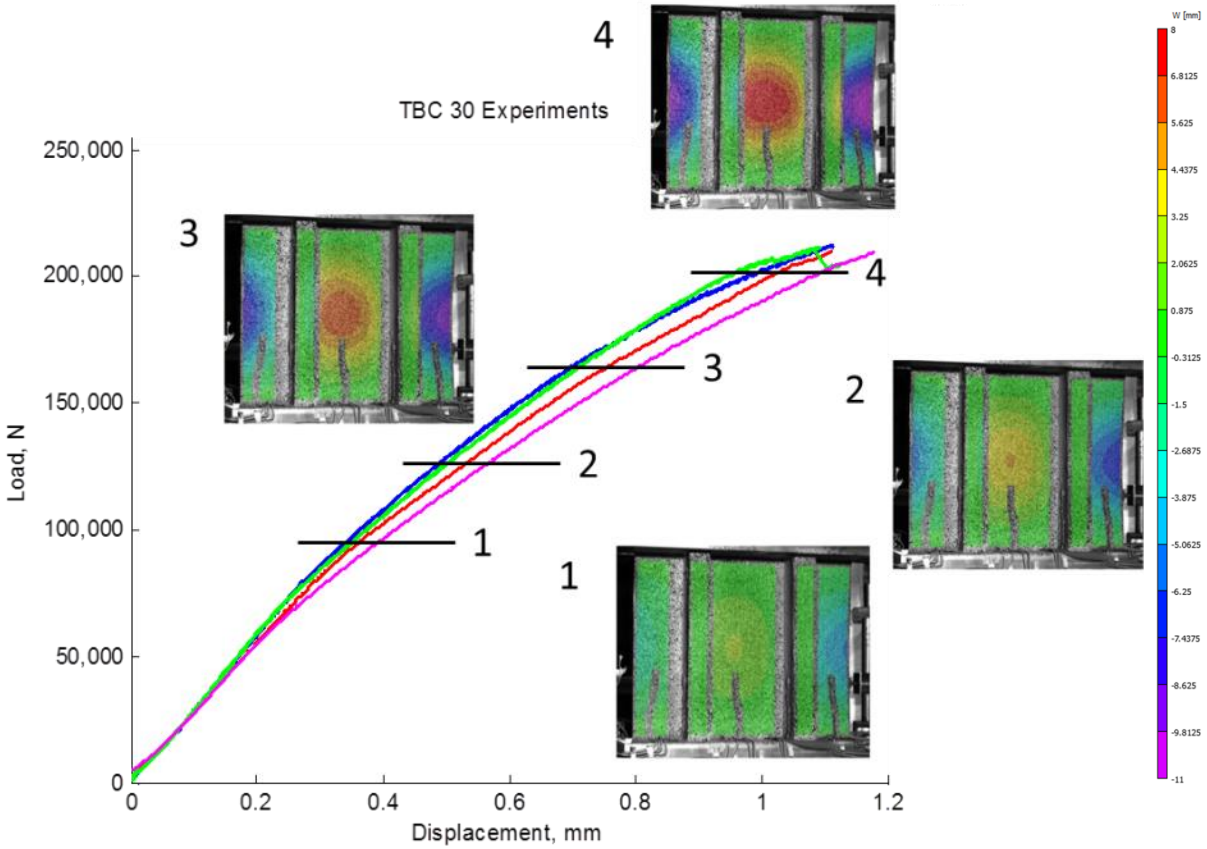

Figure 4.25: 3D DIC out-of-plane displacement contours in loading progression

skin section. Callout one shows the out-of-plane (w) displacement initially after all skin sections buckle. Note that the largest w displacement relative to the panel is in the *wide skin section*. Callouts two and three show increasing displacement contours as loading progresses well into postbuckling. Callout four shows the contour prior to global failure and demonstrate the extent of the postbuckling w displacements. Also visible in callout four are the buckling of the flange sections. The *narrow flange section* buckles toward the skin of the panel while the *wide flange section* buckles away from the skin.

4.4.4 TBC 60 Test Results

Four TBC 60 stiffened panel specimens were loaded well into postbuckling until failure. All four stiffened panels failed acceptably and within the gage section of each specimen. A macro crack was typically visible across the length of each specimen, though at certain points the exact crack location was difficult to determine. All panels lost effectively all load carrying capability due to the magnitude of the load drop at the failure event. Figure 4.26 shows the load-displacement data for each TBC 60 panel. There is again excellent consistency in the failure loads and displacements across all panels, but there are differences in the postbuckled stiffnesses. TBC 60 P1 failed at the highest load and largest end displacement at 144,300 N and 1.692-mm, respectively. TBC 60 P3 failed at the lowest load of 137,600 N, while TBC 60 P2 failed at the shortest end displacement of 1.624-mm. The failure load then spans a range of 4.9% and the end shortening spans 4.2% of the observed values. Table 4.4 provides the initial experimental buckling loads. TBC 60 P1 buckles at the highest load of 29,200 N, and TBC 60 P3 buckles at the lowest load of 22,830 N. There are two clear groups with P1 and P2 buckling near 29,000 N and P3 and P4 buckling near 23,000 N on average. There is more scatter in the TBC 60 buckling load than in the TBC 30 panels, however the smaller buckling load in P3 and P4 correspond to lower postbuckled stiffnesses as well. Such differences may be due to specimen misalignment in the potting blocks, in the test frame, or in imperfections in the panel itself. As discussed in section 3.3 with the averaged section thicknesses, TBC 60 P4 was significantly thinner in the skin sections. While P3 was not as thin as P4, other

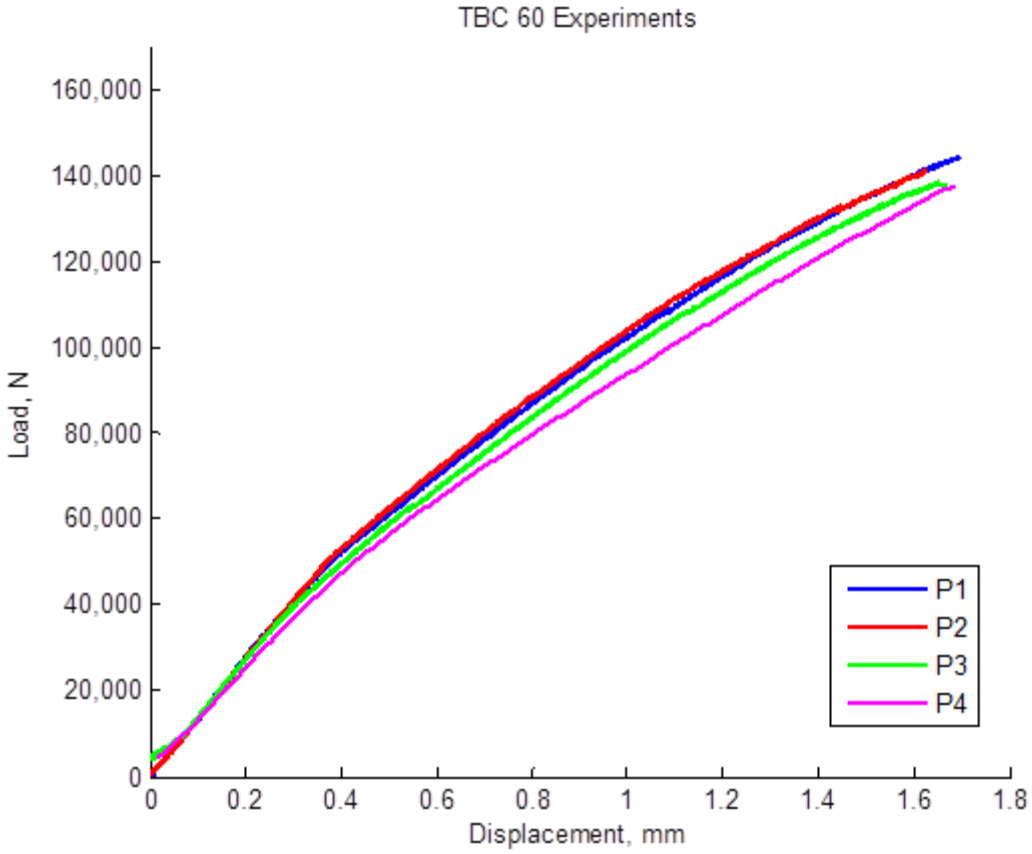

Figure 4.26: TBC 60 postbuckling load-displacement curves

specimen defects or misalignment could have contributed to the reduced buckling load as compared to P1 and P2.

Table 4.4: Experimental buckling loads for TBC 60 panels

	TBC 60 Buckling Load (N)
P1	29,200
P2	28,670
P3	22,830
P4	23,530

As with the TBC 30 panels, strain gage data are provided for Row 2 with the skin section gages only. There is significantly different behavior in postbuckling loading compared to the TBC 30 panels. Figure 4.27 shows the load-strain curves for the TBC 60 panels. As observed in the TBC 30 tests, the wide section strain gages diverge before the narrow and center section pairs. However, there is a secondary and a tertiary event after

the initial buckling strain divergence in the TBC 60 experiments [41]–[49]. Stein in [44] analyzed a three-element column on a nonlinear spring foundation to study mode switch phenomenon. While simple in form, the concepts are applicable to plate and shell structures. Discussed in [43], Nakamura investigated simply supported flat rectangular plates and how modal coupling effects may result in mode shapes with more than half waves in the loading direction. Supple in [47] investigated the effects of boundary conditions on uncoupled and coupled sudden buckling mode changes in thin rectangular plates in compression. Secondary buckling may be considered a result of the redistribution of energy into a lower equilibrium state. Typically, just before the panel is loaded halfway to the failure point, the strain divergence shifts in the TBC 60 panels and the gage pair readings get closer together in value. Gage pairs 15/16 always had this behavior as the *wide skin section* was the last section to transition into the two half wave mode shape. Panels P2 and P4 experienced the mode switch in the *wide skin section* near 90,000 and 80,000 N, respectively. Panels P1 and P3, however, had a mode switch at a much lower load near 60,000 N. This difference in mode switch load for the *wide skin section* is related to the mode switch behavior of the rest of the panel. Panel P4 had the *narrow* and *center skin sections* switch to the two half wave mode just under 60,000 N and is in line with the values from P1 and P3. This is because panels P1 and P3, based on the load-strain data, experienced the mode switch for all skin sections at approximately the same time. In this aspect, panels P1, P3, and P4 experienced similar *initial* mode switch events. This behavior is further explained when looking at Figure 4.28 and the associated callouts during the loading process [50]. The callouts are out-of-plane displacement color contours for panel TBC 60 P4. A postbuckling mode switch occurs for each of the TBC 60 panels. The first observed mode after buckling is the single half-wave also observed in the TBC 30 tests. Part way during the test, however, the mode switches to a double half-wave in the stiffener direction. The narrow and center skin sections enter this secondary mode prior to the wide section at callout two, but the wide section does switch before final failure so the entire panel develops a full double half-wave mode in callouts 3 and 4. This behavior is discussed more in modeling section 5.2. The maximum out-of-plane displacement (i.e. closer to the viewer) averaged around 6.5-mm while the minimum (i.e. farther from the viewer) averaged around 6.7-mm.

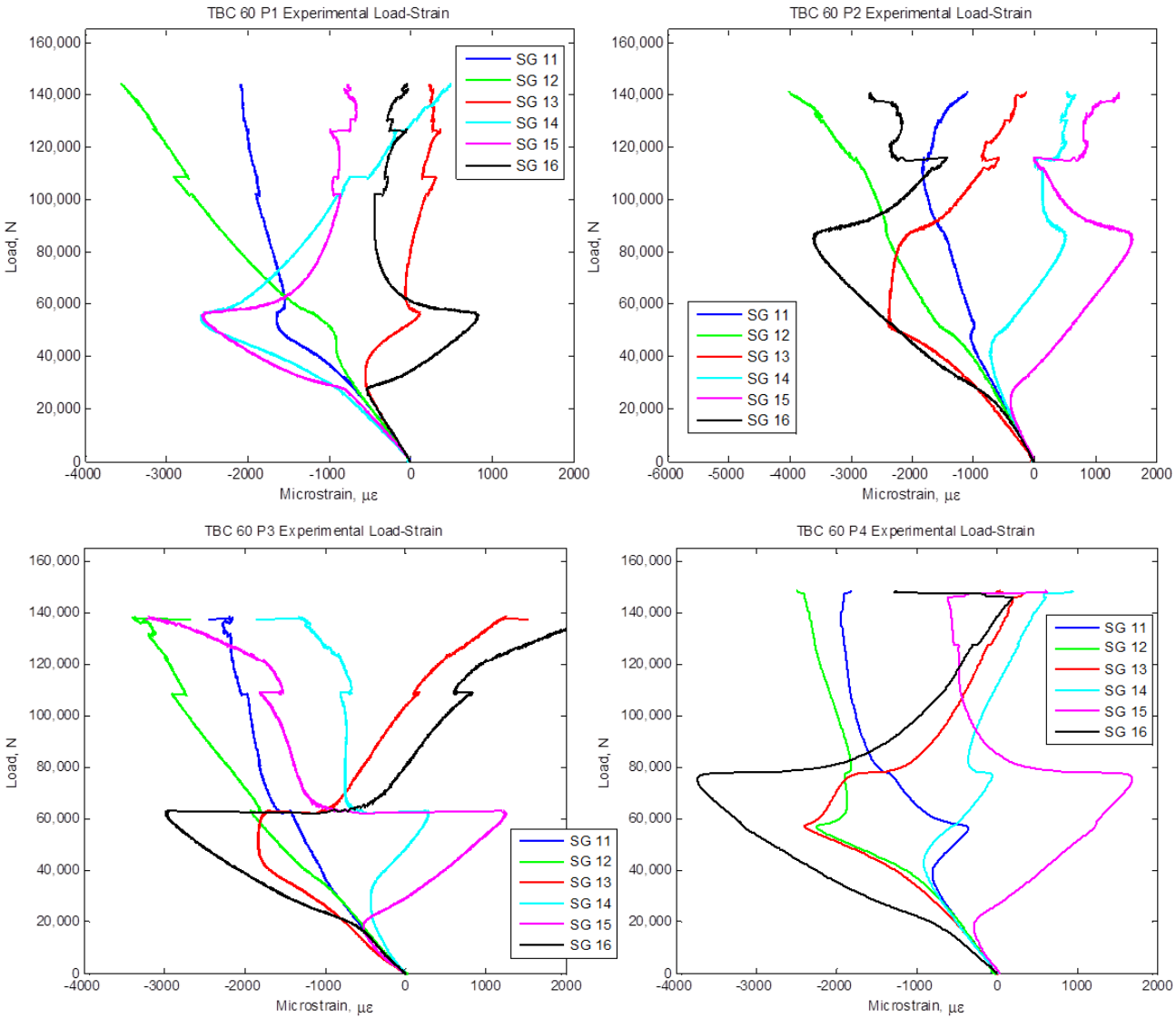

Figure 4.27: Load vs. center line skin section strain data for TBC 60 experimental panels

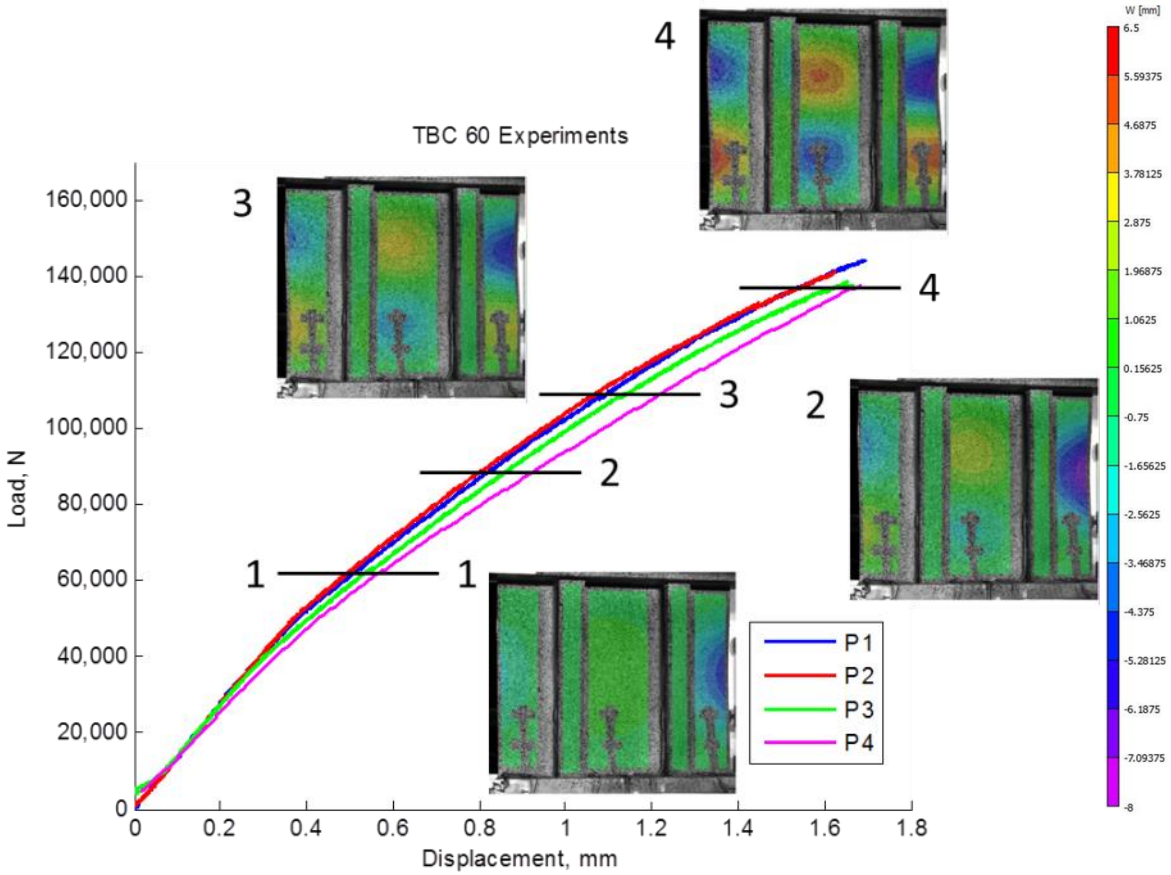

Figure 4.28: 3D DIC out-of-plane displacement contours in loading progression

4.5 Failure Investigation

After all TBC 30 and TBC 60 tests were conducted, an investigation was performed to determine the final failure mode of both types of panels. Visual inspection of the local crack behavior and path was recorded as reference. Figure 4.29 shows the macro crack path for TBC 60 P1. Note that the crack path, visible as the dark band running across the specimen, is located well away from the potted ends. The right image is an edge-on view of the same panel corresponding to the narrow section edge as marked by the eye symbol. The blue and white segments at the top of the edge-on view represent the scale as each small segment is 0.25-inch per side.

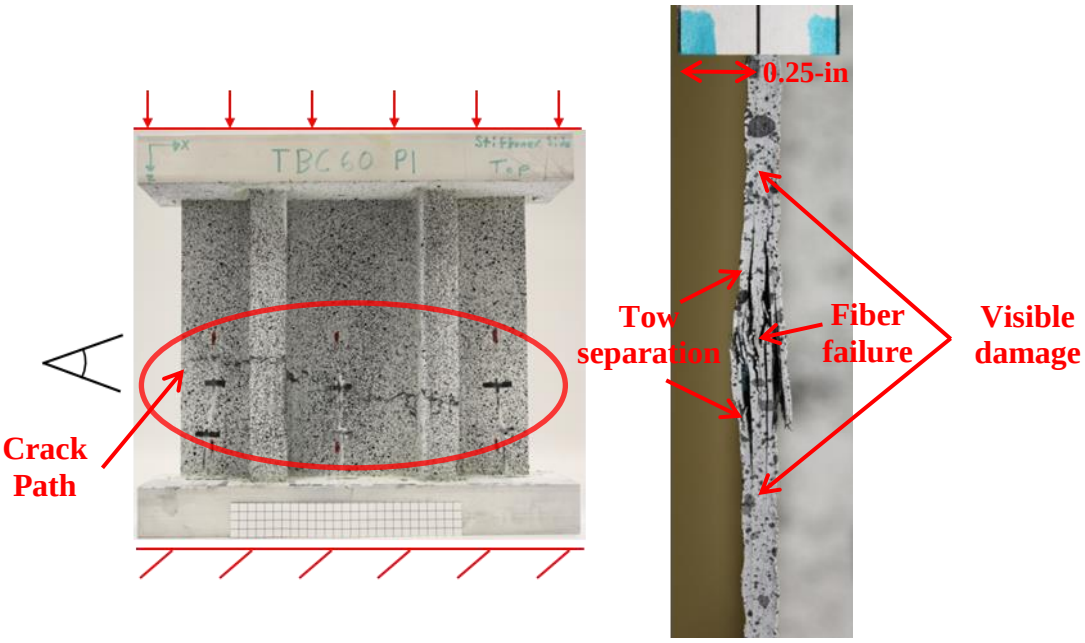

Figure 4.29: Failed TBC 60 P1 specimen showing crack path (left) and edge-on view (right)

The edge-on view in Figure 4.29 highlights a couple key failure characteristics about the TBC 60 panels. First is the crack and associated visible damage is localized compared to the overall length of the specimen. Using the scales as reference, the overall crack height is approximately 1-inch. This indicates that distributed failure did not occur at the edges. Second is the "broomed" effect that failure caused. This is a fairly common failure mode for composites in compression, particularly with textile composites [8], [15], [32], [51]–[55]. Caner in [51], among others, investigated a semi-multiscale approach to modeling failure in braided composites by capturing inelastic behavior on so-called microplanes based on the mesoscale structure of the material. This model was used to effectively capture the response of axial crushing in a composite tube. The broomed segments are localized delaminations where fiber tows have separated either within a textile layer or across textile layers. In the middle of the crack is a region of highly damaged composite. This area is significant due to the presence of localized fiber breakage. Significant portions of fibers outside this approximately 0.125-inch region were not found to be broken.

Further failure investigations revealed that localized crack distributions depended heavily on the underlying TBC material. For example, small local cracks in the TBC 30

panels around the macro crack were different than the small local cracks in the TBC 60 panels around the macro crack. This difference is shown in Figure 4.30 and Figure 4.31.

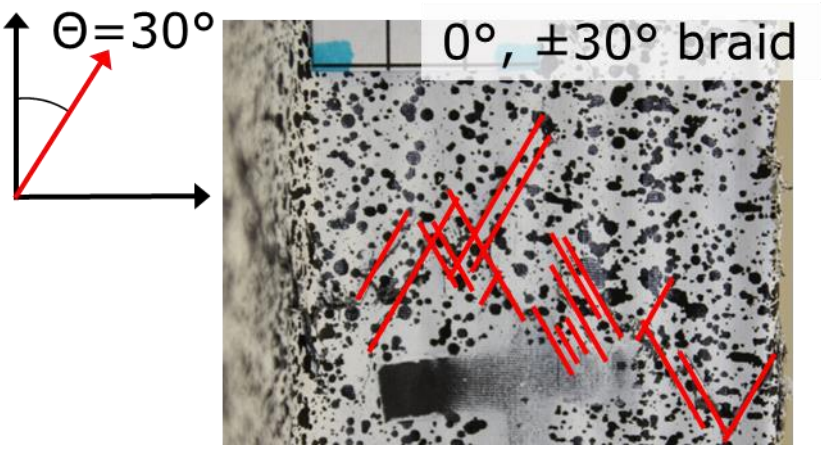

Figure 4.30: TBC 30 panel localized cracks highlighted in red on a stiffener section

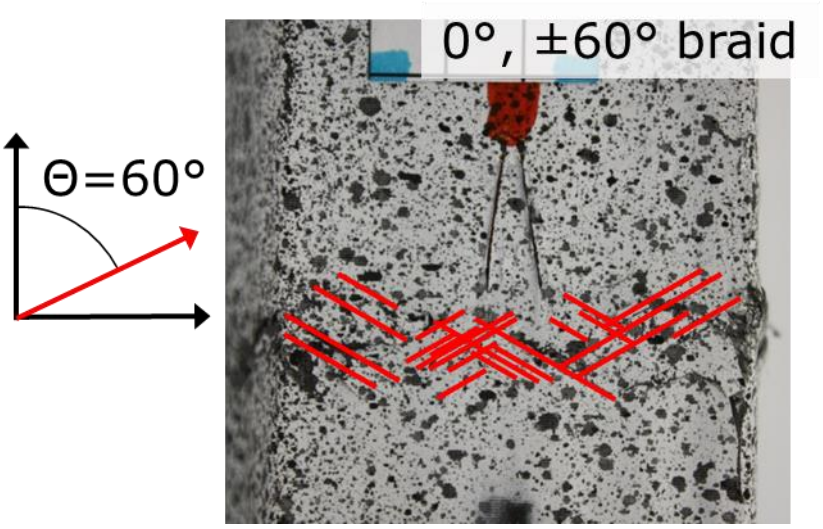

Figure 4.31: TBC 60 panel localized cracks highlighted in red on a stiffener section

The orientations of local damage cracks are aligned well with the local underlying bias tow braid angle for the TBC material. The TBC panel in Figure 4.30 has many local cracks aligned near the 30° braid angle, which is depicted by the set of axes to the left of the image. In a similar manner, the TBC panel in Figure 4.31 has many cracks aligned

close to the 60° braid angle, again depicted by the axes on the left of the image. The presence of such architecture-based damage suggests that a homogenized material description may not be sufficient to accurately capture crack initiation or propagation for braided materials[4], [56], [57]. These observations significantly influenced the modeling efforts and resulted in the formation of a multiscale analysis framework in which to incorporate local architecture dependent behavior into a homogenized global stiffened panel model. This framework is discussed in section 5.3.

To determine the extent of delamination within the panel material as well as to qualify the extent of damage near where stiffeners integrate to the skin, stiffened panels from both material types were examined using ultrasonic inspection techniques. The unstiffened sides of TBC 30 P1 and TBC 60 P1 panels were inspected using an ultrasonic probe submersed in a water bath. Ultrasonic inspection data is often difficult to interpret depending on the experience of the inspector with the component material. The basis for the technique is similar to that in medical ultrasounds. Sound waves are transmitted into a specimen. If the specimen is intact and homogenized, the opposite surface would return the only primary reflection with which to analyze. In a failed composite, particularly nonhomogeneous composites like braided textiles, there are many changes in density. Each change in density causes many reflected waves to be picked up by the instrument and from there can be used to create an image. Cracks, both opened and closed, have surfaces. The surfaces result in a change in density from one area to another and show up as a shadow or blurred area in the processed image. The primary data result for the TBC 30 P1 panel ultrasonic inspection is given in Figure 4.32. The triaxial braid architecture of the panel is clearly visible in the ultrasonic image. The locations of the stiffeners are also clearly observed as the vertical dark lines. Note that the observed pattern from the scan does not necessarily indicate failure everywhere in the panel. Instead, the undulating braided tows cause the architecture to be detected by the UT scanner. Areas of damage or failure are indicated in the red shaded regions. For this composite material, damaged and failed areas are typically noted by a lack of a clear, sharp image. The global crack path returns a blurred area in which the TBC architecture is more difficult to view. Other cracks were present in the TBC 30 panel, however they could not be visually rendered using the described ultrasonic techniques.

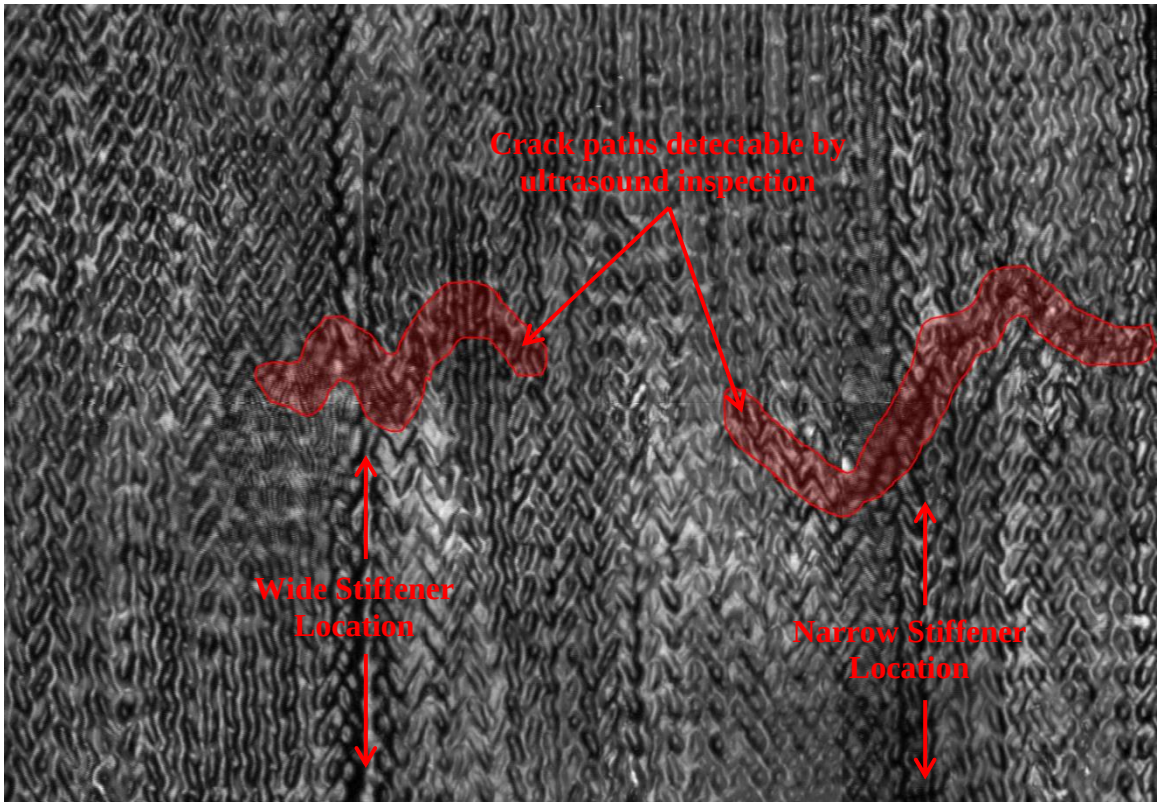

Figure 4.32: TBC 30 failed panel P1 UT scan processed image

The primary result for the scanned TBC 60 P1 failed panel is shown in Figure 4.33. Again, the braided architecture is clearly visible and markedly different compared to the TBC 30 material. The stiffener locations are still observed well, and the cracks are highlighted by the red shaded regions. Note that the crack paths are much straighter in the TBC 60 compared to the TBC 30. The crack path in the TBC 30 panel often altered direction near the presence of a stiffener. Despite best efforts, both TBC 30 and 60 materials are difficult to image well using ultrasonic techniques. The options available to UT methods were not exhausted, however the primary results indicate that alternative non-destructive evaluation (NDE) methods should be considered. False positives (and false negatives) are often a major technological challenge using NDE methods. An NDE technician without braided or other textile inspection experience might encounter significant difficulty applying UT techniques to this material, and further development is needed before high accuracy in correctly identifying damage and failure is achieved.

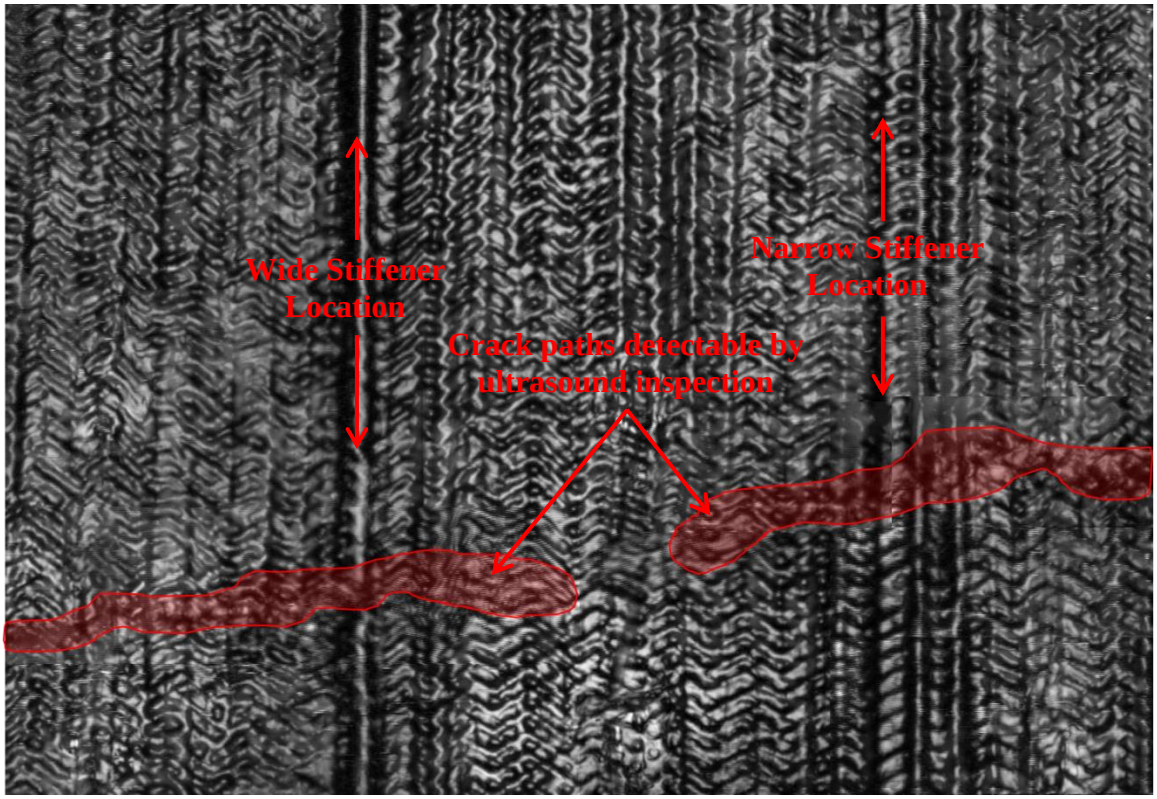

Figure 4.33: TBC 60 failed P1 UT scan processed image

4.6 Summary

Multiple experiments were conducted during this body of work. A non-standard in-plane shear modulus characterization test demonstrated that material orientation independence could be achieved and provides a value in range with other published results. This test was simple to set up, conduct, and analyze. The anticlastic plate bending test should be considered as a viable alternative to other widely accepted tests such as single- and double-rail shear when inherent material architecture makes the modulus determination dependent on specimen orientation.

A test designed to characterize the fully non-linear in-situ matrix was conducted on material made from TBC 45 architecture based textile. The special nature of the ±45° braid creates a case of shear stress within the fiber tows. A previously published method used to extend the concentric cylinder model equations into the non-linear material regime was applied in analyzing the data. The resulting equivalent stress, equivalent plastic strain formulation is critical in developing a mesoscale model that accurately and

consistently captures TBC material failure modes under compression. This modeling work is discussed and the non-linear matrix characterization data further processed in section 5.4.

Experimental tests on the unitized stiffened composite textile panels were conducted for both TBC 30 and 60 materials. These tests showed excellent consistency in failure load within each architecture type, and all tests were determined to be successful overall. Failure occurred in the gage section of the stiffened panels. The TBC 60 panels exhibited different postbuckling behavior compared to the TBC 30 panels with a mode switch during loading. One half wave, as observed throughout the TBC 30 tests, became two half-waves in the TBC 60 panels. The mode switch was not a sudden, snap buckling phenomenon as the switch happened over a time period of tens of seconds. The investigation of the TBC 30 and 60 compression tests determined that stiffener separation did not occur as a primary failure mode. The primary failure mode was determined to be local buckling of the fiber tows which lead to the observed brooming effects and fiber failure in compression.

CHAPTER 5

Computational Analysis and Modeling

5.1 Introduction

This chapter details the analysis and modeling techniques developed to computationally simulate axial compression of the unitized stiffened composite textile panels. A macroscale model is created based on the nominal manufacturing dimensions as previously given in section 2.3.4. This model forms the foundation upon which certain modeling methods like mode switching, multiscaling, and failure models are implemented. The full development of a multiscaling framework is discussed. In the multiscaling framework, information is passed between a macro and mesoscale model. The mesoscale model incorporates critical analysis details that would otherwise not be feasible on a macroscale model or not possible to capture with a homogenized material description. It was previously noted in section 4.5 that the underlying material of the stiffened panel demonstrated clear and visible effects on how damage and failure occurred during postbuckling. Since multiscaling strategies often become detailed and complex, an entire section is devoted to describing what information is communicated between the macro- and mesoscale models and how that information is used by the receiving model. A brief description of the scripts used to achieve this process is also provided. The development of the mesoscale model representative volume element (RVE) is discussed for both the TBC 30 and 60 materials. In this work, RVE is taken to

be the smallest representative model of the material that captures the correct physics of what is being modeled. This is in contrast to a representative unit cell (RUC) which is simply the smallest repeat unit to capture the correct geometry. The RVE and RUC may be the same in certain analyses such as stiffness determination, but may also be quite different once nonlinear effects, damage, and failure are aimed to be modeled correctly. An overview of the periodic boundary conditions used in the RVE development will also be discussed. A material failure scheme called crack band is introduced for modeling post-peak failure progression in the macroscale stiffened panel model. As-manufactured geometry specific computational panel results using the full multiscaling and failure models are presented for both the TBC 30 and 60 stiffened panels. Comparisons are made with experimental results aimed to quantify the accuracy and validity of the developed computational modeling strategy.

5.2 Macroscale Stiffened Panel Model

The general-purpose finite-element program Abaqus [58], [59] is used to develop and analyze the computational models of the unitized stiffened composite textile panels. A macroscale model, consisting of the stiffened-panel geometry with skin, stiffener, and flange sections, is created. The panel is modeled as a thin shell structure in 3D space. This allows increased computational efficiency compared to continuum elements while still successfully capturing the in-plane and out-of-plane bending response as the thickness is small compared to section spans. As the macroscale model does not incorporate architecture of the TBC 30 and 60 material directly, homogenized material properties are used in the shell and material descriptions. Panel geometry is defined to be the same as the nominal manufacturing geometry shown in Figure 2.9. Modeling results using the nominal section thicknesses are labeled as “linear-elastic” in all data plots. The nominal 2.7-mm skin thickness used in the initial macroscale model was later altered to include the section-specific skin thicknesses as calculated from the as-manufactured geometric imperfection data reduction effort in section 3.3. The section-specific thicknesses were coupled with the multiscale framework analysis with crack band post-peak material model.

Boundary conditions for the macroscale stiffened-panel model are implemented to emulate those in the experimental compression tests. The gage section in the tests is the same as the length modeled in Abaqus. The side edges are free, and the top and bottom edges are modeled as clamped with displacements u, v, and w and rotations ru, rv, and rw set to zero. The top edge experiences a compressive displacement-control loading condition to simulate the displacement-control loading by the platen. All other translational and rotational degrees of freedom on the top and bottom edges are restricted. As reported in [20], the TBC 30 material is modeled as an orthotropic lamina with homogenized stiffness. The elastic TBC 30 material properties are given in Table 5.1. TBC 60 material properties are given in Table 5.2. Note that the TBC 60 material is almost quasi-isotropic despite having distinct braided architecture. Until the initiation of crack band, which is discussed in a later section, the macroscale model uses linear-elastic material properties.

Table 5.1: TBC 30 material properties

E_1 (GPa)	53.1
E_2 (GPa)	7.3
ν_{12}	0.93
G_{12} (GPa)	8.3

Table 5.2: TBC 60 material properties

E_1 (GPa)	23.2
E_2 (GPa)	22.1
ν_{12}	0.3
G_{12} (GPa)	11.8

The macroscale model is meshed with S4R shell elements. The S4R element is a linear, four-noded, reduced-integration, finite-strain shell element implemented within Abaqus [59]. A mesh convergence study was performed so that the first buckling mode eigenvalue converged. The minimum number of elements across the short span of the stiffener section was restricted to be four because any fewer and appropriate buckling mode shapes would be difficult to resolve correctly in those sections. The macroscale

model was used in two analysis types. The first is a linear perturbation eigenvalue analysis to obtain initial buckling loads and mode shapes.

The second is a geometrically nonlinear response analysis where the nominal geometry is seeded with imperfections based on the calculated mode shapes from the buckling analysis. The TBC 30 panel is seeded with an imperfection of the first buckled mode shape for the TBC 30 panel. The magnitude of the imperfection is scaled to be 10% of the nominal skin thickness at 0.27-mm. This imperfection creates the postbuckling analysis to be a non-linear response problem. Figure 5.1 provides the nominal section thickness buckling loads and corresponding buckling modes for the first eight returned modes for the TBC 30 material panel. Modes one through 5 exhibit reasonable combinations of single and multiple half waves along the width and length of each panel section. It is interesting to note that mode two has two adjacent sections that buckle in the same direction (away from the reader in this case) whereas mode 3 has all skin sections buckling toward the reader. With each incremental mode, the buckling load increases fairly consistently until modes seven and eight which have significantly increased buckling loads.

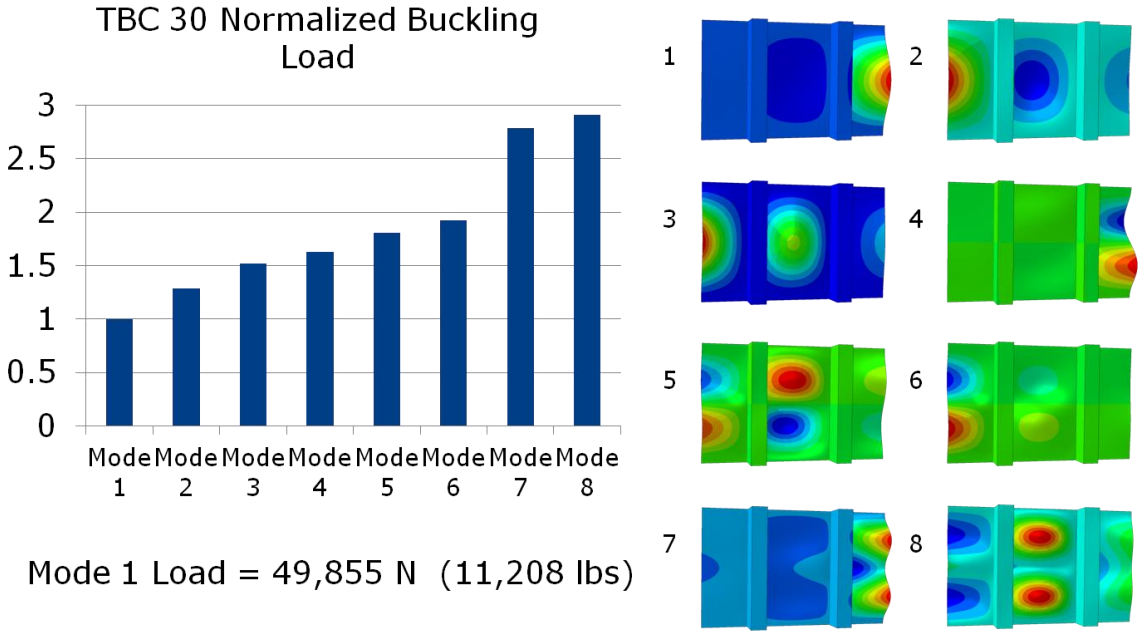

Figure 5.1: TBC 30 linear buckling analysis with nominal section thickness. Note scale in mode shapes are normalized to unitary magnitude.

Figure 5.2 shows the load vs. displacement response for the nominal-section-thickness model analysis with TBC 30. The only material description used is a linear-elastic, orthotropic, homogenized lamina description as given in Table 5.1. The end of the computational load vs. displacement curve in Figure 5.2 is determined by a maximum compressive strain criteria that was initially used to estimate the approximate failure strain as determined from previous TBC 30 material investigations. When a strain value in the model exceeds a critical strain, the solver ceases the computational analysis iteration and the run terminates. Note that the buckling load is approximated well, as is the buckling mode shape of one half wave. However, the postbuckling stiffness of the nominal panel is less than the experimentally observed behavior. Part of this difference is explained and accounted for by implementing section-specific thicknesses in the multiscaling framework macroscale model and explained in further detail in section 3.3. The results of the section thickness implementation are discussed later in sections 5.6 and 5.7. The linear-elastic model also exhibits a higher stiffness at loads near where the experimental panels failed. This indicates that there is a softening of material properties during postbuckling prior to the main structural failure event. The extension of the maximum strain criteria well beyond the experimental curves also indicates that this simple failure model is not appropriate even capable of accurately capturing the observed response in this work.

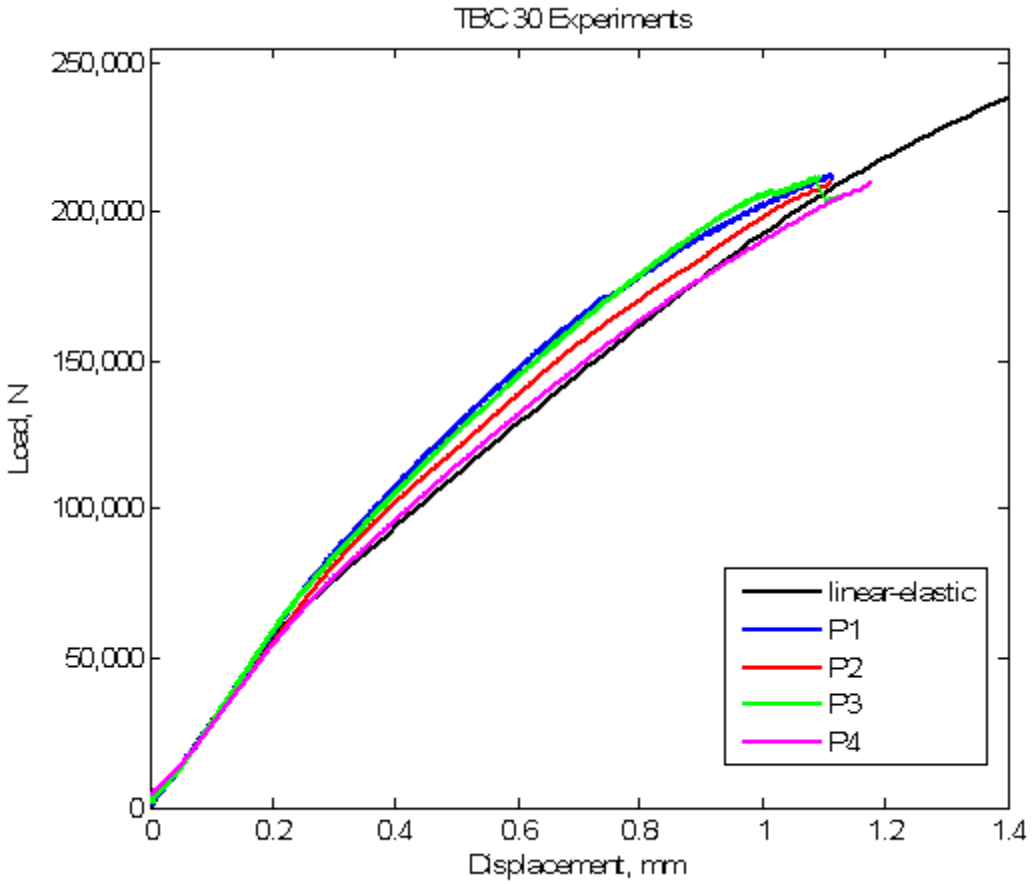

Figure 5.2: TBC 30 linear-elastic postbuckling with nominal section thicknesses

Figure 5.3 provides the nominal section thickness buckling loads and corresponding buckling modes for the first eight returned modes for the TBC 60 material macroscale model. Note that the mode shapes for the TBC 60 nominal section thickness model are different starting at the second mode. The first mode shape is the similar to the first mode shape of the TBC 30 model previously discussed. The second mode shape of the TBC 60 model, however, includes two half waves along the axial loading direction in each of the skin sections. This mode shape, although associated with a higher buckling load, is similar to the mode shape the experimental panels switched to while loading well into the postbuckling range. Also, modes five and up exhibit somewhat unrealistic mode shapes with over twice the buckling load associated with the first mode. The TBC 60 nonlinear response analysis panel is also seeded with an imperfection based on the TBC

60 panel buckling analysis. In addition to the 10% scaled nominal skin thickness imperfection magnitude of the first buckled mode shape, the TBC 60 panel macroscale model is seeded with an additional mode-shape imperfection. The additional imperfection is scaled to 1% of the nominal skin thickness of the second buckled mode shape. This secondary imperfection seeding in the TBC 60 macroscale panel is required in order to effectively capture the postbuckling secondary mode switch that was observed in the experimental tests. The second buckled mode shape corresponds to the double half-wave mode that the panel switches to after first transitioning into the regular single half-wave mode shape after loading beyond the buckling limit.

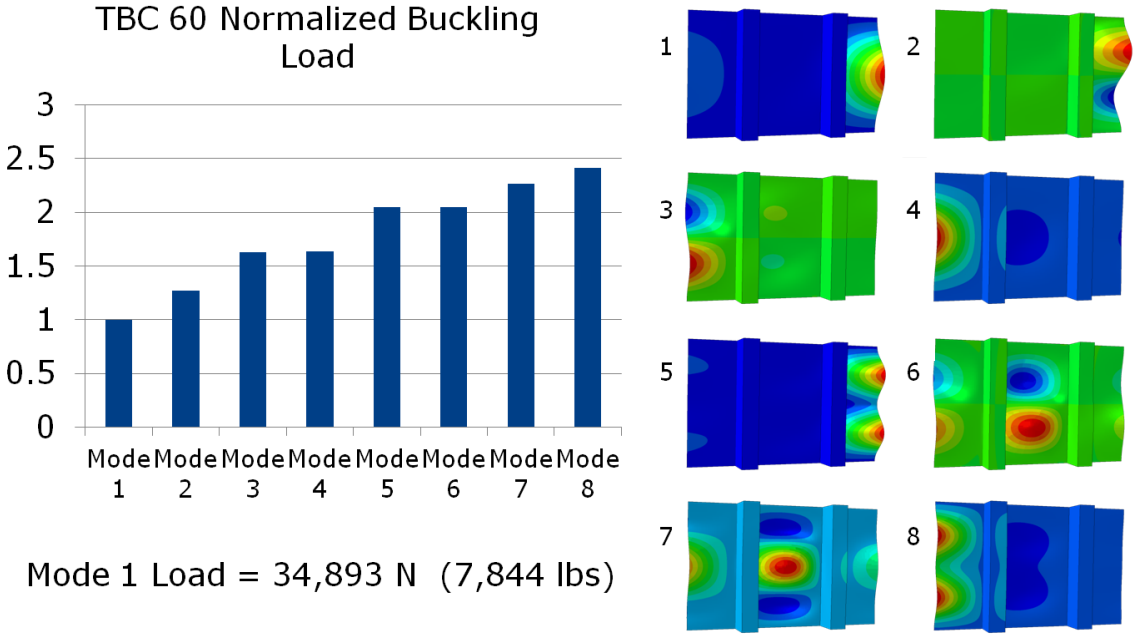

Figure 5.3: TBC 60 linear buckling analysis with nominal section thicknesses. Note scale in mode shapes are normalized to unitary magnitude.

Figure 5.4 shows the load vs. displacement response for the nominal-section-thickness model analysis with TBC 60 material. The only material description used is a linear-elastic, orthotropic, homogenized lamina description as given in Table 5.2. The end of the computational load vs. displacement curve in Figure 5.4 is based on the maximum strain criteria that was initially used to estimate the approximate failure strain determined from previous TBC 60 material investigations similarly to the TBC 30 criteria previously discussed. The buckling load is captured well, as is the initial buckling mode

shape and secondary buckling mode switch. The mode switch for the TBC 60 model is captured using a Riks analysis because the mode switch event, while not necessarily a dynamic event, is characterized by a snap-back phenomenon. The snap back is not as severe as for cylindrical shells, for example, and is difficult to observe from the curves shown in Figure 5.4.

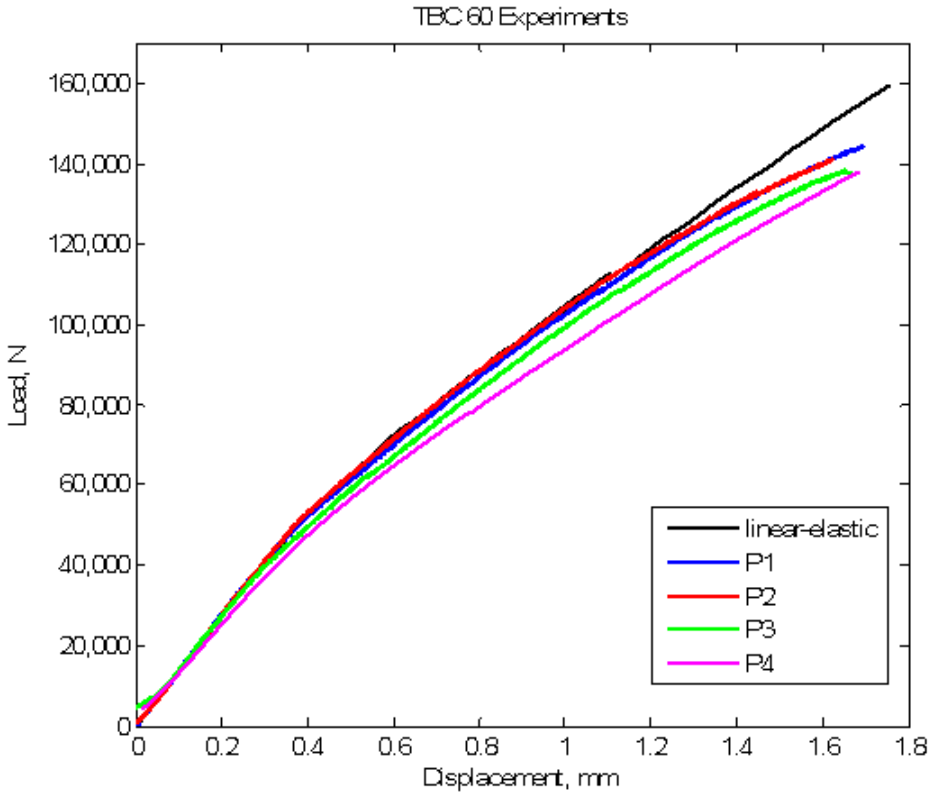

Figure 5.4: TBC 60 linear-elastic postbuckling with nominal section thicknesses

However, the postbuckling stiffness of the nominal panel is more than the experimentally observed behavior the higher the loading progresses as seen in Figure 5.4. This, as for the TBC 30 panels as well, indicates that material softening may be occurring during postbuckling and prior to the main failure event. Part of this difference is also explained and removed by the implementation of section-specific thicknesses implemented in the multiscaling framework macroscale model and explained in further detail in section 3.3. It is notable that the TBC 30 section thicknesses were usually slightly thicker than the nominal manufacturing thickness while TBC 60 section thicknesses were usually thinner. This could explain the slight under predicted stiffness

of the TBC 30 nominal thickness panel and the slight over predicted stiffness on the TBC 60 material panel. The overall prebuckling response of the stiffened panels is little changed with the section specific thicknesses, but the bending nature of the postbuckling stiffness is more heavily influenced because the bending response is proportional to the cube of the thickness. The stiffened-panel macroscale model forms the base of the multiscale framework discussed in the next section.

5.3 Multiscale Framework

Section 4.5 discussed the architecture specific cracking and damage dependency based on the underlying TBC material. The previously described homogenized material descriptions for the TBC 30 and 60 materials, while representative of the TBC material in terms of stiffnesses, are not capable of incorporating the braided architectural effects for damage initiation and propagation. The results of the failure investigation also determined that the stiffened panels failed in a mode that is indicative of a material failure rather than a structural failure mode such as stiffener separation. These aspects suggest that incorporating damage initiation and propagation information into the macroscale stiffened panel model is needed, but the current homogenized development is not sufficiently detailed to do so. Therefore, a multiscaling framework is proposed where a mesoscale model that captures the architecture-dependent details is used to provide details that cannot be calculated with the homogenized macroscale stiffened panel model.

Multiscaling techniques are powerful tools that are actively researched to continuously improve their capability and applicability beyond academic uses [60]–[62]. Just like there are many types of finite-element analysis techniques that have certain advantages and disadvantages, multiscaling methods range from lightly coupled scales that have minimal interaction between models to fully coupled, concurrently solved frameworks that are highly dependent on communication between models. The multiscaling framework in this study uses the subscale method where a global, structural level model that does not capture features such as material architecture calls upon a smaller scale model that does incorporate such features. A braided architecture-dependent mesoscale model, specifically, is used as a criterion for the macroscale stiffened panel

model to enter the crack band material damaging model. Section 5.4 has further detail on the mesoscale model used in the multiscaling framework. The next section outlines how information is handled between models in certain multiscaling methods including the one used in this work.

5.3.1 Information Handling

Fully coupled multiscaling finite-element techniques often communicate information in the macroscale model such as temperature or deformation to a subscale model. The subscale model takes the information passed down and uses it as either boundary conditions or loading conditions. The desired analysis is then performed on the subscale model, and the critical information is determined and passed up to the macroscale model. For stress analysis in finite element programs, local element strains or deformation gradients are typically the information that is passed to the mesoscale model. The information passed back up to the macroscale model is usually the stress update and Jacobian. The Jacobian in this circumstance is the tangent stiffness matrix for the local stress-strain relationship at an integration point For this work, Abaqus Standard is used and not Abaqus explicit. Figure 5.5 shows a diagram of how the information cycles from one model to the other in a standard full multiscaling framework.

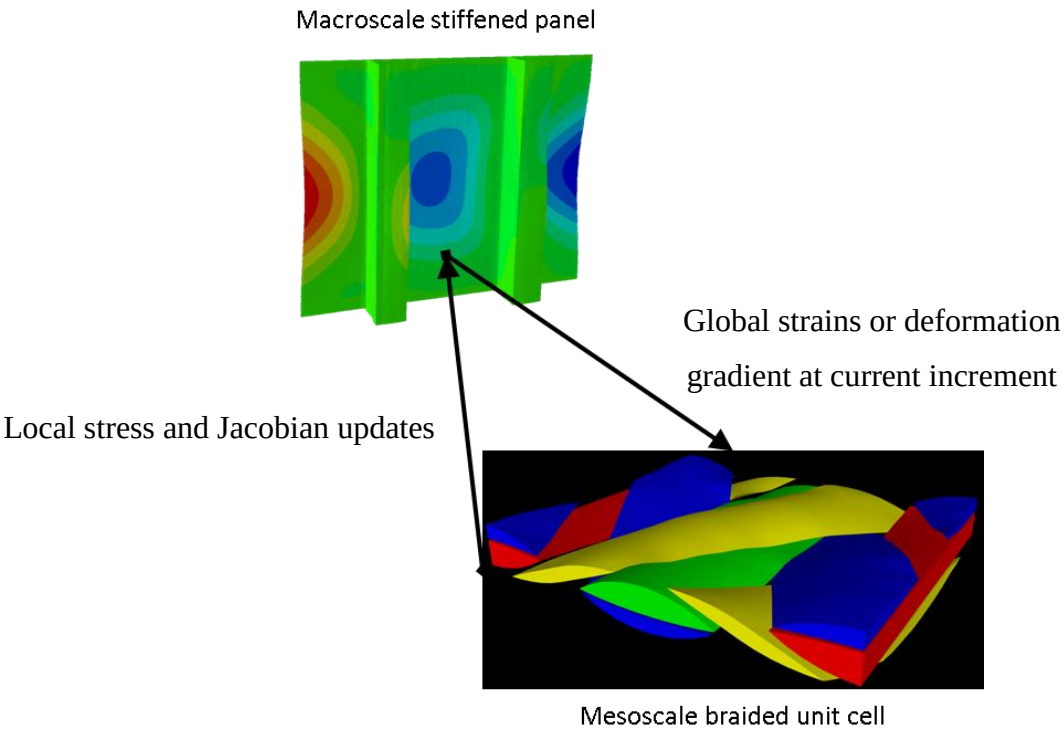

Figure 5.5: Full two-way communication multiscaling interface

This type of multiscaling is considered a two-way technique, where information is passed between both scales in a cycle. The multiscaling technique implemented for this work breaks the communication cycle in a sense because boundary condition and loading information is passed down to the mesoscale, but there is no stress update or Jacobian returned to the macroscale model. Instead the mesoscale model is used as a damage initiation criterion for the macroscale model. If the loading conditions are sufficient to cause a negative tangent slope in the load vs. displacement history in the mesoscale model, a damage indicator flag is returned to the macroscale model so that the current element enters the crack band model discussed in section 5.5. If the damage flag is not returned, the macroscale model continues as a linear-elastic material and checks for a negative tangent slope in the next increment. If the damage flag is already present in an element because damage was initiated at a previous increment, the mesoscale model is not called and the element uses the crack band model to return the updated stresses and Jacobian. Figure 5.6 shows a diagram of the information handling in the top-down approach to multiscaling used in this analysis. The term top-down simply indicates that

information is passed to the mesoscale model, but the mesoscale model does not pass significant information up to the macroscale model except for the damage flag.

Scripting is used in this work to control the flow of information between the macroscale and mesoscale models, as well as the data analysis to determine if the mesoscale model experiences a load drop. An Abaqus User Material (UMAT) subroutine is used in the macroscale model instead of a built in material model. This is done to be able to execute the mesoscale model directly via command line in the macroscale UMAT. The UMAT also writes the integration point's current deformation gradient to a text file. A User Displacement (DISP) subroutine, implemented in the mesoscale model, reads the deformation gradient from the text file and extracts the strain information to apply the appropriate displacement conditions to the mesoscale model. Once the mesoscale run terminates, a Python [63] script then determines whether a load drop occurred in the

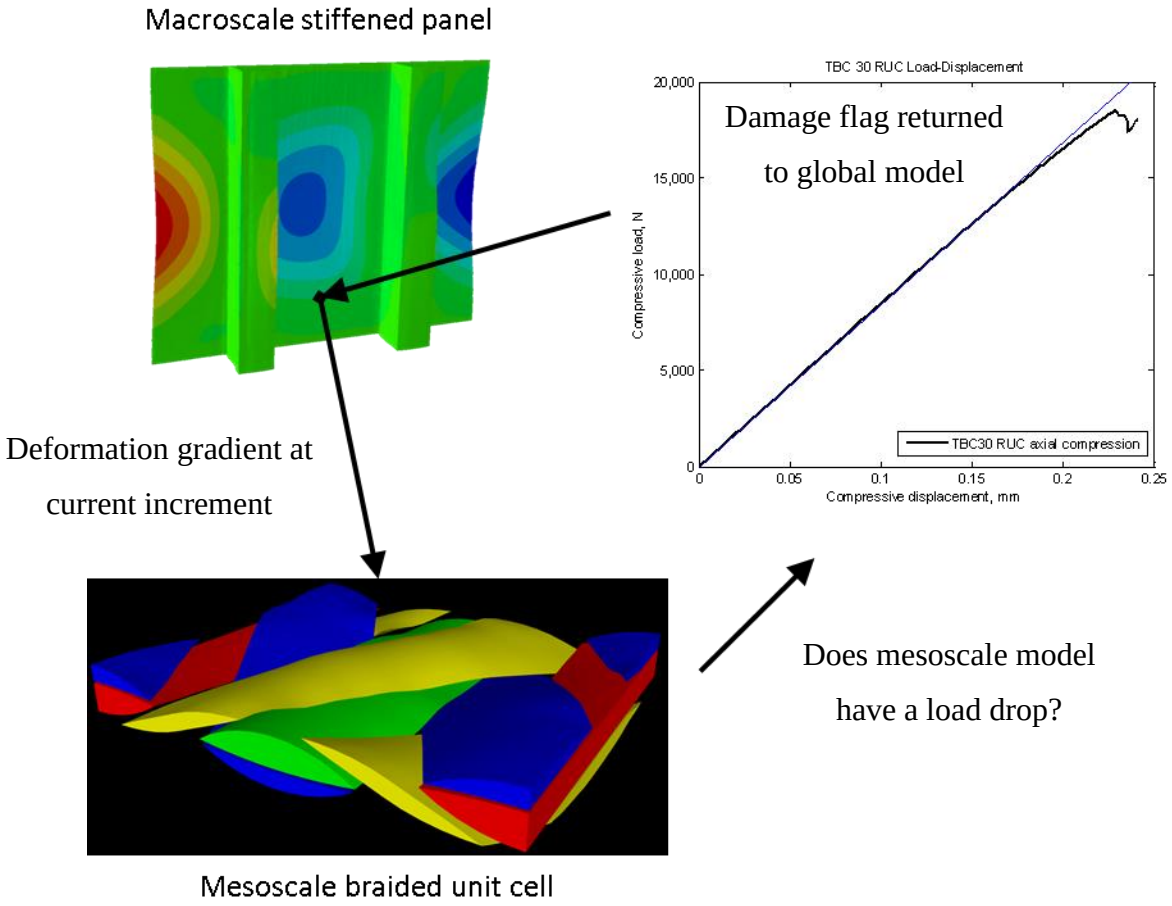

Figure 5.6: One-way top-down multiscaling communication interface

mesoscale model and, if so, returns the damage flag and maximum axial stress to the macroscale model UMAT. This procedure then repeats for each integration point at each element for each iteration of the macroscale stiffened panel model.

5.4 Representative Volume Element Development

The mesoscale model previously outlined in the multiscaling framework section incorporates TBC 30 and 60 architecture specific geometries by directly modeling fiber tows and resin rich areas for an RVE. The textile modeling software TexGen [64] is used to design the TBC 30 and 60 RVE model geometries. Tow geometry such as cross-section shapes, widths, and heights, and tow properties such as bias braid angle were developed based on the geometrical investigation data obtained from previous studies [20]. Specifically, the cross-section dimensions for the axial and bias tows as each have different cross-sections, were used to develop the TBC 30 and 60 RVE. TexGen has tow geometry definition capabilities that would be difficult to simulate in other conventional 3D modeling software. An example is lenticular tow cross sections, commonly described as a cusped ellipse, are used in the TBC RVEs because they most closely resemble the cross sectional shape visually observed in the TBC material. Traditional ellipses were once thought to best model the fiber tow cross sections, however the VARTM manufacturing method compacts the fiber tows closer together and removes much of the resin rich pocket areas. Tow nesting results in a higher tow volume fraction after the VARTM process as well as the observed lenticular cross section with cusped corners instead of rounded corners as seen in Figure 5.7.

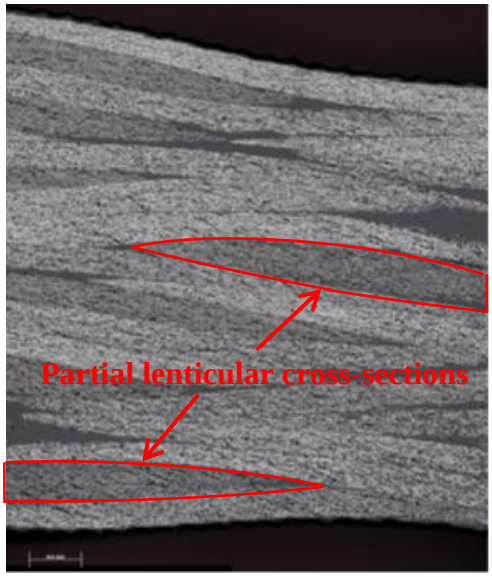

Figure 5.7: TBC fiber tow nesting of lenticular cross section

Figure 5.8 shows the individual tow geometry of the TBC 30 textile material. This geometric model was then imported into Abaqus to define the RVE using a Boolean operation to surround the tows with a block of pure matrix. It was attempted to simulate the compaction of dry textile resulting from the VARTM manufacturing process, however numerical difficulties prevented using the simulated TBC dry textile as the basis for the RVE. Instead, local tow cross-section warping effects were implemented into the idealized geometry of the TexGen model to bridge the gap between the perfect geometry and the fully compressed simulation geometry.

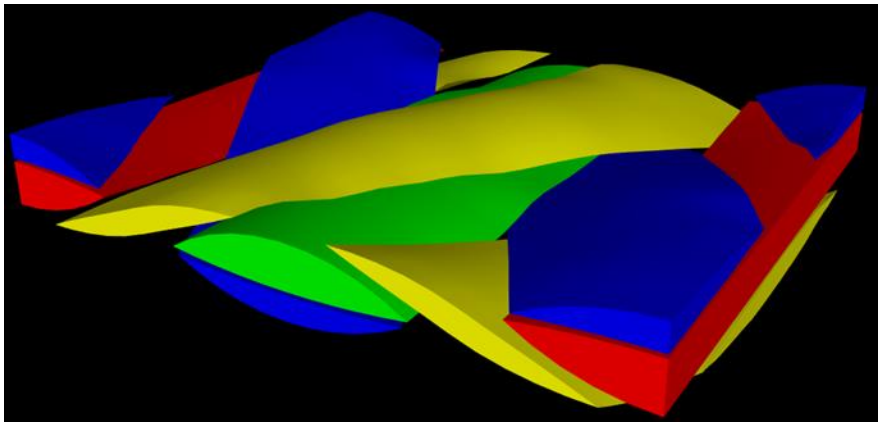

Figure 5.8: TBC 30 RVE as modeled in TexGen

As a result, the ratio of the volume in the RVE taken up by the tows compared to the overall total volume, or tow volume fraction V_t, was significantly increased compared to the idealized initial geometry. Table 5.3 shows the results of the tow compaction analysis for both the TBC 30 and 60 dry textile tows. Figure 5.9 shows the tow geometry used for the TBC 60 textile material. This geometric model was also imported into Abaqus to create the finite element model RVE used in the multiscaling framework and analysis previously discussed.

Table 5.3: RVE Tow Compaction Study Results

	V_t prior to compaction	V_t post compaction
TBC 30 RVE	36.2%	48.4%
TBC 60 RVE	36.6%	48.7%

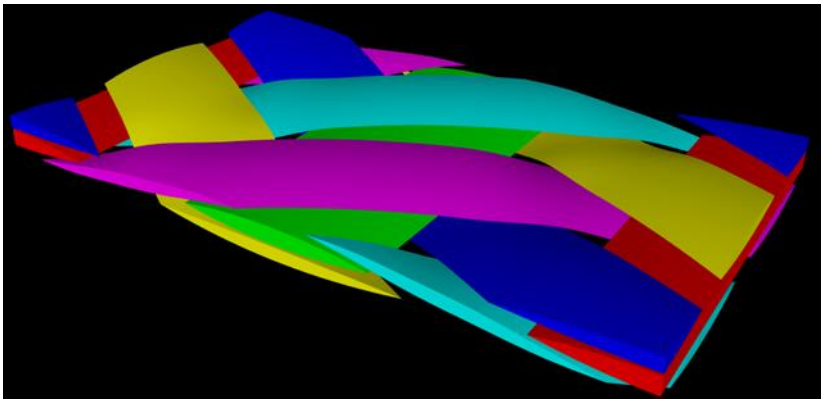

Figure 5.9: TBC 60 RVE as modeled in TexGen

The RVE finite element models were meshed using linear tetrahedral elements, C3D4 in Abaqus. Linear tetrahedral elements were chosen for computational efficiency as well as being able to successfully mesh the complicated geometry for both the TBC 30 and 60 RVEs. 8-noded brick elements simply cannot be used as the cusped points of the lenticular cross sections of the fiber tows would create highly distorted elements. Higher order tetrahedral elements would be preferred in most cases, however, the simple size of the RVE mesh (400,000 elements for a medium-refined mesh) makes quadratic

tetrahedral computationally time-intensive to use while minimally altering the stress state.

Displacement-based periodic boundary conditions (PBCs) [10], [33], [65]–[67] were implemented on the exterior surface nodes for the TBC 30 and 60 RVEs via the linear constraint equation command in Abaqus. PBCs are a numerical technique to effectively model a single piece of material like the TBC RVE yet return stiffness values that simulate the piece of material like it is surrounded by self-similar material [68]. Free boundary conditions can return dramatically lower stiffness values when analyzing computational material properties. Fixed boundary conditions can return slightly higher stiffnesses than actually observed values, but also cannot be used to determine shear moduli. PBCs are in between fixed and free boundary conditions as far as stiffness calculation and also make physical representation of a continuum in a non-continuum model. Figure 5.10 visually demonstrate the effect of implementing PBCs on an RVE for a given material. The formulation for 3D PBCs are widely available in literature [69] and thus are not repeated here. Xia in [70] demonstrates that the choice of repeat unit cell may not be unique, and proper periodic boundary condition implementation returns correct stiffness on a displacement and traction continuity basis. It should be noted that

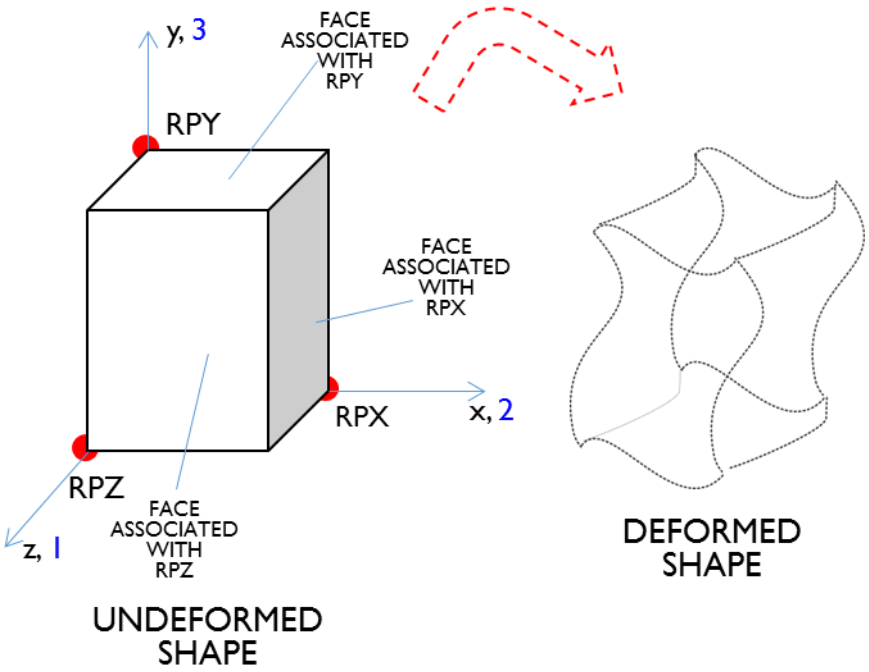

Figure 5.10: Periodic boundary condition constraints

reference nodes, RPX, RPY, and RPZ are created with the PBC formulation so that external loading conditions as supplied by the multiscaling framework may be applied to the RVE.

Non-linear material properties from the TBC 45 tension test characterization as described in section 4.3 are incorporated into the mesoscale RVEs. The equivalent stress-strain curves given in Figure 5.11 are used in conjunction with Hill's anisotropic potential. There are numerous ways with which to model non-linear material behavior, and Hill's anisotropic potential was chosen due to the applicability of available data and the manner in which the non-linear effects manifest within the RVEs [13], [71]–[73].

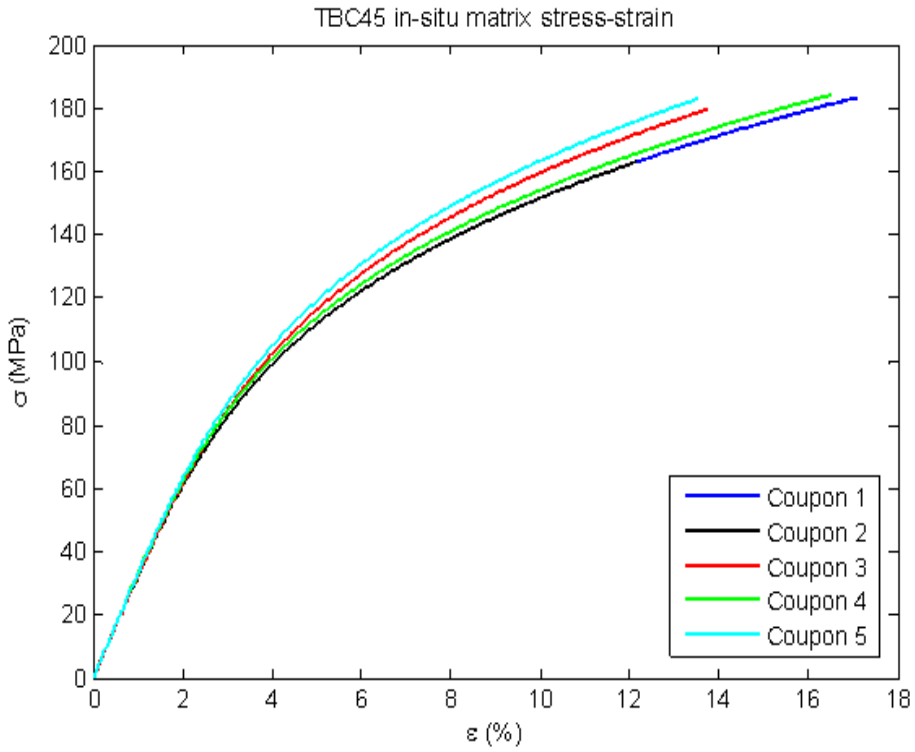

Figure 5.11: In-situ equivalent fully non-linear stress-strain

Hill's anisotropic potential, given by (5.1), is composed of weighted yielding terms due to the anisotropic nature of fiber tows.

$$f = F(\sigma_{22} - \sigma_{33})^2 + G(\sigma_{33} - \sigma_{11})^2 + H(\sigma_{11} - \sigma_{22})^2 + 2L\tau_{23}^2 + 2M\tau_{13}^2 + 2N\tau_{12}^2 \quad \textbf{(5.1)}$$

Each weighting term, given by letters F-H and L-N, are each composed of equations given by (5.2).

$$\begin{aligned} F &= \frac{1}{2}\left(\frac{1}{R_{22}^2}+\frac{1}{R_{33}^2}-\frac{1}{R_{11}^2}\right) \\ G &= \frac{1}{2}\left(\frac{1}{R_{11}^2}+\frac{1}{R_{33}^2}-\frac{1}{R_{22}^2}\right) \\ H &= \frac{1}{2}\left(\frac{1}{R_{11}^2}+\frac{1}{R_{22}^2}-\frac{1}{R_{33}^2}\right) \\ L = \frac{3}{2R_{23}^2}&, M = \frac{3}{2R_{13}^2}, N = \frac{3}{2R_{12}^2} \end{aligned} \tag{5.2}$$

A reference yield stress, σ_0, is used in combination with yield strengths in primary directions to form the R_{ij} terms. The R_{ij} terms are given by equations (5.3) where σ_0 and τ_0 are determined from the application of the non-linear matrix material behavior in the concentric cylinder model (CCM) equations.

$$R_{11} = \frac{\sigma_{11}^C}{\sigma_0}, \qquad R_{22} = \frac{\sigma_{22}^C}{\sigma_0}, \qquad R_{12} = \frac{\tau_{12}^C}{\tau_0}, \qquad etc. \tag{5.3}$$

Using the CCM equations [36], the non-linear matrix equivalent secant modulus obtained from the experimental tests is used as an array rather than a single material constant. The CCM equations now return an array of tow moduli values for each value of the non-linear matrix modulus. The results of the non-linear matrix secant modulus in the CCM equations is shown in Figure 5.12. As the pure in-situ matrix is isotropic, a standard 0.2% strain offset was used to calculate the yield limit and therefore the reference strengths. Note that σ_{22} and τ_{12} were used as the axial and shear reference strengths, respectively, where the reference strengths are given by equations (5.4).

$$\begin{aligned} \sigma_0 &= 177\ MPa \\ \tau_0 &= 102\ MPa \end{aligned} \tag{5.4}$$

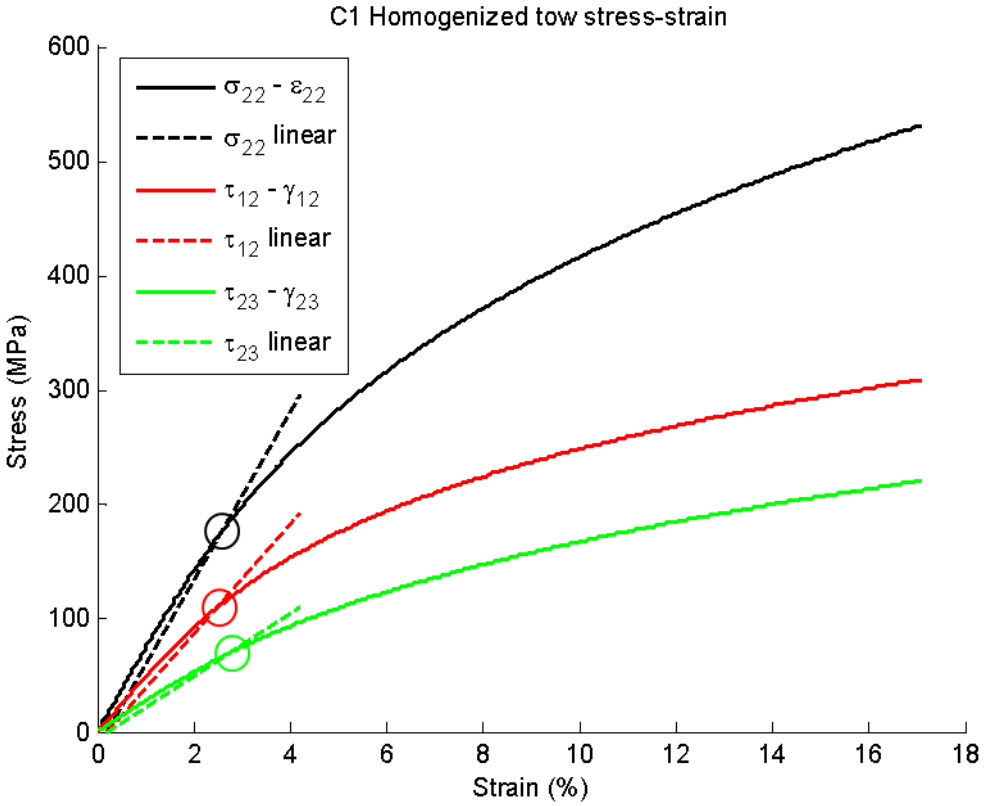

Figure 5.12: Homogenized non-linear stiffnesses for a fiber tow

With the reference strengths determined, the R_{ij} terms are calculated as previously given. Table 5.4 provides the values used. Note that R_{11} is set arbitrarily high as the non-linearity in the fiber direction is assumed small due to the fiber dominated response and that the fiber is assumed to remain linear-elastic.

Table 5.4: R_{ij} terms used in Hill's anisotropic potential

R_{11}	R_{22}	R_{33}	R_{12}	R_{13}	R_{23}
10000	1.0	1.0	1.06	1.06	0.68

5.4.1 TBC RVE Response

With the resin rich areas modeled as non-linear using the in-situ matrix equivalent stress-strain curve as shown in Figure 5.11, and with the fiber tows modeled as materially non-linear using a micromechanics incorporation of the same curves, the TBC 30 and 60 RVEs are effectively fully non-linear from a material modeling sense. Subjecting the RVEs to axial compressive loading through the reference PBC nodes as that is the primary loading condition encountered by elements in the macroscale stiffened panel, a material limit is reached. At a certain point, an axial fiber tow enters the plastic regime and forms a local buckling or kink structure. Figure 5.13 shows an example of this behavior for the TBC 30 RVE. Note that the local buckling occurs in the axial tow approximately a quarter of the length along the tow and not in the center. All surrounding matrix and other tows have been removed for clarity.

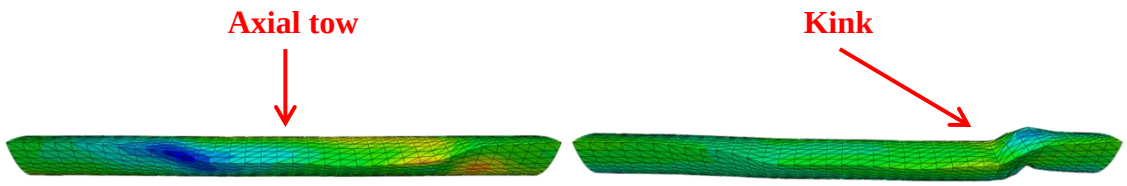

Figure 5.13: Axial tow locally buckling due to plastic deformation – other fiber tows and resin rich areas are removed for clarity. Contours are Mises stress, but the kink behavior is the highlighted feature

This local buckling is a direct result of modeling the material non-linearity of the matrix rich regions and the orthotropic fiber tows. Such behavior would not be possible without including the non-linear matrix material data. When the local buckling event occurs, there is a load drop (i.e. negative tangent slope in the load vs. displacement response) of the mesoscale model. This corresponds to a significant loss in load carrying capability of the material resulting from the loading conditions in the macroscale model. Therefore, the occurrence of a negative tangent slope in the load vs. displacement response for a TBC 30 or 60 RVE is used as the critical criteria of the macroscale User-Material (UMAT) to enter the crack band material model. Figure 5.14 shows a

corresponding load vs. displacement curve for the TBC 30 RVE when the axial tow buckles. The response is linear up until approximately 13,000 N. At this point, a small deviation is observed and gradually lessens the slope with continued loading. There is a negative slope near 18,000 N corresponding with the initiation of the local buckling event.

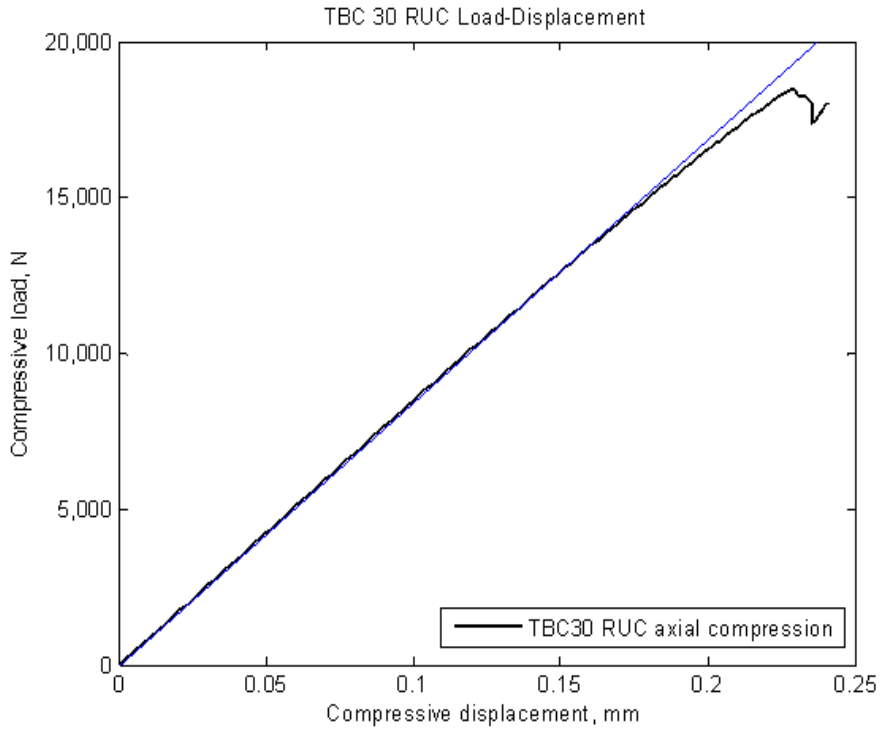

Figure 5.14: RVE load vs. displacement response highlighting the characteristic load drop upon axial tow local buckling

In order to capture the load-drop behavior and successfully flag the element in the multiscaling framework as having initiated damage, a numerical stabilization scheme was added to the RVE mesoscale model. This automatic feature within Abaqus effectively adds viscous nodal forces when nodal velocities become large. It is preferred to use numerical stabilization techniques like this over schemes like Riks analysis when local material instabilities occur [31], [74]–[77]. Riks analyses are often better suited to global instabilities instead of local ones [59]. Figure 5.15 shows that the static dissipation energy due to using the automatic stabilization scheme is small compared to the overall strain energy of the model for the mesoscale model in simple axial compression. This result

indicates that the accuracy of the load drop is reasonable and the damping forces are not dominating the solution.

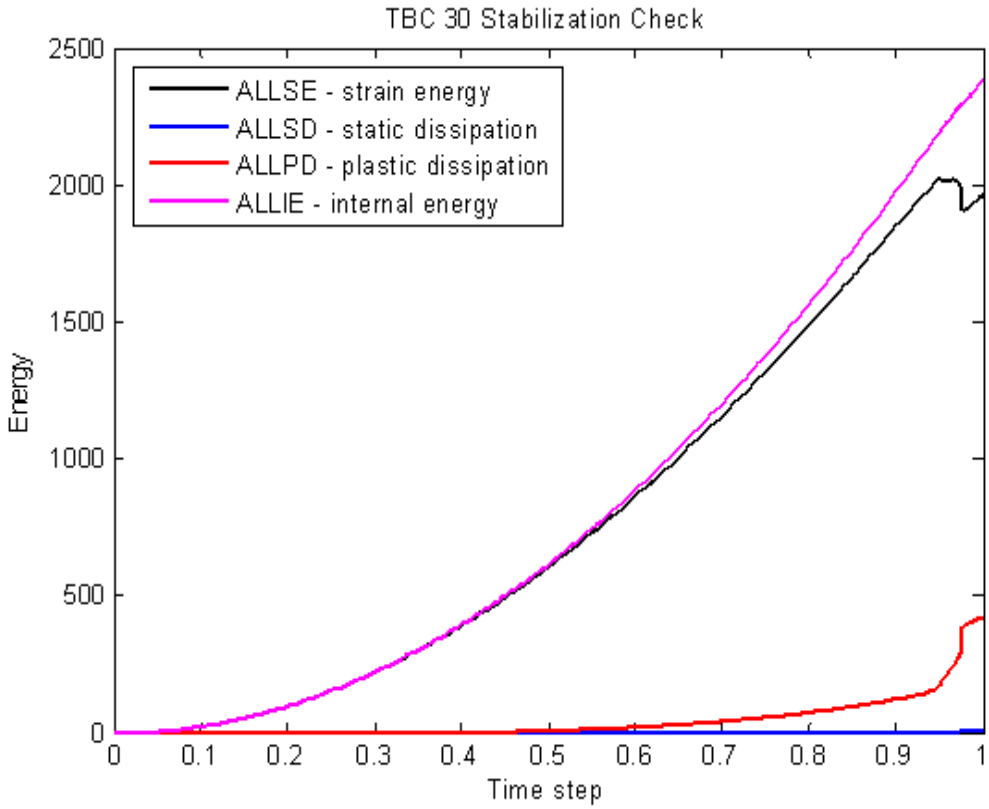

Figure 5.15: RVE energy validation for automatic stabilization check

When the first occurrence of a negative slope is encountered, a post-processing script calculates the axial stress just prior to the load drop by dividing the load value over the area of the mesoscale model. The critical stress value is returned to the macroscale model in an internal variable and is used by the crack band formulation as discussed in the next section. Using this method, individual elements are allowed to have different critical stress values depending on the loading conditions that caused the load drop in the RVE.

5.5 Crack Band

As shown in section 5.2, deviation in the load-displacement curves of the experiments from the linear elastic material stiffened panel model can be significant in the TBC 60 panels and present in some of the TBC 30 panels. This softening behavior is the result of the accumulation of damage in the TBC material prior to the final failure load and corresponding load drop. The damage manifests by the formation of matrix micro cracks in the polymer matrix material [35]. The location of these cracks is within the fiber tows as well as in resin rich areas between fiber tows. Previous work has been developed to effectively model this micro cracking behavior both in a microscale and macroscale level [51], [78]–[80]. In this work, the term damage refers to the release of energy due to micro cracking. It is typically characterized by a softening stress-strain response law [4], [56].

Micro cracking initiates at some critical parameter during analysis, often a critical stress or strain, and ends at a critical failure parameter often a maximum strain or similar type condition. After fully progressing through the softening stress-strain behavior and beyond the critical failure parameter, failure is defined as the post peak regime where all energy is dissipated and a distinct failure surface is created. Traction cannot be carried across this surface, and as such the material experiences a complete loss in stiffness in the secant sense. To avoid this issue, the failure tangent stiffness is not decreased to zero. Instead, it is set to a very small number. This residual stiffness is for purely numerical reasons, yet it does not alter the response as it is so small in comparison to the undamaged modulus. As a result of a softening stress-strain relation, there is a loss of positive-definiteness of the instantaneous stiffness tensor and causes material instability. This instability is resolved at the element level for smeared or similarly named distributed damage methods. As the primary observed failure mode of the tested stiffened panels was tow failure due to local buckling, only Mode I cracks are considered. Mode I cracks are those that have no shear (i.e. Mode II or mixed-mode) at the crack tip.

As mentioned in section 5.4, the criterion used to initiate damage and enter the softening regime of the material law is governed by the TBC 30 or 60 RVE. The occurrence of a negative tangent load-displacement slope (i.e. a load drop) causes the

local homogenized element in the macro scale model to enter crack band. Unlike other criteria methods such as critical stress or strain [81], using the TBC RVEs as the initiation criteria incorporates the architecture dependent nature of damage as previously observed in Figure 4.30 and Figure 4.31. As crack band is one version of the type of damage and failure methods labeled as smeared methods, a discrete crack does not manifest in the macroscale model. Instead, the equivalent damage or failure is distributed across the entire element that has entered crack band. This is handled through the formation of the element stress-strain constitutive law. After entering the damaging constitutive law, the stiffness in the direction perpendicular to the crack is reduced. The stiffness reduction is governed by a traction separation law. As the RVE serves as the criteria that must be satisfied to enter crack band, the macroscale homogenized element does not directly observe the occurrence of the local axial tow buckling behavior. Instead, the crack band orientation is set by aligning the crack normal to the maximum principal strain direction upon entering the separation law.

A triangular traction separation law is used for the implementation of crack band. The area under the curve is related to the Mode I fracture toughness, G_{IC}, of the TBC material. The value for G_{IC} was left as a parameter to adjust in the computational analysis. The crack band model as implemented [4] also has the benefit of mesh objectivity formulated into the stiffness degradation via the traction separation law. Mesh objectivity is highly desirable as the results will in general not depend on mesh refinement as long as certain element size criteria are satisfied. It is assumed that a single element's strain may be split into a continuum strain and a crack strain component given by

$$\varepsilon_{total} = \varepsilon_{con} + \varepsilon_{cr} \tag{5.5}$$

where ε_{con} is the continuum component of element strain and ε_{cr} is the cracked contribution to total element strain. The strain-stress relation can then be written as

$$\begin{pmatrix}\varepsilon_{11}\\ \varepsilon_{22}\\ \varepsilon_{33}\end{pmatrix}=\begin{bmatrix}\frac{1}{E_1} & -\frac{\nu_{12}}{E_1} & -\frac{\nu_{13}}{E_1}\\ -\frac{\nu_{12}}{E_1} & \frac{1}{E_2} & -\frac{\nu_{23}}{E_2}\\ -\frac{\nu_{13}}{E_1} & -\frac{\nu_{23}}{E_2} & \frac{1}{E_3}\end{bmatrix}\begin{pmatrix}\sigma_{11}\\ \sigma_{22}\\ \sigma_{33}\end{pmatrix}+\begin{pmatrix}\varepsilon_{nn}^{cr}\\ 0\\ 0\end{pmatrix} \quad \textbf{(5.6)}$$

for an orthotropic material. The continuum and cracked parts are assumed to be in a state of iso-stress and thus are comparable to a set of springs connected in series. The iso-stress assumption is given by

$$\sigma_{11}=\sigma_{nn} \quad \textbf{(5.7)}$$

and the triangular traction separation law is shown in Figure 5.16. Calculating the cracked strain ε_{nn}^{cr} is done using the negative slope relation shown in Figure 5.16 and is given by (5.8) and results in (5.9)

$$\varepsilon_{nn}^{cr}=\varepsilon_f+\frac{\sigma_{11}}{C_f} \quad \textbf{(5.8)}$$

$$\begin{pmatrix}\varepsilon_{11}-\varepsilon_f\\ \varepsilon_{22}\\ \varepsilon_{33}\end{pmatrix}=\begin{bmatrix}\frac{1}{E_1}+\frac{1}{C_f} & -\frac{\nu_{12}}{E_1} & -\frac{\nu_{13}}{E_1}\\ -\frac{\nu_{12}}{E_1} & \frac{1}{E_2} & -\frac{\nu_{23}}{E_2}\\ -\frac{\nu_{13}}{E_1} & -\frac{\nu_{23}}{E_2} & \frac{1}{E_3}\end{bmatrix}\begin{pmatrix}\sigma_{11}\\ \sigma_{22}\\ \sigma_{33}\end{pmatrix}+\begin{pmatrix}\varepsilon_{nn}^{cr}\\ 0\\ 0\end{pmatrix} \quad \textbf{(5.9)}$$

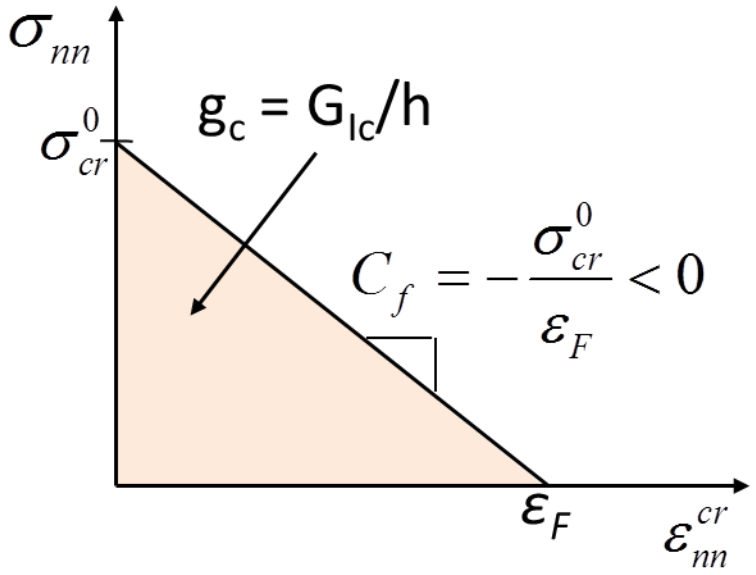

Figure 5.16: Triangular traction separation law as used in the crack band damaging material behavior

The triangular traction separation law is simple to implement and use to calculate the failure strain. The area under the curve is held as a constant, fracture toughness, so for a given critical stress value the failure strain can be determined automatically. In order to form the element stress-strain relation, the traction separation law is combined with the linear elastic material constitutive law. To achieve this, a damage parameter, D, is created. D is equal to zero if no damage exists and equal to one if the element strain ε_{11} exceeds ε_f and is fully failed. At this point, the element is considered to have no contributing stiffness despite the residual stiffness set to be extremely small for numerical stability purposes. The traction separation law and material constitutive law are combined as shown in Figure 5.17.

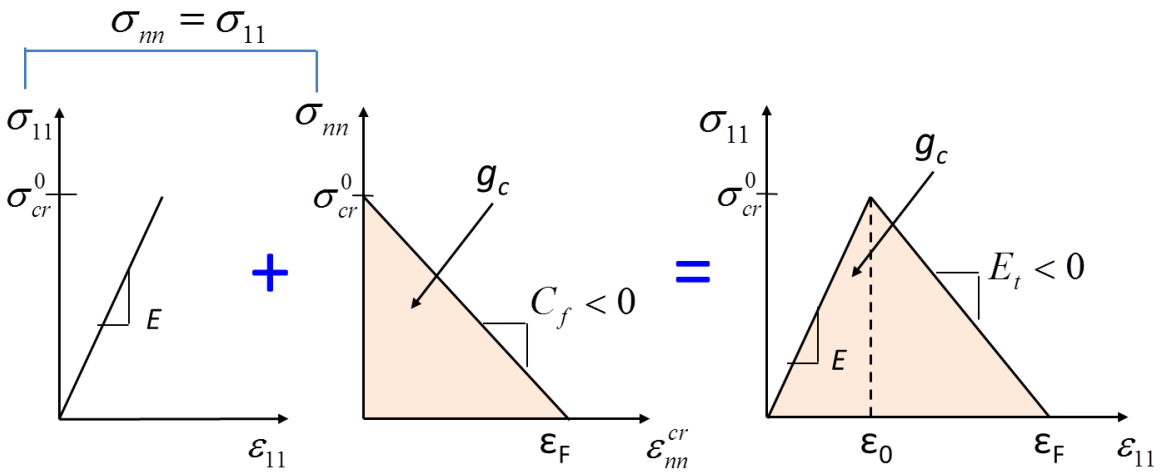

Figure 5.17: Formation of the crack band constitutive law

The damage parameter D is determined from the combined crack band constitutive law shown in Figure 5.17 by combining the equation

$$E_t = \frac{\sigma_{cr}^0}{\varepsilon_0 - \varepsilon_f} \tag{5.10}$$

with the form of the reduced secant stiffness provided in Figure 5.18 to arrive with equation (5.11). Solving this for the damage parameter D, one obtains equation (5.12). Since only the normal and shear tractions are degraded to zero at the crack, not all components of the strain-stress relation in (5.6) are affected. Equation (5.13) gives the degraded compliance matrix and shows the components that are degraded by the damage parameter.

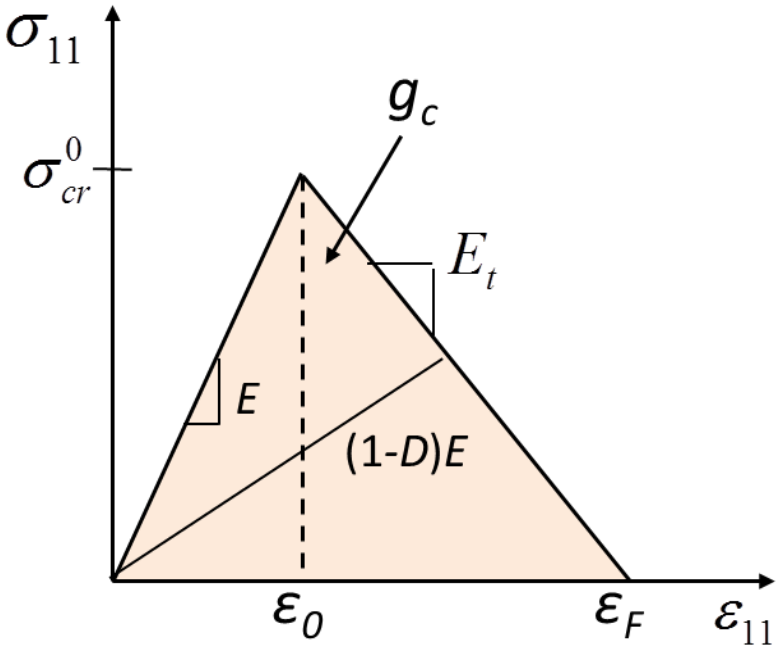

Figure 5.18: Reduced secant stiffness by damage parameter D

$$(1-D)E = \frac{E_t(\varepsilon_{11} - \varepsilon_f)}{\varepsilon_{11}} \tag{5.11}$$

$$D = 1 - \frac{\sigma_{cr}^0}{(\varepsilon_f - \varepsilon_0)E}\left(\frac{\varepsilon_f}{\varepsilon_{11}} - 1\right) \tag{5.12}$$

$$[S] = \begin{bmatrix} \frac{S_{1111}}{1-D} & S_{1122} & S_{1133} & 0 & 0 & 0 \\ S_{1122} & S_{2222} & S_{2233} & 0 & 0 & 0 \\ S_{1133} & S_{2233} & S_{3333} & 0 & 0 & 0 \\ 0 & 0 & 0 & S_{1111} & 0 & 0 \\ 0 & 0 & 0 & 0 & \frac{S_{1313}}{1-D} & 0 \\ 0 & 0 & 0 & 0 & 0 & \frac{S_{1212}}{1-D} \end{bmatrix} \tag{5.13}$$

The current implementation of the crack band method is mesh objective because a characteristic length scale [4] is introduced in the formulation of the traction separation law. Specifically, the fracture toughness G_{IC} is scaled by a characteristic element length h. Although user-defined definitions of element characteristic lengths have been developed, the characteristic element length used in the study is the length internally calculated by Abaqus. This ensures a consistent definition of element length regardless of the element type or element order. The energy released as an element's stiffness gets reduced is inherently coupled with the size of the element without any correction factors. However, when the fracture toughness is scaled with the characteristic length scale, the energy is released at a rate proportional to the element size. This preserves the total amount of energy released for a given finite element mesh.

Introduction of the characteristic length scale to obtain mesh objectivity creates a maximum element size limit in order to preserve stability. This study assumes that the pre-peak material behavior is linear and elastic. For a given critical stress and fracture toughness, the failure strain ε_f must not be less than the damage initiation strain ε_0 corresponding to the critical stress. If the failure strain is calculated to less than the damage initiation strain, the slope of the post-peak softening curve is the wrong sign and a characteristic stress drop might occur. The stress drop may even be severe enough to cause stability and convergence issues in the analysis because a snap-back type phenomenon is occurring and certain numerical solvers cannot appropriately handle such behavior. The maximum element size limit is calculated by starting with the preservation of the area under the crack band constitutive law in Figure 5.17. As shown in Figure 5.16, the slope of the softening portion of the curve must be negative. Using the relation for the negative slope in Figure 5.16 combined with (5.10), equation (5.14) can be created.

$$\frac{1}{E} - \frac{2G_{IC}}{\sigma_{cr}^2} \leq 0 \qquad \textbf{(5.14)}$$

Solving this equation for the characteristic element length, h, returns the maximum element characteristic length limit given by equation (5.15)

$$h \leq \frac{2EG_{IC}}{\sigma_{cr}^2} \tag{5.15}$$

To demonstrate how changing the characteristic element lengths alter the behavior of the crack back constitutive law, a single element study was performed. In this study, a single square element was modeled with crack band. Three different sizes of element were analyzed. The critical stress and fracture toughness used in the single element study were 190 MPa and 10 N/mm, respectively, and these values were the same for each element size. As expected from the maximum element size limit derivation, as the element size increases, the softening portion of the crack band constitutive law becomes steeper as seen in Figure 5.19.

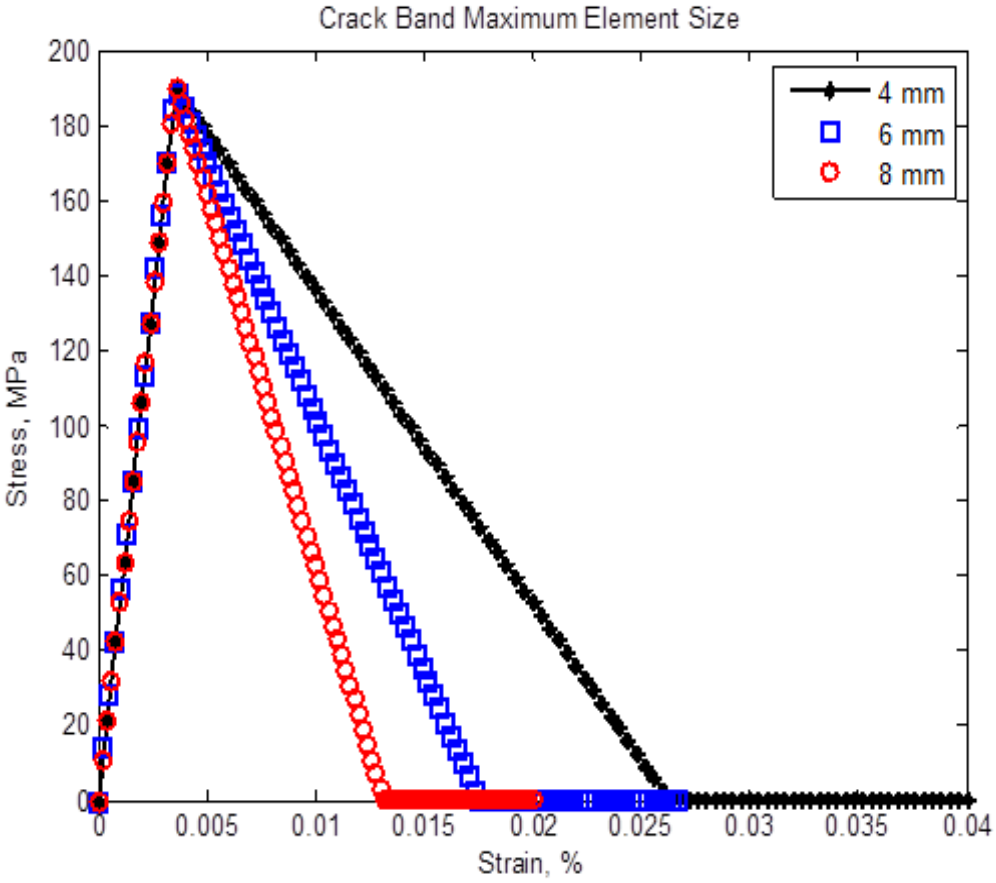

Figure 5.19: Demonstration of a maximum element characteristic length size

It is clear to see that at a certain element size, the failure strain will be equal to the initiation strain and a vertical stress drop will occur and is similar to an extremely brittle material behavior. Conversely, as the characteristic length of the element decreases, the post-peak softening becomes less steep and the failure strain increases. Taken to an extreme, an infinitesimally small element would have an infinitely large failure strain. The crack band constitutive law effectively then becomes a simple elastic-perfectly plastic model. Such mesh refinement would be prohibitively computationally costly, however, and crack band is not recommended for such modeling purposes.

It must be noted that while crack band as implemented is mesh objective, mesh refinement is still important. The mesh must be refined enough so as to resolve the stress field accurately while still maintaining feasibility with computing costs. A mesh convergence investigation with crack band may still return some slight variability in the post-peak response due to increased stress field refinement with a larger number of elements.

To demonstrate the effectiveness of crack band and show that it is mesh objective, two finite element studies were performed. Both studies used the same reduced integration S4R shell element as was used in the modeling of the macroscale stiffened panel. Both studies also used the TBC 30 linear-elastic, orthotropic material description as previously outlined for the pre-peak material model. The first test is a simple square plate loaded in axial tension. The right edge of the block was loaded in displacement control via axial tension in the x-direction. The left edge of the block was restrained in the x-direction, and the lower left corner was restrained in the y- and z-directions to prevent rigid body movements.

Four meshes labeled according to how many elements were in the x- and y-directions across the width of the plate were used in the study. In order to avoid failure initiation due to numerical error, the center element in each mesh was intentionally given a 10% lower critical stress value σ_{cr}^{0} than the rest of the elements. This ensures one element deliberately enters crack band prior to the remaining elements. A physical justification for weakening one element is to simulate a defect or imperfection in a real material. If the center element was not reduced in critical stress, numerical issues like rounding and subtraction errors would result and cause elements to enter crack band

based on non-physical reasons. The input values of fracture toughness, critical stress for the intact elements, and critical stress for the weakened element were held constant for all mesh studies and are 80 N/mm, 190 MPa, and 171 MPa, respectively.

The load-displacement results of the square block crack band validation test are provided in Figure 5.20. The pre-peak and peak load behaviors are identical, and the post-peak softening curves for all four tests are similar to within an acceptable degree. Note that there are slight deviations in the post-peak softening region. The deviations are mostly attributed to mesh refinement and activating the non-linear geometry feature within Abaqus.

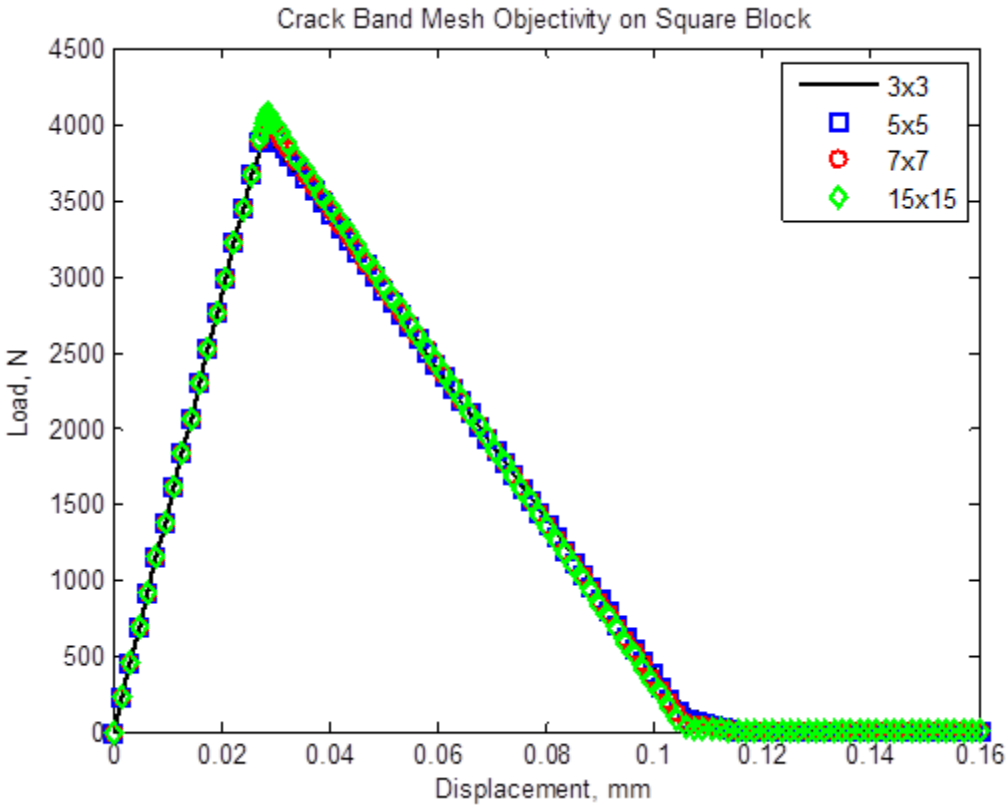

Figure 5.20: Mesh objective results for increasing mesh densities with crack band

Use of non-linear geometry within Abaqus has been documented to correspond with using logarithmic strain formulations instead of engineering strains [59]. It has also been demonstrated that using the as described crack band formulation with non-linear geometry activated in Abaqus can cause mesh dependency [82]. Using correcting terms

for G_{IC} or converting the as described crack band model to use alternative work conjugate stress-strain formulations while using non-linear geometry can remove mesh dependency when using the outlined crack band method.

Figure 5.21 and Figure 5.22 show each mesh of the simple tension block. The color scheme is showing the damage parameter D as determined from (5.12). The blue shown for most of the elements references a zero damage state where the elements are undamaged and have not entered crack band. Red references a fully failed state where the

Figure 5.21: Crack path shown in red for fully failed elements with weakened center element. Blocks are pulled in tension on the right edge

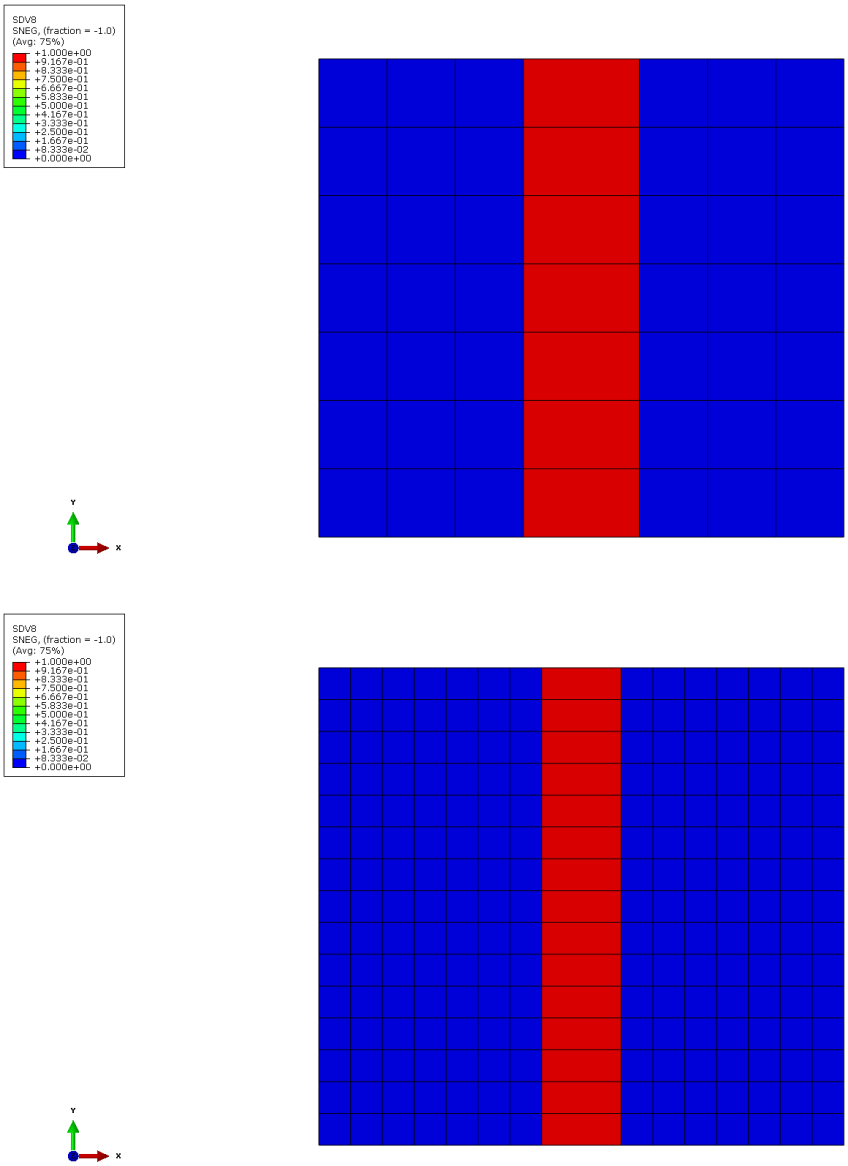

Figure 5.22: Crack path shown in red for fully failed elements with weakened center element

damage parameter D is equal to one and the element stiffness has been fully reduced. As seen in all four test cases, the center row of elements has fully failed while none of the surrounding elements have been damaged. This is expected as the weakened center element initiates a simulated crack propagating across the width of the block. Mesh objectivity is preserved.

The second finite element study is a tension coupon shaped to have a gradually narrowing waist in the middle of the gage section. The narrowing waist geometry

numerically introduces stress concentrations to the specimen when under tension and therefore there is no need to introduce an artificially weakened element. All elements in the waist models have the same critical stress criteria. Boundary and loading conditions are similar to the block test. The right edge is loaded in displacement control in the x-direction and the left edge is fixed in the x-direction. The lower left corner is again fixed in the y- and z-directions to prevent rigid body movement. The same parameters in the block crack band test were used for the waist models except that no element was weakened. Figure 5.23 provides the load-displacement curves. The pre-peak behavior and peak load are identical, and the damaging portion of the curve shows minimal change. There are again slight variances in the post-peak behavior, but they are minimal compared to the scale of change in mesh sizes and are attributed to increased refinement of the stress field.

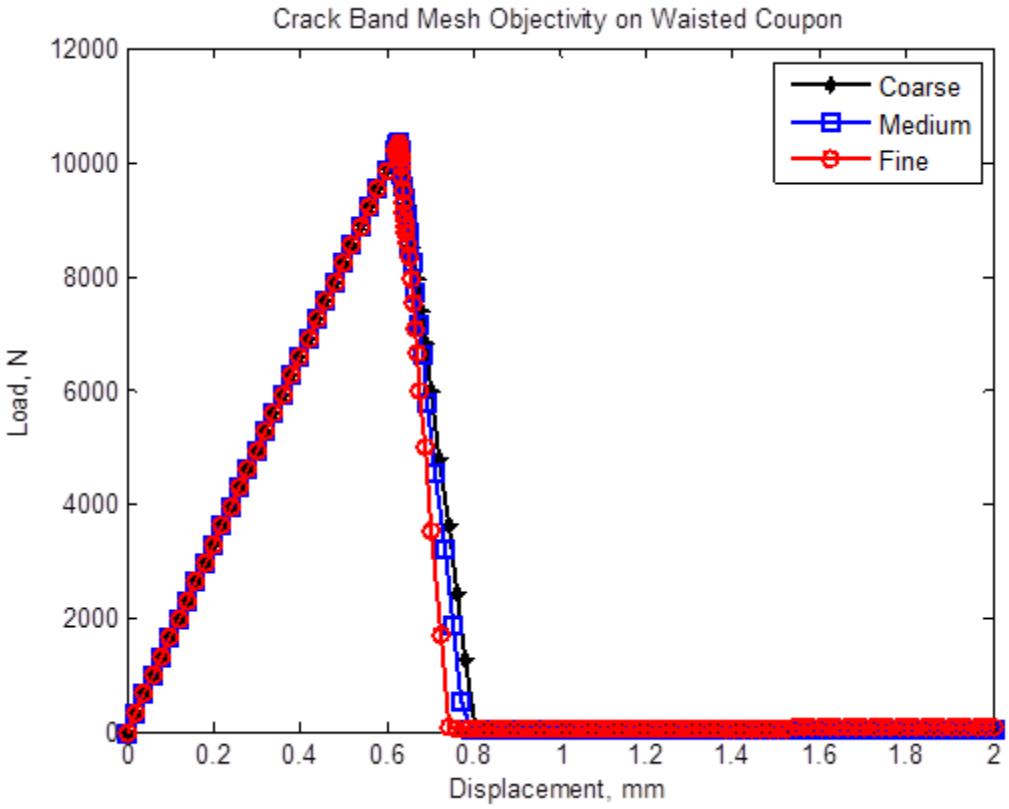

Figure 5.23: Narrowing waist tension coupon mesh objective load vs. displacement results for increasing mesh refinement

Figure 5.24 shows the damage parameter D where blue elements are undamaged and did not enter crack band while the red ones are fully failed and have negligible remaining stiffness. Note that the column of elements that failed are in the exact center of each mesh. This is again due to the narrowing waist geometry and the resulting higher stresses at the narrowest region. The narrow waist test along with the simple block test effectively and clearly demonstrate mesh objectivity for the implemented crack band model.

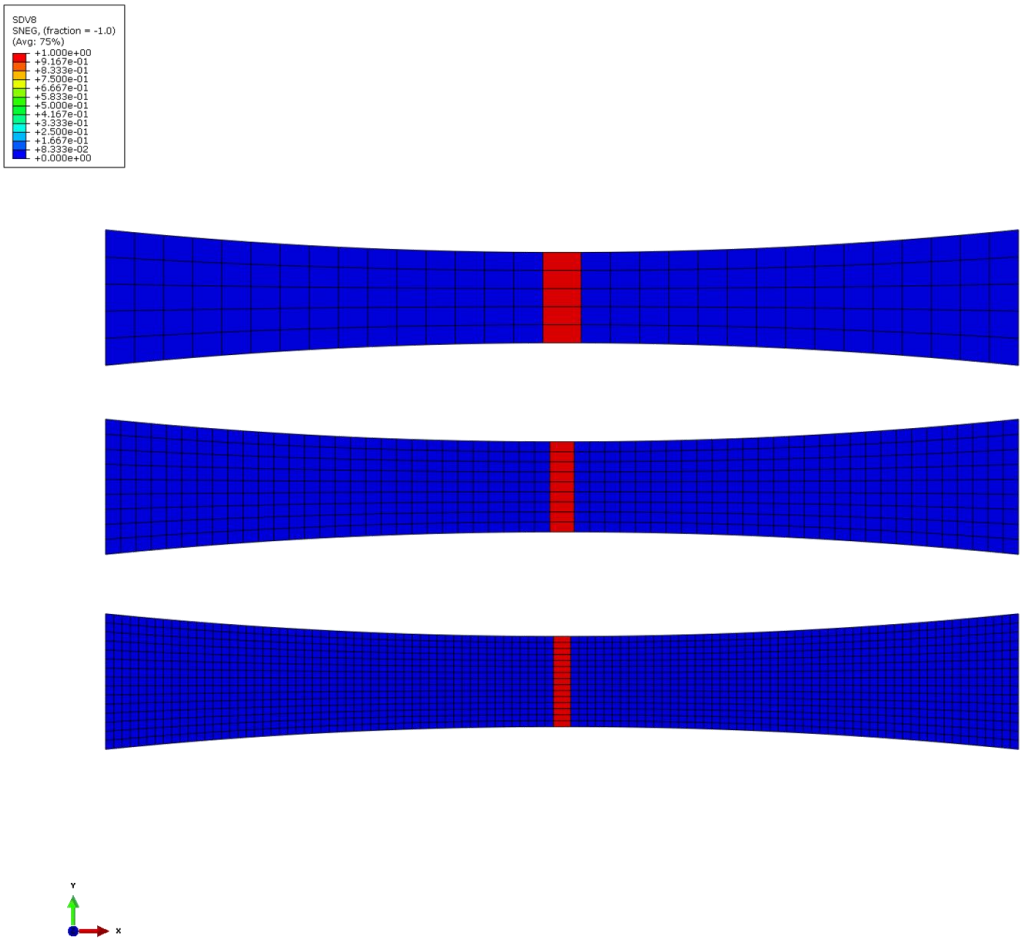

Figure 5.24: Narrowing waist tension coupon failure location with mesh refinement

The crack band model is implemented in the macroscale stiffened panel model only. The mesoscale model load-displacement behavior serves as the criteria the macroscale model checks to determine whether to continue the multiscaling analysis or to enter post-peak behavior using crack band. It is not used in the mesoscale model unlike

some other work using crack band combined with multiscaling techniques [60], [79]. When an element in the macroscale stiffened panel model has a strain state that satisfies the mesoscale load-displacement behavior criteria, the element ceases to communicate with the mesoscale model and therefore the multiscaling framework stops for that element. Future increments will call the crack band model directly as the element has entered a damaged state. Since each loading condition that satisfies the mesoscale failure criteria is slightly different, there is no single critical stress or critical strain used in the analysis. Instead, the peak load just prior to the load drop in the mesoscale model response is divided over the cross sectional area of the unit cell. This stress value is passed back to the macroscale, is treated as the critical stress in calculating the critical strain, and may be different for each element that enters crack band. Other elements, if not meeting the crack band criteria, continue to call the mesoscale model analysis. As a result, some elements may never enter a damaged state and not use the post-peak crack band material description.

5.6 TBC 30 Results

Using the macroscale model from section 5.2, the multiscaling framework as outlined in section 5.3, the RVE mesoscale models discussed in section 5.4, and the crack band damaging material model in section 5.5, computational simulations of the TBC 30 unitized stiffened textile composite panels under compression loading are presented. There are two meshed versions of the macroscale model given in the computational results data. The first is a structured mesh with constant sized shell elements along the gage section length. All computational results with this mesh end in “cb” for labeling purposes because the results use the multiscaling method coupled with the crack band material damaging model. An example of this mesh is shown in Figure 5.25.

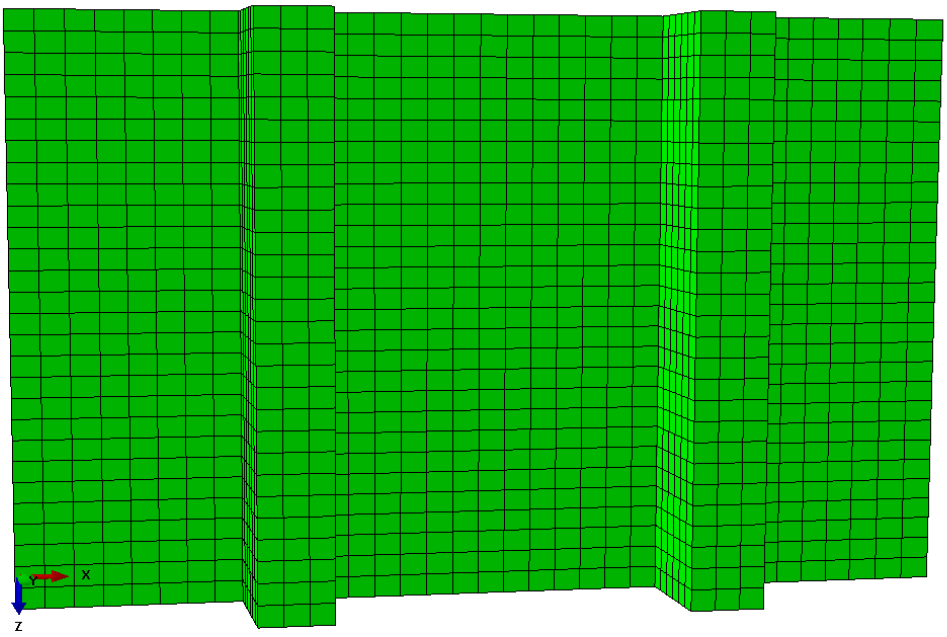

Figure 5.25: TBC panel structured, constant sized element mesh

As a demonstration of mesh objectivity for both the load vs. displacement and crack path results, a second macroscale mesh is created. This second mesh keeps the element lengths similarly sized at the top and bottom of the panel to those used in the first mesh, but biases the center of the panel with smaller elements. While more computationally expensive due to the increased number of elements, the increase is less than double the number of elements than the original mesh. All computational results with the biased mesh end in "cb2" for labeling purposes. Note that the only difference between the two analyses is the macroscale mesh. Both used the multiscaling framework and crack band models. An example of this mesh is shown in Figure 5.26.

Figure 5.27 shows the load vs. displacement experimental, structured mesh with crack band computational model, and biased mesh with crack band computational model curves for panel TBC 30 P1 on the top and TBC 30 P2 on the bottom. P1 observes excellent agreement in the prebuckling loading, however, the postbuckling stiffness of the computational model is less than that observed in the experimental test. Overall agreement with P2 throughout the loading curve is good except for an early failure in both load and displacement.

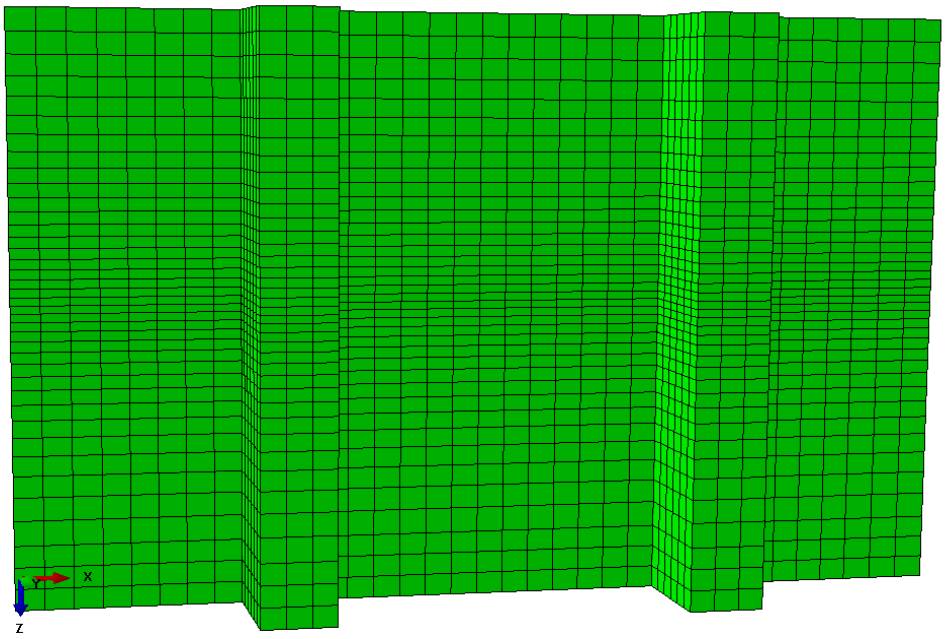

Figure 5.26: TBC panel biased mesh with smaller middle elements

Figure 5.28 shows the extent and location of damaged or failed elements in the macroscale stiffened panel model. Note that the locations of both cracks are centered about the gage section of the panel as generally observed from the experimental tests. The experimental cracks had more variation in the paths than the computational models, however, the overall path direction of straight across the width of the gage section is captured. Such homogenized techniques like crack band, where damage and material failure are smeared across the entire element, are typically ill-suited for resolving explicit computational cracks. Instead, the crack path location using crack band should be interpreted as the area most likely to experience damage and failure instead of the actual location of individual cracks. Therefore, explicit cracks like those observed in Figure 4.30 and Figure 4.31 are not able to be captured using the current models. The scale for the computationally damaged elements is binary where blue indicates undamaged and solid red is completed failed. States of damage on the negative slope of the stiffness reduction constitutive law are shown as dark purple elements. Note that the area of damaged yet not completely failed elements in the center of the panel is similar between both meshes.

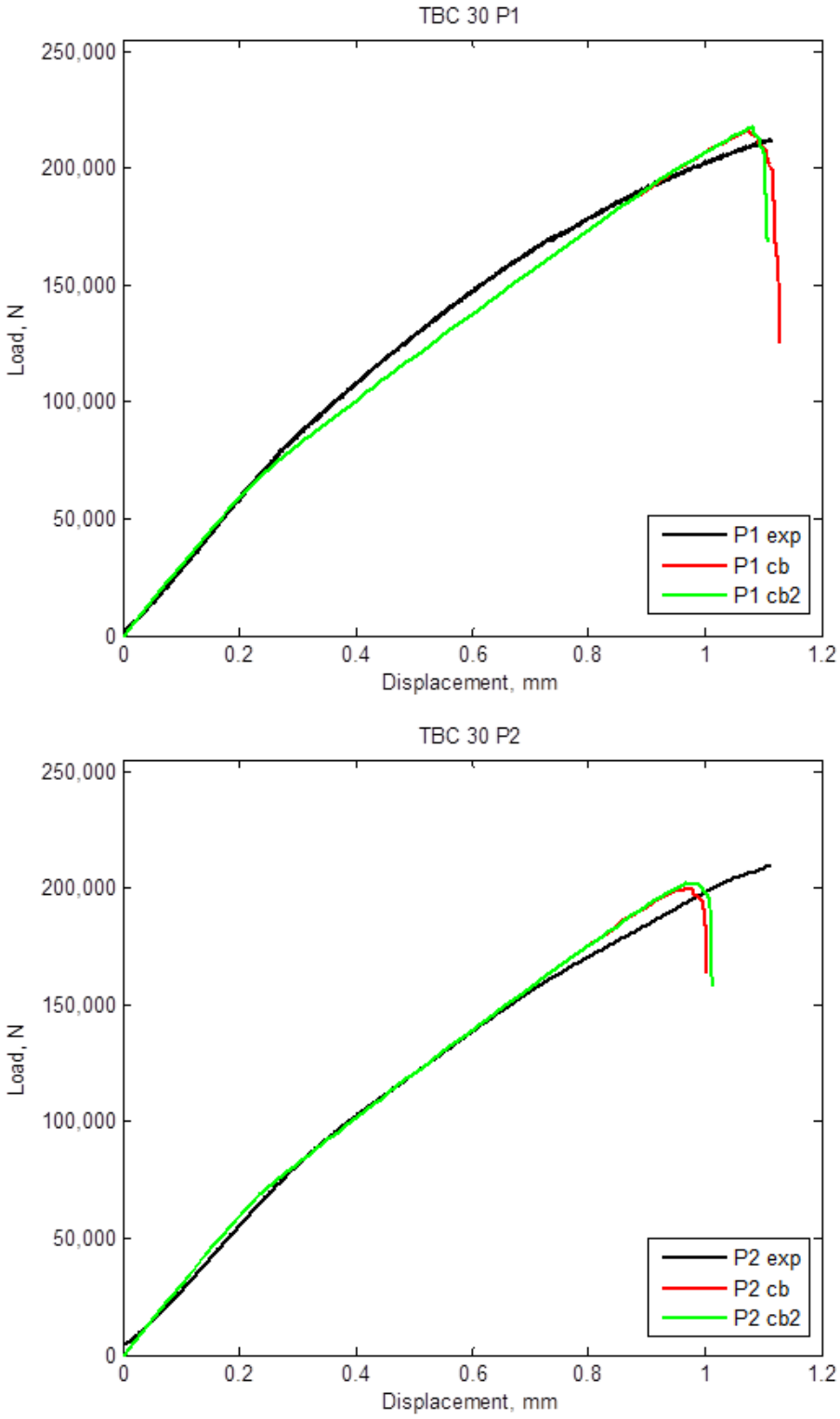

Figure 5.27: TBC 30 P1 (top) and P2 (bottom) experimental and computational load vs. displacement curves

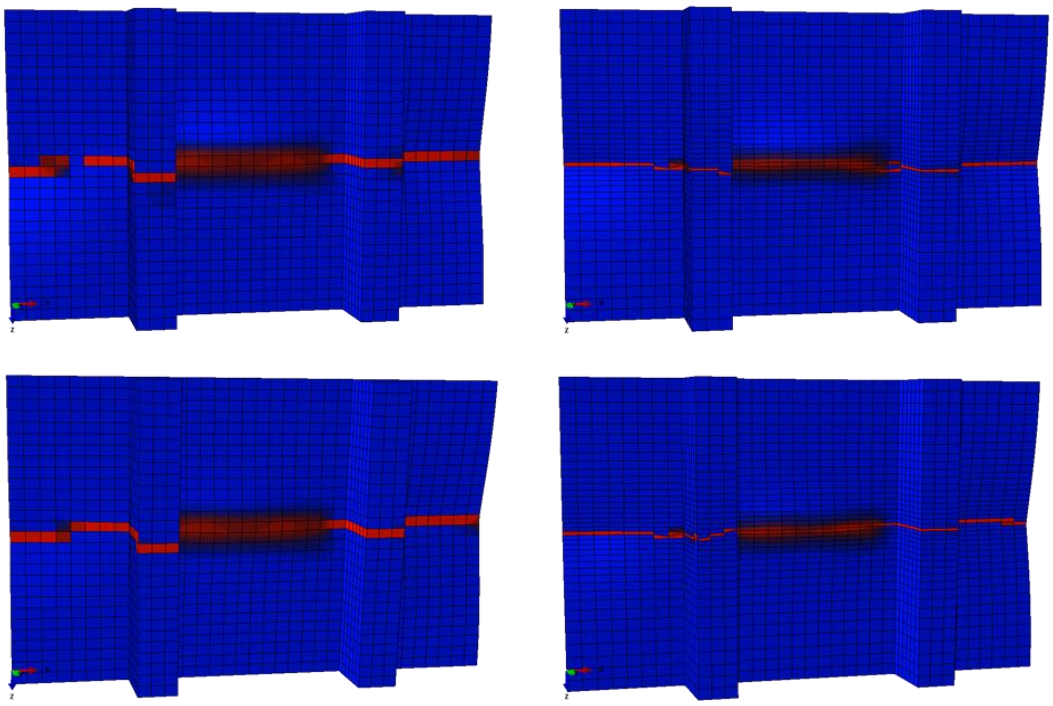

Figure 5.28: TBC 30 P1 structured mesh (top, left), biased mesh (top, right), P2 structured mesh (bottom, left), biased mesh (bottom, right) crack paths

Figure 5.29 shows the load vs. displacement experimental, structured mesh, and biased mesh with crack band curves for panels TBC 30 P3 on the top and P4 on the bottom. Again, P3 demonstrates slightly higher stiffness in the postbuckling regime, but overall good agreement in the prebuckling and failure load and displacement value. P4 demonstrates excellent agreement in all phases of loading.

Figure 5.30 shows the global damage and crack paths in the macroscale stiffened panel model. Similarly to panels P1 and P2, the main crack is centered about the middle of the panel and propagates across the majority of the gage section. Since each skin thickness section for all four TBC 30 panels is slightly different, the crack path and damaged elements are all slightly different. Despite the local variations, however, the trend is extremely consistent with those observed in the experimental tests.

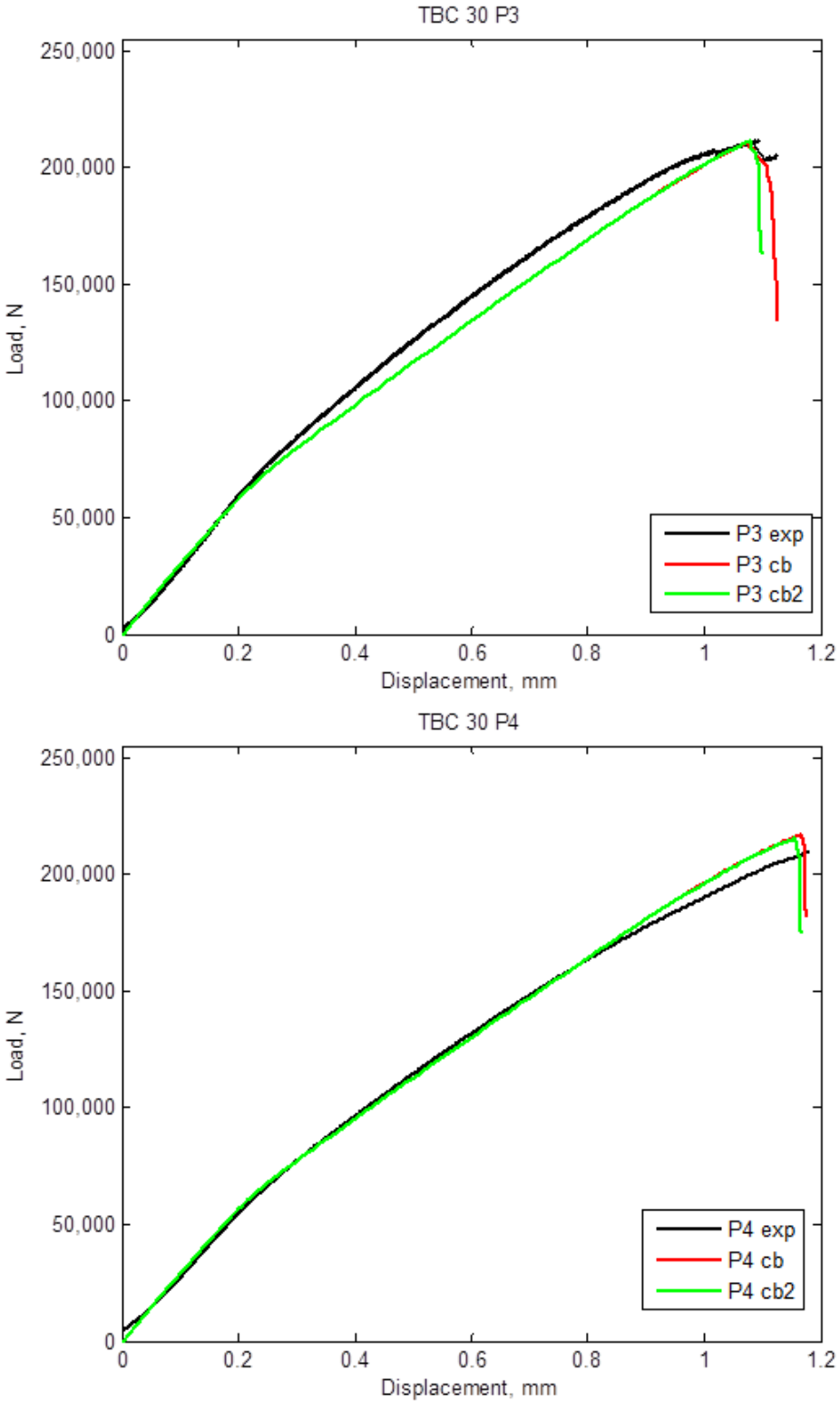

Figure 5.29: TBC 30 P3 (top) and P4 (bottom) experimental and computational load vs. displacement curves

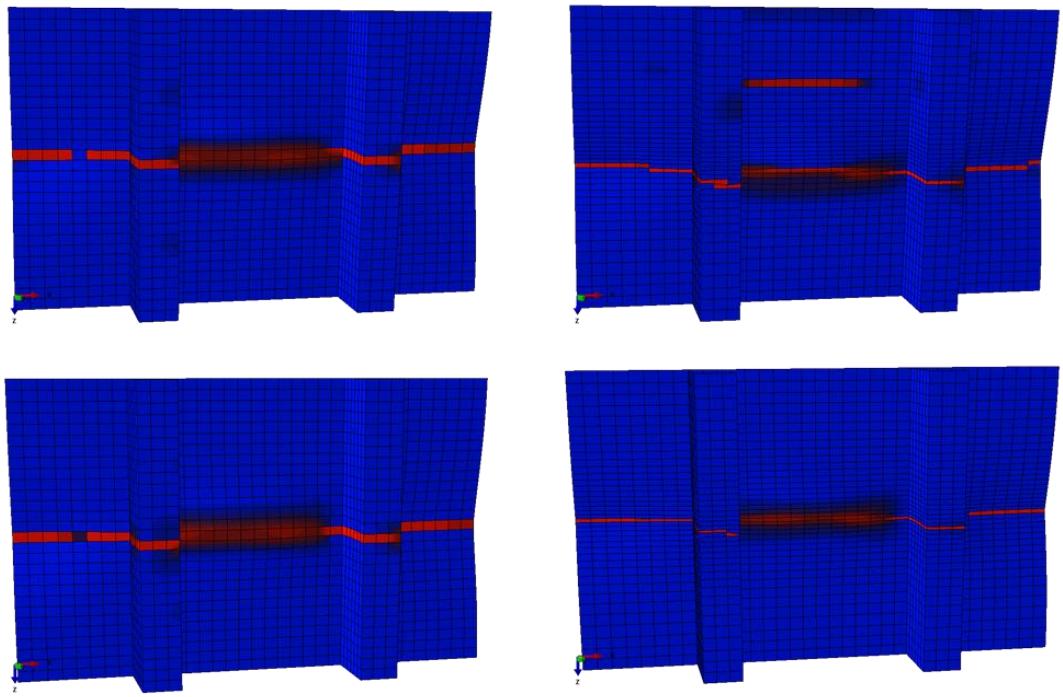

Figure 5.30: TBC 30 P3 structured mesh (top, left), biased mesh (top, right), P4 structured mesh (bottom, left), biased mesh (bottom, right) crack paths

Table 5.5 provides the differences between the structured mesh failure load and displacement compared to the experimentally recorded values. The majority of computational results is within 5% of the experimental values and is acceptable. TBC 30 P2 computationally fails at lower load and displacement. The post-peak computational behavior acts more brittle than the experiment. Damage appears to initiate sooner in the experiment, yet the damage propagation exhibits higher toughness behavior than the crack band model predicts. Toughness in this instance is the area under the curve in the material stiffness degradation as previously described. Higher toughness, all else equal, results in a longer post-peak path and therefore a prolonged damaging state. The experimental curve implies an earlier onset of damage from the deviation in the load-displacement curve, but acts more ductile with a larger post-peak softening region. Other factors such as imperfect loading, boundary conditions, or geometric imperfections not considered such as stiffener spacing and misalignment may account for some of the

discrepancies between the computational model and experimental results. The investigation into these other factors is left as future work.

Table 5.5: TBC 30 computational deviations compared to experimental values

	Displacement	Load
P1	-3.2%	2.0%
P2	-4.8%	-11.8%
P3	-0.47%	-1.37%
P4	3.4%	-0.8%

5.7 TBC 60 Results

Similarly to the results provided in 5.6, the following results provide comparisons between the TBC 60 experimental, structured mesh, and biased mesh computational results. The TBC 60 macroscale models implemented the multiscaling framework to use the TBC 60 RVE as the criteria for entering the crack band damage model. As with the TBC 30 macroscale models, the section specific skin thicknesses were implemented in the TBC 60 macroscale model and result in four sets of computational results – one set for each corresponding experimental panel. Figure 5.31 provides the load vs. displacement curves for panels TBC 60 P1 on the top and P2 on the bottom.

The agreement between the experimental and computational models is overall excellent for TBC 60 P1 and P2. The prebuckling and initial postbuckling stiffnesses are in agreement. The secondary mode switch part of the way through the postbuckling regime is captured by implementing a Riks analysis. The mode switch numerically results in a snap back phenomenon in the global load vs. displacement data. The TBC 60 P1 load-displacement plot marks the snap back numerical event associated with the buckling mode switch. All four TBC 60 panels have this numerical behavior, but it is only highlighted once for clarity. Global failure loads and displacement values are in excellent agreement. Figure 5.32 shows the macroscale damaged elements and overall crack path. Note that the location of the crack path is the same for both the structured, constant element size mesh and the biased mesh. The location of the crack is approximately one-

quarter of the way up from the bottom of the panel. This location corresponds closely to the center of one of the double half-wave mode shapes the panel switches to. The location also corresponds well with the location of the experimentally observed global crack. As with the TBC 30 cracks the slight variation in crack directions are not effectively captured. However, the broad location and paths are in good agreement to the experimental tests.

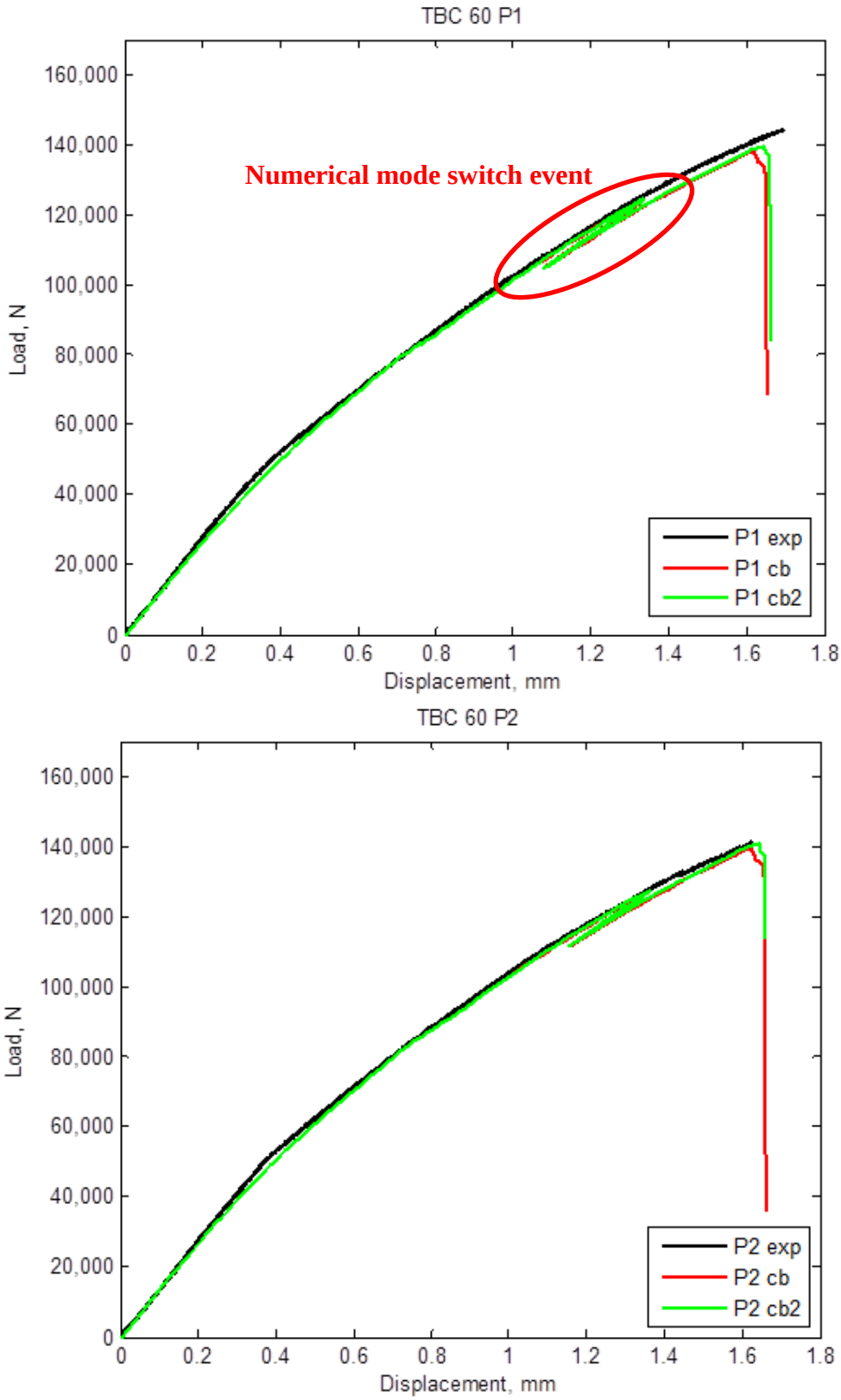

Figure 5.31: TBC 60 P1 (top) and P2 (bottom) experimental and computational load vs. displacement curves

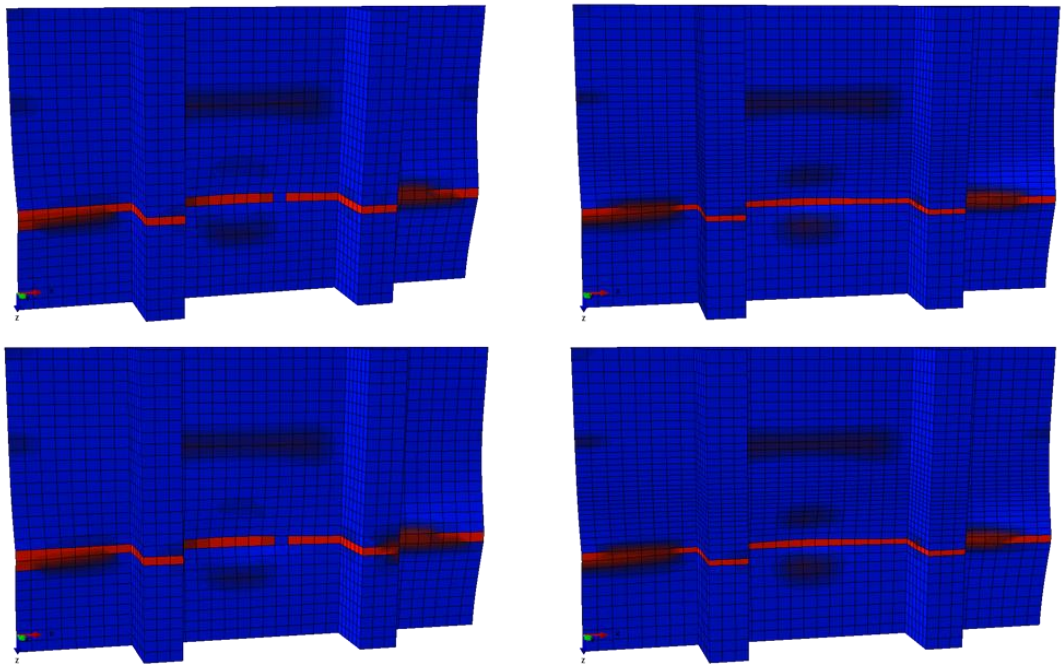

Figure 5.32: TBC 60 P1 structured mesh (top, left), biased mesh (top, right), P2 structured mesh (bottom, left), biased mesh (bottom, right) crack paths

Figure 5.33 shows the load vs. displacement responses of the TBC 60 P3 panel on the left and P4 on the right. The same overall excellent agreement is observed between the computational and experimental results. Also of note is the very similar response between the structured and biased meshes. This indicates that the local strain fields and deformation gradients are resolved accurately enough for the mesoscale models to signal when to correctly enter crack band. Despite having significantly thinner skin sections than the nominal model, TBC 60 P4 matches excellently when the section average thickness data is included in the model.

Figure 5.34 shows the global damaged element areas and developed crack path. The agreement between meshes is very good, and the location and general behavior of the crack is in line with experimentally observed results. Note that there are elements that have initiated the crack band damage model but have not fully failed in the top quarter of the *center skin section* for both meshes. This location corresponds to the maximum out-of-plane displacement location for the top half wave. Table 5.6 provides a comparison of the TBC 60 constant sized element mesh results to the experimentally obtained values.

As noted, the agreement is typically very good with both load and displacement failure values are within 5%.

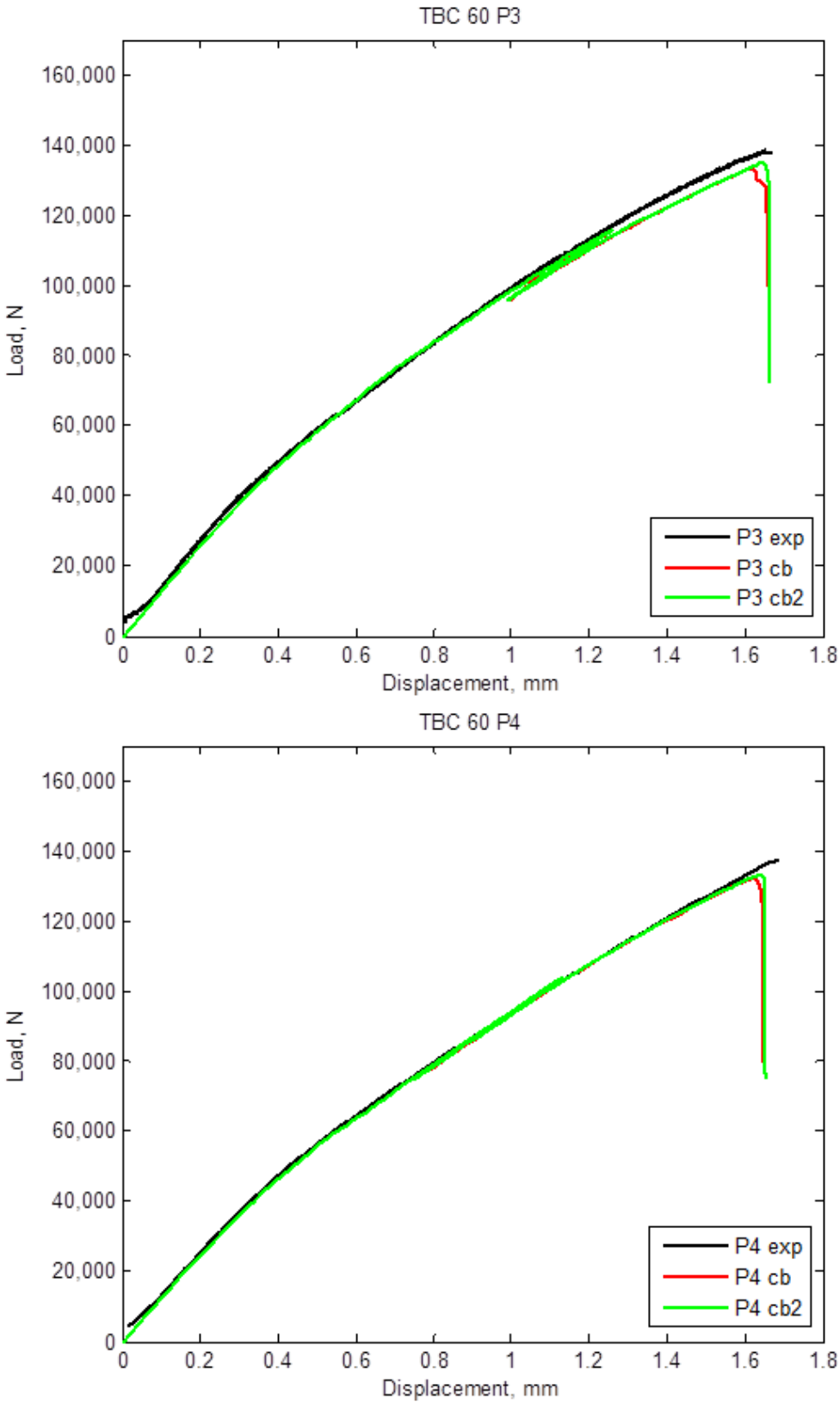

Figure 5.33: TBC 60 P3 (top) and P4 (bottom) experimental and computational load vs. displacement curves

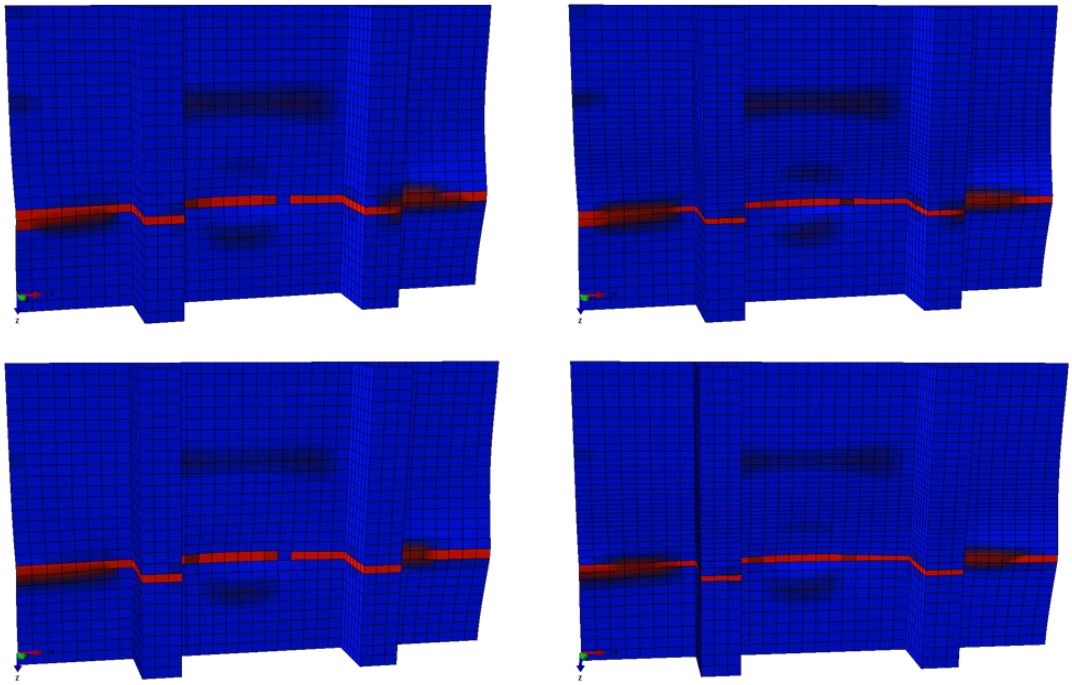

Figure 5.34: TBC 60 P3 structured mesh (top, left), biased mesh (top, right), P4 structured mesh (bottom, left), biased mesh (bottom, right) crack paths

Table 5.6: TBC 60 computational deviations compared to experimental values

	Displacement	Load
P1	-4.2%	-4.3%
P2	0.18%	-1.2%
P3	-3.0%	-2.8%
P4	-3.4%	-3.9%

5.8 Summary

A computational macroscale model designed to the manufactured nominal specifications was created. Local section thickness variations were then included to increase agreement of the postbuckled stiffnesses for all TBC 30 and 60 panels. The development and implementation of a multiscale framework was discussed. The flow of information from the macroscale to the mesoscale using the deformation gradient and periodic boundary conditions enabled the mesoscale to accurately signal the macroscale

element to enter the crack band material damaging constitutive model. The local mesoscale model development including the TBC fiber tow geometry generation and implementation of the as-manufactured in-situ non-linear matrix material characterization was explained. An overview of the crack band methodology and background was given.

Results and discussions of the experimental and computational results were provided for both the TBC 30 and 60 panels. Overall, good agreement exists between the TBC 30 experimental and computational model. There is room for future work in the investigation of a couple postbuckling stiffness discrepancies as well as one case of early computational failure. There was excellent agreement, however, between the TBC 60 experimental and computational models. Mesh objectivity is achieved as two differently designed meshes return similar results. The location and paths of damage and failure are in general agreement with the experimental specimens.

CHAPTER 6

Concluding Remarks

6.1 Conclusions

Stiffener separation is shown to be removed as a primary structural failure mode for unitized stiffened composite textile panels loaded under axial compression well into the postbuckling regime. Instead, a material damaging and failure model effectively captures the local post-peak material response via incorporating a mesoscale model using a multiscaling framework and macroscale model failure event of the stiffened panel. Experimental results are in overall excellent agreement compared to the computational modeling responses. Minor deviations exist for some of the TBC 30 panels and are attributed to factors outside the scope of this work. To achieve such results, a manufacturing method that takes advantage of the nature of textiles is developed and characterized. The characterization efforts include investigations into the material constituent components via acid digestion and optical imaging techniques. As-manufactured geometric imperfection data is collected, analyzed, and implemented into the macroscale homogenized stiffened panel model to provide panel dependent behavior to the results. A smeared crack damage and failure model is implemented into the macroscale model, and it is activated by a criteria based on the TBC architecture dependent mesoscale models developed using the textile generation software TexGen [64].

6.2 Future Work

Much potential exists for future improvement of the work discussed in this thesis. Research never finishes, only projects. The following sections outline broad topics that are of particular interest due to the technical challenges presented as well as the potential for significant benefits should they be accomplished successfully. The first area of future development is in variable angle braided composite manufacturing, testing, and analysis. Significant advancements have been achieved in recent years by braiding, weaving, and knitting technologies in the areas of high performance fibers such as glass and carbon. The second area of future development is to increase the scope of the work conducted so far and apply the concepts and knowledge learned to large scale structures. The stiffened panels tested so far are small in comparison to structures that are in use in air and space applications. Scalability studies must be performed in order to determine the feasibility of incorporating unitized structures into flight ready vehicles. Lastly, numerical development of the multiscaling framework is severely needed in order to make the method as outlined in this work feasible for large problems.

6.2.1 Variable Angle Tow Braiding

Variable angle and fiber direction tailoring techniques have been of interest for many years. Recent advancements in manufacturing and analysis methods have become powerful enough to be applied to these complex problems. Braiding, weaving, and knitting composite technologies offer distinct advantages compared to unidirectional flat lamina by incorporating tow steering concepts during manufacturing. Incorporating unitized structure concepts via the use of alternative materials like composite textiles expands the design space even more than what traditional composites currently have. The ability to tailor a structure not only to minimize weight while meeting performance requirements, but to design it to be simple to manufacture, straightforward to analyze, and even designed to remove problems such as certain failure modes increases the potential for further structural efficiency. Hwang [83] expanded on the closed form solution of an analytic model of a TBC RVE proposed by Quek [2] and expanded by Kier [20] that resulted in the implementation of the model in an optimization study that solves

an RVE tow packing problem for generic tow braid angles. Using the analytic method from Quek and Kier to solve for the RVE fully 3D stiffness components, the optimization study demonstrated using nonstandard braid angle TBC composites as part of the design variable input list for a larger structure. This was previously not possible due to the inherent dependency of the tow braid angle geometry on an RVE homogenized stiffness calculation. Hwang's work has potential to replace the fully 3D finite element mesoscale model with an analytic representation possible of calculating the initial stiffness of any angle braid. The analytic representation can significantly decrease computational time required as it is faster than the finite element method currently outlined. Development of the model such that damage initiation and progressive damage analysis can also be incorporated will result in completely removing the need for the currently implemented finite element mesoscale model and offers significant computational performance benefits without loss of fidelity or accuracy. The multiscale framework could then be used as a design tool to inform structural design on local braid angle variations instead of being used primarily as a post-test analysis tool.

6.2.2 Component Manufacturing

Expanding the scope of this work to large scale structures is needed before final determination can be made as to the effectiveness of the unitized structure concept. The initial results provided by this work, and other work, show strong potential to be a useful concept. However, further development is needed across the range of topics both covered and not covered by this work. The simple issue of size effects [57] may prove that the potential benefit of unitized structures is limited beyond a certain scale. This area is as yet unknown and therefore requires further investigation.

6.2.3 Multiscale Framework Parallelization

The multiscaling framework is currently implemented in a serial fashion – i.e. one element enters the UMAT at a time, the mesoscale analysis is performed and data processed, and then the analysis continues with the next element in the macroscale model. Such a technique is used due to the ease of development required to get a working prototype running. However, parallelization schemes absolutely must be included in

future work if the multiscaling method is to be of real benefit for researchers and users. The ability to perform multiple mesoscale model analyses concurrently provides scale to the computational problem that then becomes limited only by the number of computing resources available.

6.2.4 Stiffener Geometry Characterization

The stiffeners were observed to deviate from the nominal locations after processing the scanned imperfection data. Primarily, a stiffener may be shifted one way or the other by up to the value of the skin thickness. The spacing between stiffeners is directly traceable to the VARTM manufacturing method where the resin flow media and insert blocks do not provide strict dimension control over the preform. Stiffener spacing geometric imperfection was not studied in this work. Stiffener spacing can have significant effects not only on the overall global stiffness of the structure, but also effects the buckling loads, modes, and postbuckling response [84].

BIBLIOGRAPHY

[1] J. M. Comiez, A. M. Waas, and K. W. Shahwan, "Delamination buckling; Experiment and analysis," *Int. J. Solids Struct.*, vol. 32, no. 6–7, pp. 767–782, 1995.

[2] S. C. Quek, A. M. Waas, K. W. Shahwan, and V. Agaram, "Analysis of 2D triaxial flat braided textile composites," *Int. J. Mech. Sci.*, vol. 45, pp. 1077–1096, 2003.

[3] C. Heinrich, M. Aldridge, A. S. Wineman, J. Kieffer, A. M. Waas, and K. Shahwan, "The influence of the representative volume element (RVE) size on the homogenized response of cured fiber composites," *Model. Simul. Mater. Sci. Eng.*, vol. 20, no. 7, 2012.

[4] Z. Bazant and B. Oh, "Crack band theory of concrete," *Mater. Struct.*, vol. 16, pp. 155–177, 1983.

[5] R. M. Jones, *Mechanics of Composite Materials*. CRC Press, 1998.

[6] C. A. Rose and C. T. Herakovich, "An approximate solution for interlaminar stresses in composite laminates," *Compos. Eng.*, vol. 3, no. 3, pp. 271–285, 1993.

[7] W. Callister, *Material Science and Engineering: An Introduction*, 7th ed. New York: John Wiley & Sons, Inc., 2007.

[8] S. Song, A. M. Waas, K. W. Shahwan, O. Faruque, and X. Xiao, "Effects of Matrix Microcracking on the Response of 2D Braided Textile Composites Subjected to Compression Loads," *J. Compos. Mater.*, vol. 44, no. 2, pp. 221–240, 2009.

[9] M. Rask, B. Madsen, B. F. Sørensen, J. L. Fife, K. Martyniuk, and E. M. Lauridsen, "In situ observations of microscale damage evolution in unidirectional natural fibre composites," *Compos. Part A Appl. Sci. Manuf.*, vol. 43, no. 10, pp. 1639–1649, 2012.

[10] K. P. Walker, E. H. Jordan, and A. D. Freed, “Nonlinear mesomechanics of composites with periodic microstructure,” no. June, 1989.

[11] J. Arbocz and J. G. Williams, “Imperfection surveys on a 10-ft-diameter shell structure,” *AIAA J.*, vol. 15, no. 7, pp. 949–956, 1977.

[12] R. A. Schapery, “Prediction of compressive strength and kink bands in composites using a work potential,” *Int. J. Solids Struct.*, vol. 32, no. 6–7, pp. 739–765, 1995.

[13] S. V. Lomov, D. S. Ivanov, I. Verpoest, M. Zako, T. Kurashiki, H. Nakai, and S. Hirosawa, “Meso-FE modelling of textile composites: Road map, data flow and algorithms,” *Compos. Sci. Technol.*, vol. 67, no. 9, pp. 1870–1891, 2007.

[14] S. P. Yushanov and A. E. Bogdanovich, “Fiber waviness in textile composites and its stochastic modeling,” *Mech. Compos. Mater.*, vol. 36, no. 4, pp. 297–318, 2000.

[15] Z. M. Huang and S. Ramakrishna, “Modeling inelastic and strength properties of textile laminates: A unified approach,” *Compos. Sci. Technol.*, vol. 63, no. 3–4, pp. 445–466, 2003.

[16] S. V. Lomov, D. S. Ivanov, I. Verpoest, M. Zako, T. Kurashiki, H. Nakai, J. Molimard, and A. Vautrin, “Full-field strain measurements for validation of meso-FE analysis of textile composites,” *Compos. Part A Appl. Sci. Manuf.*, vol. 39, no. 8, pp. 1218–1231, 2008.

[17] M. Danielsson, D. M. Parks, and M. C. Boyce, “Three-dimensional micromechanical modeling of voided polymeric materials,” *J. Mech. Phys. Solids*, vol. 50, no. 2, pp. 351–379, 2002.

[18] “MATLAB.” The MathWorks, Inc., Natick, Massachusetts.

[19] “ImageJ.” National Institute of Health, 2012.

[20] Z. T. Kier, A. Salvi, G. Theis, A. M. Waas, and K. W. Shahwan, “Estimating mechanical properties of 2D triaxially braided textile composites based on microstructure properties,” *Compos. Part B Eng.*, vol. 68, pp. 288–299, 2015.

[21] “ASTM D3171 Standard Test Methods for Constituent Content of Composite Materials,” *ASTM Int.*, pp. 1–6, 2010.

[22] C. A. Featherston, “Geometric imperfection sensitivity of curved panels under combined compression and in-plane bending - A study using adaptive meshing and DIC,” *Strain*, vol. 48, pp. 286–295, 2012.

[23] M. W. Hilburger, M. P. Nemeth, and J. H. Starnes, “Shell Buckling Design Criteria Based on Manufacturing Imperfection Signatures,” *AIAA J.*, vol. 44, no. 3, pp. 654–663, 2006.

[24] D. Bushnell, “Optimization of composite, stiffened, imperfect panels under combined loads for service in the postbuckling regime,” *Comput. Methods Appl. Mech. Eng.*, vol. 103, pp. 43–114, 1993.

[25] “Focus Inspection.” Nikon Metrology, Inc., Brighton, MI, 2014.

[26] M. R. Pankow, “The Deformation Response of 3D Woven Composites Subjected to High Rates of Loading,” 2010.

[27] C. Heinrich, “The Influence of the Curing Process on the Response of Textile Composites,” 2011.

[28] M. Farshad, M. Wildenberg, and P. Flüeler, “Determination of shear modulus and Poisson’s ratio of polymers and foams by the anticlastic plate-bending method,” *Mater. Struct.*, vol. 30, no. 6, pp. 377–382, 1997.

[29] “ASTM D3044 Standard Test Method for Shear Modulus of Wood-Based Structural Panels,” *ASTM International*. pp. 10–12, 2000.

[30] H. Yoshihara and Y. Sawamura, “Measurement of the shear modulus of wood by the square-plate twist method,” *Holzforschung*, vol. 60, no. 5, pp. 543–548, 2006.

[31] S. C. Quek and A. M. Waas, “Instabilities in Braided Textile Composites Under Uniaxial Compressive and Biaxial Loadings,” *43rd AIAA/ASME/ASCE/AHS/ASC Struct. Struct. Dyn. Mater. Conf.*, no. April, pp. 1–12, 2002.

[32] P. Prabhakar and A. M. Waas, “Interaction between kinking and splitting in the compressive failure of unidirectional fiber reinforced laminated composites,” *Compos. Struct.*, vol. 98, pp. 85–92, 2013.

[33] Z. Xia, Y. Zhang, and F. Ellyin, “A unified periodical boundary conditions for representative volume elements of composites and applications,” *Int. J. Solids Struct.*, vol. 40, no. 8, pp. 1907–1921, 2003.

[34] C. T. Herakovich, *Mechanics of Fibrous Composites*. New York: Wiley, 1998.

[35] W. H. Ng, A. G. Salvi, and A. M. Waas, “Characterization of the in-situ non-linear shear response of laminated fiber-reinforced composites,” *Compos. Sci. Technol.*, vol. 70, no. 7, pp. 1126–1134, 2010.

[36] R. M. Christensen and F. M. Waals, “Effective Stiffness of Randomly Oriented Fibre Comopsites,” *J. Compos. Mater.*, vol. 6, pp. 518–535, 1972.

[37] “Toray T-700 Carbon Fiber Data Sheet.” Toray Industries, Inc.

[38] W. Chen and D. Ham, *Plasticity for Structural Engineers*. New York: Springer-Verlag, 1988.

[39] C. Bisagni, “Progressive Delamination Analysis of Stiffened Composite Panels in Post-Buckling,” in *47th AIAA/ASME/ASCE/AHS/ASC Structures, Structural Dynamics, and Materials Conference*, 2006, no. May, pp. 1–12.

[40] D. C. Jegley, “Experimental Behavior of Fatigued Single Stiffener PRSEUS Specimens,” *NASA/TM -2009-215955*, no. December, 2009.

[41] A. H. Chilver, “Coupled Modes of Elastic Buckling,” *J. Mech. Phys. Solids*, vol. 15, pp. 15–28, 1967.

[42] B. G. Falzon and G. P. Steven, “Buckling mode transition in hat-stiffened composite panels loaded in uniaxial compression,” *Compos. Struct.*, vol. 37, no. 96, pp. 253–267, 1997.

[43] T. Nakamura and K. Uetani, “The Secondary Buckling and Post-Secondary Buckling Behaviours of Rectangular Plates,” *Int. J. Mech. Sci.*, vol. 21, pp. 265–286, 1979.

[44] M. Stein, “The Phenomenon of Change Pattern Buckle Pattern in Elastic Structures,” *NASA/TR-R-39*, p. 14, 1959.

[45] F. Stoll, “Analysis of the snap phenomenon in buckled plates,” *Int. J. Non. Linear. Mech.*, vol. 29, no. 2, pp. 123–138, 1994.

[46] W. J. Supple, “Coupled Branching Configurations in the Elastic Buckling of Symmetric Structural Systems,” vol. 9, pp. 97–112, 1967.

[47] W. J. Supple, “Changes of wave-form post-buckling,” *Int. J. Solids Struct.*, vol. 6, pp. 1243–1258, 1970.

[48] M. Uemura and O. Byon, “Secondary Buckling of a Flat Plate Under Uniaxial Compression Part 1: Theoretical Analysis of Simply Supported Flat Plate,” *Int. J. Non. Linear. Mech.*, vol. 12, no. 6, pp. 355–370, 1977.

[49] F. Stoll, “An implementation of solution strategies for the analysis of complex non-linear equilibrium behavior,” *Int. J. Non. Linear. Mech.*, vol. 29, no. 2, pp. 109–122, 1994.

[50] N. Tiwari and M. W. Hyer, “Secondary buckling of compression-loaded composite plates,” *AIAA J.*, vol. 40, no. 10, pp. 2120–2126, 2002.

[51] F. C. Caner, Z. P. Bažant, C. G. Hoover, A. M. Waas, and K. W. Shahwan, "Microplane Model for Fracturing Damage of Triaxially Braided Fiber-Polymer Composites," *J. Eng. Mater. Technol.*, vol. 133, no. 2, 2011.

[52] C. S. Lopes, Z. Gürdal, and P. P. Camanho, "Variable-stiffness composite panels: Buckling and first-ply failure improvements over straight-fibre laminates," *Comput. Struct.*, vol. 86, pp. 897–907, 2008.

[53] C. Meeks, E. Greenhalgh, and B. G. Falzon, "Stiffener debonding mechanisms in post-buckled CFRP aerospace panels," *Compos. Part A Appl. Sci. Manuf.*, vol. 36, pp. 934–946, 2005.

[54] S. Nagendra, Z. Gürdal, R. T. Haftka, and J. H. Starnes, "Buckling and failure characteristics of compression-loaded stiffened composite panels with a hole," *Compos. Struct.*, vol. 28, pp. 1–17, 1994.

[55] D. Zhang, A. M. Waas, and C. F. Yen, "Progressive damage and failure response of hybrid 3D textile composites subjected to flexural loading, part I: Experimental studies," *Int. J. Solids Struct.*, vol. 75–76, pp. 309–320, 2015.

[56] J. G. Rots, P. Nauta, G. M. A. Kusters, and J. Blaauwendraad, "Smeared Crack Approach and Fracture Localization in Concrete," *HERON*, vol. 30, no. 1, 1985.

[57] A. G. Salvi, A. M. Waas, and A. Caliskan, "Specimen size effects in the off-axis compression test of unidirectional carbon fiber tow composites," *Compos. Sci. Technol.*, vol. 64, no. 1, pp. 83–97, 2004.

[58] "Abaqus." Dassault Systemes Simulia Corp.

[59] Abaqus, "Abaqus User's Manual." Dassault Systemes Simulia Corp., 2014.

[60] P. Meyer and A. M. Waas, "Mesh-objective two-scale finite element analysis of damage and failure in ceramic matrix composites," *Integr. Mater. Manuf. Innov.*, vol. 4, no. 1, p. 18, 2015.

[61] D. Zhang and A. M. Waas, "A micromechanics based multiscale model for nonlinear composites," *Acta Mech.*, vol. 225, pp. 1391–1417, 2014.

[62] K. C. Liu, A. Chattopadhyay, B. Bednarcyk, and S. M. Arnold, "Efficient Multiscale Modeling Framework for Triaxially Braided Composites using Generalized Method of Cells," *J. Aerosp. Eng.*, vol. 24, no. April, pp. 162–169, 2011.

[63] "Python Language Reference, 2.7." Python Software Foundation.

[64] H. Lin, L. P. Brown, and A. C. Long, “Modelling and Simulating Textile Structures Using TexGen,” *Adv. Mater. Res.*, vol. 331, pp. 44–47, 2011.

[65] W. Wu and J. Owino, “Applying Periodic Boundary Conditions in Finite Element Analysis,” *Simulia Community Conf.*, pp. 707–719, 2014.

[66] X. F. Wang, X. W. Wang, G. M. Zhou, and C. W. Zhou, “Multi-scale Analyses of 3D Woven Composite Based On Periodicity Boundary Conditions,” *J. Compos. Mater.*, vol. 41, no. 14, pp. 1773–1788, 2007.

[67] H. Lin, M. Clifford, A. C. Long, and M. Sherburn, “Finite element modelling of fabric shear,” *Model. Simul. Mater. Sci. Eng.*, vol. 16, 2008.

[68] N. V. De Carvalho, S. T. Pinho, and P. Robinson, “Reducing the domain in the mechanical analysis of periodic structures, with application to woven composites,” *Compos. Sci. Technol.*, vol. 71, no. 7, pp. 969–979, 2011.

[69] C. T. Sun and R. S. Vaidya, “Prediction of composite properties from a representative volume element,” *Compos. Sci. Technol.*, vol. 56, no. 2, pp. 171–179, 1996.

[70] Z. Xia, C. Zhou, Q. Yong, and X. Wang, “On selection of repeated unit cell model and application of unified periodic boundary conditions in micro-mechanical analysis of composites,” *Int. J. Solids Struct.*, vol. 43, no. 2, pp. 266–278, 2006.

[71] D. S. Ivanov, F. Baudry, B. Van Den Broucke, S. V. Lomov, H. Xie, and I. Verpoest, “Failure analysis of triaxial braided composite,” *Spec. Issue 12th Eur. Conf. Compos. Mater. ECCM 2006*, vol. 69, no. 9, pp. 1372–1380, 2008.

[72] S. V. Lomov, D. S. Ivanov, T. C. Truong, I. Verpoest, F. Baudry, K. Vanden Bosche, and H. Xie, “Experimental methodology of study of damage initiation and development in textile composites in uniaxial tensile test,” *Compos. Sci. Technol.*, vol. 68, no. 12, pp. 2340–2349, 2008.

[73] M. Kumosa, G. Odegard, D. Armentrout, L. Kumosa, K. Searles, and J. K. Sutter, “Comparison of the ± 45° tensile and iosipescu shear tests for woven fabric composite materials,” *J. Compos. Technol. Res.*, vol. 24, no. 1, p. 3, 2002.

[74] S. C. Quek, A. Waas, K. W. Shahwan, and V. Agaram, “Compressive response and failure of braided textile composites: Part 2 - Computations,” *Int. J. Non. Linear. Mech.*, vol. 39, pp. 649–663, 2004.

[75] M. J. Shuart, “Analysis of Shear Failure Mechanisms,” *J. Compos. Mater.*, vol. 23, pp. 251–263, 1989.

[76] M. J. Shuart, “Failure of Compression-Loaded Multidirectional Composite Laminates,” *AIAA J.*, vol. 27, no. 9, pp. 1274–1279, 1989.

[77] S. Song, A. M. Waas, K. W. Shahwan, O. Faruque, and X. (Sharon) Xiao, “Compression response, strength and post-peak response of an axial fiber reinforced tow,” *Int. J. Mech. Sci.*, vol. 51, no. 7, pp. 491–499, 2009.

[78] C. Heinrich and A. Waas, “Investigation of progressive damage and fracture in laminated composites using the smeared crack approach,” *53rd AIAA/ASME/ASCE/AHS/ASC Struct. Struct. Dyn. Mater. Conf.*, pp. 1537–1556, Apr. 2012.

[79] P. Meyer and A. M. Waas, “FEM predictions of damage in continous fiber ceramic matrix composites under transverse tension using the crack band method,” *Acta Mater.*, vol. 102, pp. 292–303, 2016.

[80] E. J. Pineda, B. a Bednarcyk, A. M. Waas, and S. M. Arnold, “Implementation of a Smeared Crack Band Model in a Micromechanics Framework,” *NASA/TM-2012-217603*, no. June, 2012.

[81] N. V. De Carvalho, S. T. Pinho, and P. Robinson, “An experimental study of failure initiation and propagation in 2D woven composites under compression,” *Compos. Sci. Technol.*, vol. 71, no. 10, pp. 1316–1325, 2011.

[82] W. Xu and A. M. Waas, “Modeling damage growth using the crack band model; effect of different strain measures,” *Eng. Fract. Mech.*, vol. 152, pp. 126–138, 2016.

[83] J. T. Hwang, A. M. Waas, and J. R. R. a Martins, “Micromechanical Modeling and Design Optimization of 2-D Triaxial Braided Composites,” *AIAA Aerosp. Sci. Meet. Incl. New Horizons Forum Aerosp. Expo.*, 2012.

[84] D. Brush and B. Almroth, *Buckling of Bars, Plates, and Shells*, First Edit. McGraw-Hill Inc., 1975.